STUDIES OF DISLOCATION GEOMETRIES USING HIGH-RESOLUTION ELECTRON MICROSCOPY

S.M. HOLMES B.A.

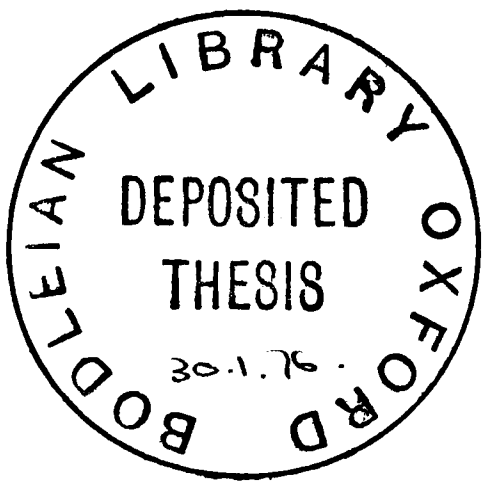

A dissertation submitted for the degree of Doctor of Philosophy in the University of Oxford, October 1975.

Abstract

Conventional strong-beam imaging techniques have been widely applied in the study of crystal defects, the main advantage being the high intensity of the images which reduces photographic exposure times to a few seconds at most, thus avoiding problems of drift and contamination. However, such images have the disadvantage of not being related in any simple way to the defect geometry, and they are relatively insensitive to small changes in the strain field. The width of a peak from a dislocation can be ~100 Å for 100keV electrons, and so the study of dislocations separated by the much smaller distances that are found in dissociated dislocations or faulted dipoles in pure metals is very difficult, even with careful computed image matching techniques. The weak-beam technique of electron microscopy (Cockayne, Ray and Whelan 1969) overcomes this problem by tilting the specimen so that only the highly-strained regions near dislocation cores contribute to the final image; narrow (~15 Å), relatively intense peaks which lie close to the defects are obtained by this approach, and such images are ideal for investigating closely-spaced dislocations.

This thesis describes the study of various dislocation geometries by the weak-beam technique and the calculation of equivalent images. Chapter 1 reviews the theories of electron diffraction which are needed both to understand the properties of weak-beam images and also to compute the images required for comparison with experimental micrographs. Such calculations require a knowledge of the displacement field of a dislocation, and in most cases if any useful information is to be derived from weak-beam observations of dislocation networks (e.g. the stacking-fault energy) the stress fields are also required. Chapter 2 discusses the anisotropic theory of infinite straight dislocations as given by Stroh (1958); the only defects considered here are those for which this infinite straight approximation is reasonable, e.g. the partial dislocations

in a faulted dipole, or the dissociated straight edge of a very large loop.

Chapter 3 applies the weak-beam technique to the study of faulted dipoles in copper and it is shown that such images define the dipole geometry with a greater accuracy than hitherto possible using conventional techniques. Previous strong-beam studies of faulted dipoles are also discussed. An upper limit for the stacking-fault energy of copper of

$$\gamma_{max} = 47 \pm 8 \text{ erg cm}^{-2}$$

is obtained. It is concluded that similar studies are potentially very useful for estimating the stacking-fault energy of materials for which γ and the elastic constants are such that the dissociation of single dislocations cannot be resolved.

The rest of the thesis considers the effect that a finite divergence in the illuminating beam of electrons has on weak-beam images. The oscillatory effects dependent on depth and thickness which are often observed in weak-beam image computations when assuming a parallel beam can be damped or removed altogether when calculations are performed which make allowance for a finite divergence. Chapter 4 considers divergent illumination from a theoretical point of view and it is shown that effective damping of the depth and thickness oscillations should occur if the defect is greater than a distance

$$d = \frac{1}{2\Delta s}$$

from either surface, where $\Delta s = g\Delta\theta$ is the spread in the deviation parameter s introduced by a finite divergence $\Delta\theta$ in the incident beam.

Chapter 5 calculates the images of single undissociated and dissociated dislocations in copper including the effect of a finite beam divergence. The predictions of Chapter 4 concerning the damping of the oscillations and the above formula for d are shown to be valid in these cases. The effect of anisotropy on the symmetry of images of dissociated dislocations is considered and the results of the image

calculations are also used to analyse the author's experimental observations of dissociated dislocations in copper. The result obtained for the stacking-fault energy is

$$\gamma = 44 \text{ erg cm}^{-2} .$$

This result is dependent on the assumption that the partial dislocation cores are singular. The effect of a finite core extension on this value is discussed, and it is argued that the good agreement between this figure and that deduced from the studies of faulted dipoles in Chapter 3 is evidence supporting the view that core extension effects are negligible in faulted dipoles and dissociated edge dislocations in this material.

Chapter 6 considers the dissociation of the Frank partial dislocation into a stair-rod and a Shockley partial. Such a dissociation is thought to occur in small Frank loops in heavy-ion irradiated copper, but previous weak-beam investigations have not resolved the partials due to the presence of stacking-fault contrast. In theory $\{113\}$ reflections at the (110) pole should image both partials but not the stacking faults. To simplify the computer simulation of experimental micrographs when investigating these new diffraction conditions, very large faulted Frank loops in copper and copper-aluminium alloys were grown by electron irradiation at elevated temperatures in a high-voltage electron microscope. The partials in any one dissociated side can then be simply represented by two infinite straight dislocations and the effect of the rest of the loop is ignored. The weak-beam images in general show two peaks corresponding to the two partials; as the dissociation always produces an obtuse fault bend, the ribbon of fault between the partials is intrinsic in nature, which suggests that the intrinsic stacking-fault energy is less than the extrinsic in these materials. The images calculated assuming a parallel incident beam of electrons do not agree with the experimental images since two, three or four peaks which

are very sensitive to small changes in defect depth and foil thickness are predicted; these effects are not observed in practice. However, with a finite value of beam divergence the images become more uniform and only two peaks are predicted which exhibit inside-outside contrast effects on reversing $\underline{g}$. Therefore the assumption of a finite beam divergence has proved essential in understanding the images of a dissociated Frank partial, and suitable diffraction conditions have been developed for studying such dissociations which may be applicable to small loops.

Chapter 7 contains general conclusions and suggestions for further work.

Contents

Preface

The work described in this thesis was carried out by the author in the Department of Metallurgy and Science of Materials, Oxford University, between October 1971 and October, 1975, originally under the supervision of Dr. D.J.H. Cockayne, and then under that of Dr. M.J. Whelan following Dr. Cockayne's departure for Australia in April 1974. No part of this work has been submitted for a degree at any other University. From time to time the results of other workers are used in the text with due acknowledgement; a list of references appears at the end of the thesis.

I would like to thank Professor Sir Peter Hirsch, F.R.S., for the provision of laboratory facilities and for the interest he has shown in the work. Special thanks are due to Dr. D.J.H. Cockayne for introducing me to the mysteries of weak-beam electron microscopy, and for his constant encouragement throughout his term as supervisor; and also to Dr. M.J. Whelan for smoothly taking over in this capacity and for many helpful and enlightening discussions.

I have received assistance from many others in the course of this work; in particular I must mention

Mr. C.B. Carter for his excellent experimental work on faulted dipoles, which is analysed in Chapter 3;

Dr. I.L.F. Ray for providing the single copper crystal used in the study of dissociated dislocations in Chapter 5;

Mr. D.G. Wilson for his expertise in producing the specimens containing large faulted loops by irradiation in the high-voltage microscope which were the basis of the work in Chapter 6;

and Dr. M.L. Jenkins and Mr. D.K. Saldin for many stimulating discussions.

Thanks are due to Mr. G. Dixon-Brown and his team of helpers for the excellent microscope maintenance which made possible the ten

minute weak-beam exposure (in a tilting holder!) shown in Chapter 4, and to Mr. A. McKnight for his photographic work.

During the course of this work financial support was provided by the Science Research Council, and A.E.R.E. Harwell.

I am grateful to my mother for her efficient and careful typing of this thesis, and especially to my wife Wendy for her endless encouragement and inspiration.

S.M. Holmes

Brasenose College

October 1975

Some parts of this thesis have been, or are about to be, published as follows:-

(Chapter 4)

Holmes, S.M., Cockayne, D.J.H. and Ray, I.L.F., 1974,

Proc. 8th Int. Cong. Electron Microscopy, Canberra, 1, 290.

(Chapter 3)

Carter, C.B. and Holmes, S.M., 1975a,

Phil. Mag., 32, 599.

Carter, C.B. and Holmes, S.M., 1975b,

Proc. EMAG Conf., Bristol, Institute of Physics (in press)

Part I

The theory of weak-beam electron microscopy of infinite straight dislocations

Chapter 1

The weak-beam method of high-resolution electron microscopy

1.1 The imaging of crystal defects by diffraction contrast

In the transmission electron microscope a crystalline specimen scatters the incident beam of electrons into one or more Bragg diffracted beams corresponding to the various sets of crystal planes. These are then focussed by the objective lens to form a transmission diffraction pattern in its back focal plane. If all these beams were allowed to recombine and interfere, the result should be a resolved image of the lattice planes. In practice an aperture is positioned in the back focal plane of the objective lens to select only the incident beam and one or two first-order Bragg beams which are reasonably near the axis of the lens. This is done because the higher-order beams are subject to sufficiently large lens aberrations to prevent the periodic structure from being resolved. Images so formed display sine fringes with the periodicity of the lattice planes corresponding to the beams included (Menter 1956, 1958). Lattice fringe images of crystals with dislocations can contain terminating and distorted fringes, and it is tempting to associate these directly with a dislocation core and its associated strain field. This has been done by several workers (Parsons, Hoelke and Rainville 1968; Parsons and Hoelke 1969; Phillips and Hugo 1970). These simple interpretations are not confirmed by calculated images which show that the form of fringe bending is sensitive to the depth of the dislocation in the foil, and that for an inclined dislocation several terminating fringes can be expected, the number of these and the entire fringe distribution being dependent on the exact foil thickness and diffraction conditions (Cockayne 1970; Cockayne and Whelan 1970). Experiments confirming these conclusions have been performed in germanium (Cockayne, Parsons and Hoelke 1971). It therefore seems that, although lattice fringe images potentially contain a great deal of information concerning dislocation strain fields, they cannot be interpreted without very precise knowledge of the diffraction conditions, foil thickness and dislocation depth.

An alternative method of imaging crystal defects uses the mechanism of diffraction contrast. Again an aperture is inserted in the back focal plane of the objective lens, but only one beam is selected. This beam can be positioned to coincide with the axis of the lens by the incident beam electromagnetic tilting device which is now a standard fitting on any high-resolution instrument. If the beam selected is the forward-scattered beam, the resulting image is called the bright-field image; images produced by any of the Bragg diffracted beams are called dark-field images. When a suitable set of lattice planes is oriented in the Bragg position, the contrast from a dislocation and the background intensity are considerable in both the bright-field and dark-field images. These are termed strong-beam conditions. There is a dynamical coupling between the direct and diffracted beams even in a perfect crystal. The effect of a strain field surrounding a crystal defect is simply to alter the local diffraction conditions, thus affecting the dynamical coupling and producing contrast in the final image.

This method of imaging defects has been widely applied. Its chief advantage is the high intensity of the images which reduces photographic exposure times to a few seconds at most, thereby avoiding problems of specimen drift and contamination. However, the images are not well suited to high resolution studies since they are not related in any simple way to the defect geometry, and are relatively insensitive to small changes in the strain field. A peak from a dislocation in a strong beam image can be ~ 100 Å wide for 100 keV electrons, yet we may wish to measure the width of dissociation of a dislocation into two partials separated perhaps by only 20 Å. Such a dissociation would be completely masked in a strong-beam image. A useful technique for simulating images, which involves over-printing of computer line-printer characters to create different grey levels, has been described by Head (1967). The result may be reduced photographically and compared with experimental micrographs.

Many strong-beam investigations have used this method; further details and a review of some experiments performed in this manner may be found in Head et al. (1973).

Another method of operation of the electron microscope in the diffraction contrast mode is the weak-beam technique (Cockayne, Ray and Whelan 1969). In this method the diffracted beam selected corresponds to a set of lattice planes which are set far from the Bragg position; the background intensity of a weak-beam image is thus very low. The strain field around a defect may be strong enough to tilt a part of the lattice back into the Bragg position, in which case we expect an image peak. The advantages of this method are that the peak only arises from a small part of the strain field, and so should be narrow, and that since the large strain required is only to be found close to the core of a defect such as an isolated dislocation, the peak should define the position of the defect accurately. Computed images show that under certain conditions the weak-beam image peak of a dislocation is

(i) ~ 15 Å wide at half height

(ii) close to ($\lesssim 20$ Å from) the dislocation core. (Cockayne 1973)

These properties are very useful in experimental studies of defects. They allow complicated networks of dislocations to be resolved, and accurate measurements made of the separations between them. This thesis describes studies of different dislocation geometries by the weak-beam technique and the calculation of equivalent images. The remainder of this chapter is devoted to the theory and practice of the weak-beam method. The image of a crystal defect may be calculated from the dynamical theory of electron diffraction, which has been considered by many authors (e.g. Whelan and Hirsch 1957a,b; Sturkey 1957; Fujimoto 1959; Howie and Whelan 1960, 1961; Takagi 1962; Howie and Basinski 1968). Many of the characteristics of weak-beam images are predicted by the simpler, but less exact, kinematical theory (Hirsch, Howie and Whelan 1960) which will be

discussed in section 1.3. The dynamical theory may be approached in two ways; by a wave-optical (Darwin) method, or on a stricter wave-mechanical basis. Both formulations can express the electron wave function as a sum of Bloch waves, and it is the equivalence of these which justifies the Darwin approach. Section 1.2 considers the scattering of an incident electron wave by an atom, a unit cell, and a crystal lattice; these results are needed for the kinematical theory and the Darwin formalism of the dynamical theory (section 1.4.1). Much of the argument and terminology of sections 1.2-4 is taken from Hirsch et al. (1965).

1.2 The scattering of electrons by a crystal lattice

1.2.1 The atomic scattering factor for electrons

Consider a beam of electrons, wave vector $\underline{k}$, incident upon an isolated atom. Let $\underline{r}'$ be the co-ordinate of any point in the region of the atom, and $\underline{r}$ that of a point some distance from the atom (positioned at the origin) where we wish to calculate the electron wave function $\Psi(\underline{r})$ (see fig. 1.1(a)). $\Psi(\underline{r})$ is the solution of the time-independent Schrödinger equation

$$\frac{\hbar^2}{2m}\nabla^2\Psi(\underline{r}) + |e|(E + V(\underline{r}))\Psi(\underline{r}) = 0 \qquad (1.1)$$

where $-|e|$ is the electron charge

$|e|E$ is the total electron energy

$V(\underline{r})$ is the potential (in volts) at $\underline{r}$.

For the special case of $V(\underline{r}) = 0$, (1.1) has the solution

$$\Psi_o(\underline{r}) = \exp(2\pi i \underline{k}.\underline{r}) \qquad (1.2)$$

where $k^2 = \frac{2m|e|E}{h^2}$.

Dividing $\Psi(\underline{r})$ into two components representing the incident and scattered waves, and assuming (1.2) gives the solution for the incident wave, we have

$$\Psi(\underline{r}) = \Psi_o(\underline{r}) + \Psi_s(\underline{r}) \qquad (1.3)$$

A solution for $\Psi_s(\underline{r})$ is found by substituting (1.3) into (1.1), using a

Green's function method, and making the assumption (the first Born approximation) that $\Psi(\underline{r}') \sim \Psi_o(\underline{r}') = \exp(2\pi i \underline{k}.\underline{r}')$, i.e. that $\Psi_s(\underline{r}') \ll \Psi_o(\underline{r}')$. Then the result for large r is

$$\Psi_s(\underline{r}) = \frac{\exp(2\pi i k r) f(\underline{K}')}{r} \tag{1.4}$$

where $$f(\underline{K}') = \frac{2\pi m |e|}{h^2} \int V(\underline{r}') \exp(-2\pi i \underline{K}'.\underline{r}') d\underline{r}' \tag{1.5}$$

and $\underline{K}' = (\underline{k}' - \underline{k})$ (see fig. 1.1(a)).

This can also be cast in the equivalent form

$$f(\underline{K}') = \frac{1}{2a_o(\pi K')^2} (Z - F_x(\underline{K}')) \tag{1.6}$$

where Z is the atomic number

$a_o = \frac{\epsilon h^2}{\pi m |e|^2}$ is Bohr's radius

and $F_x(\underline{K}')$ is the atomic scattering factor for X-rays.

1.2.2 Electron diffraction from a unit cell and crystal lattice (kinematic approximation).

To calculate the amplitude diffracted by a unit cell it is necessary to know the phase difference between a wave scattered at a point $\underline{r}$ and that scattered at the origin. The extra path length is simply $(\underline{k}.\underline{r} - \underline{k}'.\underline{r})$; therefore the phase factor, $2\pi k$ times this, is given by $\frac{}{k}$ $\exp(-2\pi i \underline{K}'.\underline{r})$. (See fig. 1.1(b)). Then the amplitude diffracted by a unit cell will be

$$A_o(\underline{K}') = \frac{\exp(2\pi i k r)}{r} \sum_i f_i(\underline{K}') \exp(-2\pi i \underline{K}'.\underline{r}_i) \tag{1.7}$$

where there are i atoms in the unit cell with scattering factors $f_i(\underline{K}')$ at positions $\underline{r}_i$. This may be rewritten as

$$A_o(\underline{K}') = \frac{\exp(2\pi i k r)}{r} F(\underline{K}') \tag{1.8}$$

where $$F(\underline{K}') = \sum_i f_i(\underline{K}') \exp(-2\pi i \underline{K}'.\underline{r}_i) \tag{1.9}$$

is called the structure factor of the unit cell.

In the same manner we can derive the scattered amplitude from a crystal lattice. Omitting the factor $\frac{\exp(2\pi ikr)}{r}$,

$$A_c(\underline{K}') \sim \sum_n F_n(\underline{K}')\exp(-2\pi i\underline{K}'.\underline{r}_n) \tag{1.10}$$

where there are n unit cells in the lattice with structure factors $F_n(\underline{K}')$ at positions $\underline{r}_n$, which are some integer combination of the unit cell translation vectors,

$$\underline{r}_n = n_1\underline{a} + n_2\underline{b} + n_3\underline{c} \tag{1.11}$$

Strong diffraction occurs when $\underline{K}'.\underline{r}_n$ is an integer for all $n_1n_2n_3$ (the Laue condition). This condition is satisfied when $\underline{K}'$ coincides with $\underline{g}$, a translation vector of the reciprocal lattice defined by

$$\underline{g} = h\underline{a}^* + k\underline{b}^* + l\underline{c}^*$$

$$\underline{a}^* = \frac{\underline{b}\wedge\underline{c}}{\underline{a}.(\underline{b}\wedge\underline{c})} \quad ; \quad \underline{b}^* = \frac{\underline{c}\wedge\underline{a}}{\underline{b}.(\underline{c}\wedge\underline{a})} \quad ; \quad \underline{c}^* = \frac{\underline{a}\wedge\underline{b}}{\underline{c}.(\underline{a}\wedge\underline{b})} \tag{1.12}$$

and having the property

$$|g| = \frac{1}{d_{hkl}} \tag{1.13}$$

where d_{hkl} is the distance between planes with Miller indices hkl. Using (1.13) and $\underline{K}' = \frac{2\sin\theta}{\lambda}$ we obtain the familiar Bragg law

$$\lambda = 2d_{hkl}\sin\theta \tag{1.14}$$

and so the strong diffraction in question is Bragg diffraction from the hkl planes.

These conditions for diffraction can be expressed in terms of a geometrical construction, in which the Ewald sphere of possible wave vectors $\underline{k}'$ is superimposed on the reciprocal lattice such that the origin is the point where the incident wave vector $\underline{k}$ meets the sphere. Then any vector drawn from the origin to another point on the sphere is a possible $\underline{K}'$ vector. If this point coincides with a reciprocal lattice point then the condition $\underline{K}' = \underline{g}$ will be satisfied and strong diffraction will result. If a reciprocal lattice point does not lie on the sphere, the deviation is

measured by a vector $\underline{s}$ such that

$$\underline{K}' = \underline{g} + \underline{s} \tag{1.15}$$

and by convention $\underline{s}$ is positive if tne point $\underline{g}$ lies inside the sphere. (See fig. 1.1(c)).

It is possible for $\underline{s}$ to be zero in (1.15) but no diffraction occur since $F_n(\underline{K}')$ in (1.10) may be zero. Substituting (1.12) in (1.9) we have

$$F(\underline{g}) = \sum_i f_i(\underline{g}) \exp(-2\pi i(hu_i + kv_i + lw_i)) \tag{1.16}$$

where $u_i v_i w_i$ are the real-space co-ordinates of atom i in the unit cell. For the face-centred cubic lattice this immediately gives the well-known result that hkl must be all even or all odd, in which case $F(\underline{g}) = 4f(\underline{g})$ (if each atom has the same scattering factor); otherwise the reflection is absent.

1.2.3 The amplitude scattered by a crystal plane and the column approximation

Equation (1.10) gives the amplitude a long way from the crystal, effectively at infinity. However, we are more interested in the intensity distribution at the bottom surface of the crystal which is imaged by the lenses and projected on the final screen. To calculate this we split the crystal into elemental layers parallel to the surface and consider the amplitude of the diffracted wave at the bottom surface due to any one of these; the total effect may be found by summation. The manner in which this last step is performed dictates whether we have a kinematical or dynamical theory of diffraction.

Each elemental volume of the layer gives rise to a spherical wavelet and these combine to form a plane wave, as may be seen by splitting the layer into Fresnel zones and constructing an amplitude-phase diagram of the disturbance at the required point P. The diagram starts as a circle and becomes a convergent spiral as the amplitude falls off from the outer Fresnel zones (see fig. 1.2(a)). The resultant is $\pi/2$ out of phase with

the wavelet scattered from the centre of the zones and is half the magnitude of the resultant effect of the first zone, whose area is $\frac{\pi r \lambda}{\cos\theta}$ when P is a point at distance r. The scattered wave at P from a thickness δz is therefore

$$\frac{i}{\pi}\frac{\exp(2\pi ikr)}{r}F(\underline{K}')\frac{\delta z}{V_c}\frac{\pi r\lambda}{\cos\theta} \longrightarrow \frac{i\lambda F(\underline{K}')}{V_c\cos\theta}\exp(2\pi ikr)\delta z \qquad (1.17)$$

times the incident wave, where V_c is the volume of a unit cell. Applying the result to the geometry of fig. 1.2(b) where the origin is at the top surface, and we require the amplitude $d\Psi_g$ at $\underline{r}$ due to the crystal thickness δz at $\underline{r}_n$, the exponential term in (1.17) becomes $\exp(2\pi i\underline{k}'.(\underline{r} - \underline{r}_n))$ and the incident wave at $\underline{r}_n$ is $\exp(2\pi i\underline{k}.\underline{r}_n)$; therefore

$$d\Psi_g(\underline{r}) = \frac{i\lambda F(\underline{g})}{V_c\cos\theta}\exp(2\pi i\underline{k}'.(\underline{r} - \underline{r}_n))\exp(2\pi i\underline{k}.\underline{r}_n)\,\delta z$$

$$= \frac{i\lambda F(\underline{g})}{V_c\cos\theta}\exp(-2\pi i\underline{K}'.\underline{r}_n)\exp(2\pi i\underline{k}'.\underline{r})\,\delta z \qquad (1.18)$$

This is usually written

$$d\Psi_g(\underline{r}) = \frac{i\pi}{\xi_g}\exp(-2\pi i\underline{K}'.\underline{r}_n)\exp(2\pi i\underline{k}'.\underline{r})\,\delta z \qquad (1.19)$$

where ξ_g has dimensions of length and is called the extinction distance.

$$\xi_g = \frac{\pi V_c\cos\theta}{\lambda F(\underline{g})} \qquad (1.20)$$

The equivalent equations for forward scattering are

$$d\Psi_o(\underline{r}) = \frac{i\pi}{\xi_o}\exp(2\pi i\underline{k}.\underline{r})\,\delta z \qquad (1.21)$$

and $$\xi_o = \frac{\pi V_c\cos\theta}{\lambda F(0)} \qquad (1.22)$$

Equations (1.19) and (1.21) can be applied to an imperfect crystal by rewriting $$\underline{r}_n \longrightarrow \underline{r}_n + \underline{R} \qquad (1.23)$$

where $\underline{R}$ is the displacement. From the derivation of (1.19) where contributions from a whole plane are considered it would seem that this is only appropriate in the case where $\underline{R}$ is a function of z only. However, most of the contributions come from the first few Fresnel zones, perhaps ~20 Å for a crystal 1000 Å thick, so if $\underline{R}$ does not vary appreciably over

this distance we may apply (1.23) in cases where $\underline{R}$ is a function of a lateral co-ordinate as well. In other words, we can assume that the amplitude at P only comes from a narrow column of crystal parallel to the diffracted wave. This is the so-called column approximation. All the theoretical image computations presented in this thesis make use of it. This can be avoided (e.g. Takagi 1962) in which case the intensity at the lower surface can be shown to depend only on a triangle of crystal enclosed by the incident and diffracted wave vectors whose apex is at the point in question. The smallness of the Bragg angle again indicates that the approximation is justified if $\underline{R}$ does not vary too rapidly in the lateral direction.

1.3 The image contrast of crystal defects: kinematical theory

The basic assumption of the kinematical theory is that the amplitude of the incident wave is much greater than that of the diffracted wave, and is approximately unity everywhere in the crystal. Then (1.19), which is written for unit amplitude of the incident wave, applies for all $\underline{r}_n$ and may simply be integrated. As the propagation factor is a constant it is usual to remove it at this stage by writing

$$\Psi(\underline{r}) = \phi_o(z)\exp(2\pi i\underline{k}.\underline{r}) + \phi_g(z)\exp(2\pi i\underline{k}'.\underline{r}) \qquad (1.24)$$

Then (1.19) becomes

$$d\phi_g(z) = \frac{i\pi}{\xi_g}\exp(-2\pi i\underline{K}'.\underline{r}_n)\,\delta z \qquad (1.25)$$

Equations (1.15) and (1.23) give, for an imperfect crystal,

$$\exp(-2\pi i\underline{K}'.\underline{r}_n) \rightarrow \exp(-2\pi i(\underline{g}.\underline{r}_n + \underline{g}.\underline{R} + \underline{s}.\underline{r}_n + \underline{s}.\underline{R}))$$
$$\sim \exp(-2\pi i(\underline{g}.\underline{R} + sz)) \qquad (1.26)$$

Substituting (1.26) in (1.25) and integrating gives

$$\phi_g = \frac{i\pi}{\xi_g}\int_o^t \exp(-2\pi i\underline{g}.\underline{R})\exp(-2\pi isz)\,dz \qquad (1.27)$$

which is the integral basic to the kinematical theory of imperfect crystals.

For a perfect crystal $\underline{R} = 0$ and (1.27) can be integrated to give

$$\phi_g = \frac{i\pi}{\xi_g}\,\frac{\sin(\pi ts)}{\pi s}\exp(-\pi ist) \qquad (1.28)$$

Therefore the intensity in the diffracted beam g is given by

$$I_g = |\phi_g|^2 = \left(\frac{\pi}{\xi_g}\right)^2 \frac{\sin^2(\pi t s)}{(\pi s)^2} \qquad (1.29)$$

Conservation of electron flux gives the incident beam intensity as

$$I_o = 1 - I_g = 1 - \left(\frac{\pi}{\xi_g}\right)^2 \frac{\sin^2(\pi t s)}{(\pi s)^2} \qquad (1.30)$$

If the crystal is in the Bragg position, (1.29) reduces to $I_g = \left(\frac{\pi t}{\xi_g}\right)^2$, in which case the condition that $I_g \ll 1$ is only valid for $t \ll \frac{\xi_g}{\pi}$, ~ 100 Å. Therefore the kinematical theory can only be used in strong-beam conditions for very thin crystals. The $\frac{\sin^2(\pi t s)}{(\pi s)^2}$ curve of (1.29) is plotted against s in fig. 1.3(a). The subsidiary maxima, whose peaks lie on a $\left(\frac{1}{\pi s}\right)^2$ curve, occur at intervals of $\Delta s = \frac{1}{t}$. In fig. 1.3(b) the curve is reproduced in a reciprocal lattice and Ewald sphere diagram (section 1.2.2), the s = 0 point being the reciprocal lattice point. The resulting intensity can be read off the curve where the s axis cuts the sphere. This then explains two common effects:-

(i) Thickness fringes. s remains fixed but different thicknesses cause the function to expand or contract, sweeping maxima and minima through the sphere. The condition for a minimum is $s = \frac{n}{t}$; therefore the fringes have a periodicity $\Delta t = \frac{1}{s}$.

(ii) Bend contours. The scale of the curve (determined by thickness) is constant but different parts of the crystal have different s values, again causing various parts of the function to cut the sphere. The subsidiary fringes occur in regions of the crystal having s values differing by $\Delta s = \frac{1}{t}$. This relation can be used to determine the thickness.

The integration in (1.27) can be performed graphically using an amplitude-phase diagram for both a perfect and an imperfect crystal. (Hirsch, Howie and Whelan 1960). For a perfect crystal this is simply a circle of radius $1/2\pi s$. The amplitude diffracted by a crystal thickness t is

proportional to a line joining the origin to the point found by moving round the circumference from the origin a distance t (see fig. 1.4(a)). For an imperfect crystal there is an additional phase factor α given by

$$\alpha = 2\pi \underline{g}.\underline{R} \tag{1.31}$$

In the case of a stacking fault there is perfect crystal above and below the fault plane, and these regions correspond to circles in the amplitude-phase diagram. After traversing the circumference of the first circle by a distance corresponding to the depth of the fault, there will be an abrupt change of angle given by α on to the second circle for the rest of the crystal (see fig. 1.4(b)). For an inclined fault, points which differ in height by 1/s (one complete circumference) will have the same resultant amplitude, and so the contrast will be in the form of fringes with this periodicity. From (1.31) we see that faults for which $\underline{g}.\underline{R}$ is an integer will be effectively invisible since no jump in angle occurs.

In the case of dislocations $\underline{R}$ is a continuously varying function of z. General methods of calculating $\underline{R}$ are presented in Chapter 2, but the characteristics of a dislocation image in the kinematical theory can best be discussed using a specific example: a screw dislocation in the isotropic approximation for which

$$\underline{R} = \frac{\underline{b}}{2\pi} \tan^{-1}\frac{(z - y)}{x} \qquad \text{(See fig. 1.5(a))} \tag{1.32}$$

Then (1.31) gives

$$\alpha = \underline{g}.\underline{b} \tan^{-1}\frac{(z - y)}{x} \tag{1.33}$$

which indicates that the dislocation is invisible for $\underline{g}.\underline{b} = 0$. The amplitude-phase diagram for the top of the crystal is asymptotic to a perfect crystal circle, as is that for the bottom. The angle α when near the dislocation will either reduce the effect of the $2\pi sz$ term in (1.27), in which case the initial and final circles will be positioned far from each other (fig. 1.5(b)); or it will enhance it, causing the circles to overlap (fig. 1.5(c)). For a given sign of $\underline{g}.\underline{b}$, the difference between the two cases depends on the sign of sx, i.e. on which side of the dislocation the column in question is situated. Clearly the former case will tend to give

amplitudes higher than those from a perfect crystal, whereas the latter will not be significantly different. This gives a peak on one side of the dislocation, a result which can be used to determine the sign of $\underline{b}$ in practice. The line joining the centres of the initial and final circles gives a measure of the average amplitude expected, neglecting depth and thickness oscillation effects. The scale of the whole diagram is inversely proportional to s; therefore the intensity in a particular column is inversely proportional to s^2 . Plotting the average intensity as a function of column position gives a measure of the half-width of the peak, Δx, and the peak position, X_k . The latter figure is simply the value of x which maximises the distance between the circle centres. In the present case (screw dislocation) and for $\underline{g}.\underline{b} = 2$, the values are

$$\Delta x \sim \frac{1}{\pi s} \quad ; \quad X_k = \frac{-1}{2\pi s} \tag{1.34}$$

(Hirsch, Howie and Whelan 1960)

1.4 The image contrast of crystal defects: dynamical theory

1.4.1 The wave-optical formalism

In this approach we may assume n beams to be excited, but again remove the propagation factors in a similar manner to (1.24) by writing

$$\Psi(\underline{r}) = \sum_g \phi_g(z)\exp(2\pi i(\underline{k} + \underline{g} + \underline{s}_g).\underline{r}) \tag{1.35}$$

Using (1.25) and (1.26) to describe the scattering between any two beams in thickness dz gives

$$\frac{d\phi_g}{dz} = \sum_h \frac{i\pi}{h\xi_{g-h}} \phi_h \exp(-2\pi i(\underline{g} - \underline{h}).\underline{R})\exp(-2\pi i(s_g - s_h)z) \tag{1.36}$$

where ξ_{g-h} is the extinction distance for scattering from beam h to g . The n differential equations of (1.36) may be recast into many equivalent forms by using different wave amplitudes related to the set ϕ_g by phase factors (which do not affect the intensities). For example, the substitution

$$\phi_g \rightarrow \phi'_g \exp(-2\pi i s_g z + \frac{\pi i z}{\xi_o}) \tag{1.37}$$

in (1.36) gives

$$\frac{d\phi'_g}{dz} = (2\pi i s_g - \frac{i\pi}{\xi_o})\phi'_g + \sum_h \frac{i\pi}{h\xi_{g-h}} \phi'_h \exp(-2\pi i(\underline{g} - \underline{h}).\underline{R}) \tag{1.38}$$

and in (1.35)

$$\Psi(\underline{r}) = \sum_g \phi'_g(z)\exp(2\pi i(\underline{K} + \underline{g}).\underline{r}) \qquad (1.39)$$

where $\underline{K}$ is the incident wave vector in the crystal, related to the vacuum wave vector $\underline{k}$ by

$$K_x = k_x \quad ; \quad K_y = k_y \quad ; \quad K_z = k_z + 1/2\xi_o \qquad (1.40)$$

The solution of (1.36) in the two-beam approximation for a perfect crystal is straightforward and gives

$$|\phi_g|^2 = \left(\frac{\pi}{\xi_g}\right)^2 \frac{\sin^2(\pi t s_{eff})}{(\pi s_{eff})^2} \qquad \text{where } s_{eff} = \sqrt{s^2 + \left(\frac{1}{\xi_g}\right)^2} \qquad (1.41)$$

This is identical to (1.29) of the kinematical theory, except that s_{eff} replaces s. For $s = 0$, (1.41) gives $|\phi_g|^2 = \sin^2\left(\frac{\pi t}{\xi_g}\right)$, and clearly this can be valid for any thickness of crystal, unlike the kinematic expression. For a crystal deviated from the Bragg position, the intensity oscillations have a periodicity of the effective extinction distance, defined as

$$\xi_g^{\,w} = \frac{1}{s_{eff}} = \frac{1}{\sqrt{s^2 + \left(\frac{1}{\xi_g}\right)^2}} \qquad (1.42)$$

All the equations derived so far have assumed that the electrons are scattered elastically by the atoms into one or more Bragg beams. Inelastically scattered electrons may also pass through the objective aperture and reach the image. Some of these give the same contrast effects as predicted for elastic scattering (Kamiya and Uyeda 1961; Howie 1963), but the effect of the others is neglected in the above theory. Many electrons are scattered outside the aperture and so do not contribute to the image at all, and this effect can be incorporated, phenomenologically, by writing

$$\frac{1}{\xi_g} \rightarrow \frac{1}{\xi_g} + \frac{i}{\xi'_g} \qquad (1.43)$$

in (1.38) and (1.39). This gives an effective absorption of electrons with depth in the crystal.

1.4.2 The wave-mechanical formalism: perfect crystal

In this approach the potential in a perfect crystal is written as

$$V(\underline{r}) = \sum_g V_g \exp(2\pi i \underline{g}.\underline{r}) = \frac{h^2}{2m|e|} \sum_g U_g \exp(2\pi i \underline{g}.\underline{r}) \qquad (1.44)$$

and we look for solutions of Schrödinger's equation of the form

$$\Psi(\underline{r}) = \sum_j \psi^{(j)} \sum_g C_g^{(j)} \exp(2\pi i(\underline{k}^{(j)} + \underline{g}).\underline{r}) \qquad (1.45)$$

where the amplitude $\psi^{(j)}$ of the Bloch wave with vectors $(\underline{k}^{(j)} + \underline{g})$ is constant. Substituting (1.44) and (1.45) into (1.1) and recalling that $k^2 = \frac{2m|e|E}{h^2}$ gives

$$\sum_j \psi^{(j)} \sum_g (((k^2 + U_o - (\underline{k}^{(j)} + \underline{g})^2) C_g^{(j)} + \sum_{p, p \neq g} U_{g-p} C_p^{(j)})(\exp(2\pi i(\underline{k}^{(j)} + \underline{g}).\underline{r}))) = 0 \qquad (1.46)$$

Equating the coefficient of each exponential term to zero gives a set of n equations

$$(K^2 - (\underline{k}^{(j)} + \underline{g})^2) C_g^{(j)} + \sum_{p, p \neq g} U_{g-p} C_p^{(j)} = 0 \qquad (1.47)$$

where $K^2 = k^2 + U_o$

This may be written in matrix form

$$\underline{\underline{D}}^{(j)} \underline{C}^{(j)} = 0 \qquad (1.48)$$

where $\underline{\underline{D}}$ has terms on the diagonal $D_{gg} = K^2 - (k^{(j)} + g)^2$

off the diagonal $D_{gp} = U_{g-p}$, and $\underline{C}$ is the column vector $C_g^{(j)}$

A solution of (1.48) only exists if the determinant

$$[D] = 0 \qquad (1.49)$$

which is the dispersion equation for the wave vectors $\underline{k}^{(j)}$, limiting them to certain values. A pictorial representation of this is the dispersion surface, drawn for the two-beam case in fig. 1.6. The two branches corresponding to j = 1,2 are asymptopic to spheres of radius K centred on $\underline{O}$ and $\underline{g}$. Comparison of the definition of K^2 in (1.47) with (1.2) shows that K is the magnitude of the incident wave vector after refraction by the mean crystal potential; it is thus the vector defined in (1.40). These two definitions are compatible if

$$\xi_g = \frac{K}{U_g} \qquad (1.50)$$

since, by geometry, $K^2 - k^2 \sim (K_z - k_z)2K$. Now we define the new quantity

$\gamma^{(j)}$ by

$$\gamma^{(j)} = k_z^{(j)} - K_z \tag{1.51}$$

Then the expressions for the electron wave function in the Darwin and Bloch-wave formalisms, (1.39) and (1.45), are identical if

$$\phi_g'(z) = \sum_j \psi^{(j)} C_g^{(j)} \exp(2\pi i \gamma^{(j)} z) \tag{1.52}$$

As mentioned in section 1.1, it is the fact that the two formalisms can be shown to be identical which justifies the Darwin approach.

Equation (1.51) shows that $\gamma^{(j)}$ is the distance in the z direction from the point A to the wave point for $\underline{k}^{(j)}$. Again by geometry we have

$$K^2 - (\underline{k}^{(j)} + \underline{g})^2 \sim 2K(s_g - \gamma^{(j)})\cos\theta_g \tag{1.53}$$

Substituting in (1.47) gives

$$\sum_{p,p\neq g} \frac{U_{g-p}}{2K\cos\theta_g} C_p^{(j)} + s_g C_g^{(j)} - \gamma^{(j)} C_g^{(j)} = 0 \tag{1.54}$$

Alternatively, in matrix notation

$$\underline{\underline{A}}\ \underline{C}^{(j)} - \gamma^{(j)} \underline{C}^{(j)} = 0 \tag{1.55}$$

where $\underline{\underline{A}}$ has terms on the diagonal $A_{gg} = s_g$

off the diagonal $A_{gp} = \frac{U_{g-p}}{2K\cos\theta_g} \sim \frac{1}{2\xi_{g-p}}$ from (1.50).

This shows that $C_g^{(j)}$ is the g^{th} element of the j^{th} eigenvector of the matrix $\underline{\underline{A}}$, and $\gamma^{(j)}$ is the j^{th} eigenvalue. We can also define a matrix $\underline{\underline{C}}$ with $C_{gj} = C_g^{(j)}$. Then if a diagonal matrix is denoted by curly brackets,

$$\underline{\underline{A}}\ \underline{\underline{C}} = \underline{\underline{C}}\ \{\gamma^{(j)}\} \tag{1.56}$$

The amplitudes of the various beams at the bottom of a crystal thickness z can now be obtained. In matrix form (1.52) is

$$\underline{u}(z) = \underline{\underline{C}}\ \{\exp(2\pi i \gamma^{(j)} z)\}\ \underline{\Psi} \tag{1.57}$$

where $\underline{u}(z)$ is the column vector of beam amplitudes $\phi_g'(z)$. At z = 0, (1.57) gives $\underline{\Psi} = \underline{\underline{C}}^{-1}\ \underline{u}(0)$; therefore

$$\underline{u}(z) = \underline{\underline{C}}\ \{\exp(2\pi i \gamma^{(j)} z)\}\ \underline{\underline{C}}^{-1}\ \underline{u}(0) \tag{1.58}$$

Absorption can again be included by using (1.43), which together with (1.50) and (1.44) can be seen to make the crystal potential complex by writing

$$U_g \longrightarrow U_g + iU_g' \tag{1.59}$$

whereupon (1.54) becomes

$$\sum_{p,p\neq g} \frac{U_{g-p}}{2K\cos\theta_g} C_p^{(j)} + i\sum_p \frac{U'_{g-p}}{2K\cos\theta_g} + s_g C_g^{(j)} - \gamma^{(j)} C_g^{(j)} = 0 \qquad (1.60)$$

and (1.55) still applies for a new matrix $\underline{A}$ where $A_{gg} = s_g + \frac{iU'_o}{2K\cos\theta_g} \sim s_g + \frac{i}{2\xi'_o}$

$$A_{gp} = \frac{1}{2\xi_{g-p}} + \frac{i}{2\xi'_{g-p}}$$

1.4.3 The wave-mechanical formalism: imperfect crystal

The displacement $\underline{R}$ in an imperfect crystal may be included by using the deformable-ion approximation for the potential,

$$V(\underline{r}) = \frac{h^2}{2m|e|} \sum_g (U_g \exp(-2\pi i \underline{g}.\underline{R}))\exp(2\pi i \underline{g}.\underline{r}) \qquad (1.61)$$

and writing the wave function as

$$\Psi(\underline{r}) = \sum_j \psi^{(j)}(z) \sum_g C_g^{(j)} \exp(2\pi i(\underline{k}^{(j)} + \underline{g}).\underline{r})\exp(-2\pi i \underline{g}.\underline{R}) \qquad (1.62)$$

where the wave amplitude $\psi^{(j)}(z)$ is now a variable. Matrix forms can again be used (Howie and Whelan 1961). Firstly we define

$$\beta_g = \underline{g}.\underline{R} \quad ; \quad \beta'_g = \underline{g}.\frac{d\underline{R}}{dz} \quad ; \quad \underline{Q} = \{\exp(2\pi i \beta g)\} \qquad (1.63)$$

Comparison of (1.61) with (1.44), and (1.62) with (1.45), suggests that the same equations may be used as in the perfect crystal case if we rewrite

$$U_g \longrightarrow U_g \exp(-2\pi i \beta_g) \quad ; \quad C_g^{(j)} \longrightarrow C_g^{(j)} \exp(-2\pi i \beta_g) \qquad (1.64)$$

These expressions can be incorporated in the matrices $\underline{A}$ and $\underline{C}$ by rewriting

$$\underline{A} \longrightarrow \underline{Q}^{-1}\,\underline{A}\,\underline{Q} \quad ; \quad \underline{C} \longrightarrow \underline{Q}^{-1}\,\underline{C} \qquad (1.65)$$

Then (1.57) for an elemental thickness δz becomes

$$\underline{u}(\delta z) = \underline{Q}^{-1}\,\underline{C}\,\{\exp(2\pi i \gamma^{(j)}\delta z)\}\,\underline{\Psi}$$

$$= \underline{Q}^{-1}\,\underline{C}\,\{\exp(2\pi i \gamma^{(j)}\delta z)\}\,\underline{C}^{-1}\,\underline{Q}\,\underline{u}(0) \qquad (1.66)$$

Equation (1.66) may be used in conjunction with the column approximation (section 1.2.3), when the crystal is divided into perfect lamellae parallel to the surface but with relative displacements given by $\underline{R}$, to calculate the intensity at the bottom of an imperfect crystal. It can be expressed as a differential equation by writing $\{\exp(2\pi i \gamma^{(j)}\delta z)\} \sim \underline{1} + 2\pi i \{\gamma^{(j)}\}\,\delta z$. Then

$$\delta \underline{u} = \underline{u}(\delta z) - \underline{u}(0)$$

$$= \underline{\underline{Q}}^{-1}\ \underline{\underline{C}}\ (\underline{\underline{1}} + 2\pi i \{\gamma^{(j)}\}\ \delta z)\ \underline{\underline{C}}^{-1}\ \underline{\underline{Q}}\ \underline{u}(0)$$

$$= \underline{\underline{Q}}^{-1}\ \underline{\underline{C}}\ 2\pi i \{\gamma^{(j)}\}\ \underline{\underline{C}}^{-1}\ \underline{\underline{Q}}\ \underline{u}(0)\ \delta z$$

$$\therefore \quad \frac{d\underline{u}}{dz} = 2\pi i\ \underline{\underline{Q}}^{-1}\ \underline{\underline{A}}\ \underline{\underline{Q}}\ \underline{u}(0) \qquad \text{using (1.56).} \tag{1.67}$$

The matrices $\underline{\underline{A}}$ and $\underline{\underline{C}}$ in these equations are those for perfect crystal.

A differential equation for the Bloch wave amplitudes may also be derived. Making a transformation

$$\underline{v} = \underline{\underline{Q}}\ \underline{u} \tag{1.68}$$

and substituting in (1.67) gives

$$\frac{d\underline{v}}{dz} = 2\pi i(\underline{\underline{A}} + \{\beta'_g\})\underline{v} \tag{1.69}$$

Combining (1.66) and (1.68) gives

$$\underline{v} = \underline{\underline{C}}\ \{\exp(2\pi i\, \gamma^{(j)} z)\}\ \underline{\Psi} \tag{1.70}$$

Differentiation of (1.70), and use of (1.56) and (1.69) gives

$$\frac{d\underline{\Psi}}{dz} = 2\pi i\ \{\exp(-2\pi i\, \gamma^{(j)} z)\}\ \underline{\underline{C}}^{-1}\ \{\beta'_g\}\ \underline{\underline{C}}\ \{\exp(2\pi i\, \gamma^{(j)} z)\}\ \underline{\Psi} \tag{1.71}$$

or in summation form,

$$\frac{d\Psi^{(j)}}{dz} = \sum_l \Psi^{(l)}(z) \sum_g (2\pi i \underline{g} \cdot \frac{d\underline{R}}{dz}\, C_g^{(j)} \cdot C_g^{(l)}) \exp(2\pi i (k_z^{(l)} - k_z^{(j)}) z) \tag{1.72}$$

The changes in $\Psi^{(j)}$ depend on $\Psi^{(j)}$ itself (intraband scattering) and on $\Psi^{(l)}$ $(l \neq j)$ (interband scattering).

1.5 Electron diffraction theory of weak-beam microscopy

1.5.1 Introduction

In the weak-beam method the diffracted beam selected by the objective aperture corresponds to a set of lattice planes which are far from the Bragg position. Therefore in regions of perfect crystal the deviation parameter s is large and the diffracted intensity small. A defect strain field may cause the reciprocal lattice point to be locally tilted towards the Ewald sphere resulting in a relatively large diffracted intensity. This interpretation of weak-beam imaging suggests that the image peaks should be associated with a particular value of the strain field, be narrow,

and lie close to defect cores. These properties are very desirable for high-resolution studies. The technique was first proposed by Cockayne, Ray and Whelan (1969). The next section considers the theory of weak-beam images and is based on Whelan (1971) and Cockayne (1972).

1.5.2 Bloch-wave analysis of weak-beam images

First we define

$$T^{jl}(z) = 2\pi i \sum_g \underline{g}.\underline{R}(z) C_g^{(j)*} C_g^{(l)} \quad ; \quad \Delta k^{jl} = k_z^{(l)} - k_z^{(j)} \tag{1.73}$$

Then by expanding $\frac{d}{dz}(\psi^{(j)}(z)\exp(-T^{jj}(z)))$, integrating both sides and using (1.72) we obtain

$$\psi^{(j)}(t)\exp(-T^{jj}(t)) - \psi^{(j)}(0)\exp(-T^{jj}(0)) = \int_0^t \sum_{l\neq j} \psi^{(l)}(z)\frac{dT^{jl}(z)}{dz}\exp(-T^{jj}(z)).$$
$$.\exp(2\pi i\Delta k^{jl}z)dz \tag{1.74}$$

Next we assume that the $\psi^{(l)}$ are all constant. Then on integrating by parts we obtain

$$\psi^{(j)}(t) = \exp(T^{jj}(t))\Big[\psi^{(j)}(0)\exp(-T^{jj}(0)) + \sum_{l\neq j} B^{jl}\psi^{(l)}\{\exp(-T^{jj}(0))$$
$$-\exp(-T^{jj}(t))\exp(2\pi i\Delta k^{jl}t) + 2\pi i\Delta k^{jl}\int_0^t \exp(-T^{jj}(z))\exp(2\pi i\Delta k^{jl}z)dz\}\Big] \tag{1.75}$$

where $B^{jl} = T^{jl}(z)/T^{jj}(z) = \sum_n nC_n^{(j)*}C_n^{(l)} \Big/ \sum_n nC_n^{(j)*}C_n^{(j)}$.

The condition that all $\psi^{(l\neq j)}$ are constant, when applied to (1.70), gives the change in v_g due to the interband scattering to $\psi^{(j)}$ as

$$|\Delta v_g| = |\Delta\psi^{(j)}C_g^{(j)}| \tag{1.76}$$

The condition for g to be a weak beam is that $|\phi_g'| = |v_g| \ll 1$ in the perfect lattice, i.e. $|\psi^{(l)}C_g^{(l)}| \ll 1$ for all l and z . Then a more general interpretation of (1.76) is that appreciable weak-beam contrast for a reflection g occurs for those conditions which produce strong interband scattering from the branch of the dispersion surface with largest $|\psi^{(l)}(0)|$ to that with largest $C_g^{(j)}$. It is convenient to number the branches of the dispersion surface such that branch j is that closest to the sphere of radius K centred on the reciprocal lattice point j. The branch centred on

the origin is branch 1 . Then the matrix $\underline{C}$ is close to diagonal for the weak-beam case when all $|s_j|$ are large and appreciably different, and the off-diagonal elements are given by perturbation theory as $|C_j^{(i)}| \sim \left|\frac{1}{2\xi_{i-j}(s_i-s_j)}\right|$ (Cockayne 1972). With this terminology it can be seen that most of the weak-beam contrast arises by scattering from Bloch wave 1 to Bloch wave g . From the matrix $\underline{C}$, $|\psi^{(k)}| \sim \left|\frac{1}{2\xi_k s_k}\right|$. Then $|\psi^{(k)}| \ll |\psi^{(1)}|$ if $\left|\frac{1}{2\xi_k s_k}\right| \ll 1$. As ξ_k increases with k , this is normally a condition on the first-order beam, which in most cases is the weak beam g . The parameter $w = s_g \xi_g$ cannot be made too great since the absolute intensity decreases; computed and experimental images indicate that $|w| \sim 5$ is a reasonable compromise. Therefore the fundamental condition for weak-beam images is that

$$|w| \gg 5 \qquad (1.77)$$

1.5.3 The properties of weak-beam images

Substitution of (1.75) into (1.70) and (1.68) gives the general expression for the weak-beam amplitude $\phi_g'(t)$. In terms of the parameter

$$D^{jl}(z) = B^{jl} C_g^{(j)} \exp(2\pi i \gamma^{(j)} z) \exp(T^{jj}(z)) \psi^{(l)}(0) \qquad (1.78)$$

it is

$$\phi_g'(t) = \exp(-2\pi i \underline{g}.\underline{R}(t)) \left[\sum_{l \neq g} \exp(2\pi i \gamma^{(l)} t) \psi^{(l)} (C_g^{(l)} - C_g^{(g)} B^{gl}) + \sum_l D^{gl}(t) \exp(-T^{gg}(0)) \right.$$
$$\left. + \sum_{l \neq g} D^{gl}(t) 2\pi i \Delta k^{gl} \int_0^t \exp(-T^{gg}(z)) \exp(2\pi i \Delta k^{gl} z)\, dz \right] \qquad (1.79)$$

The maximum intensity occurs in the column for which $\underline{R}(z)$ is such that the square bracket term in (1.79) has the largest modules.

In the two-beam case the first two terms of (1.79) are zero. Then the maximum intensity arises when the integral is a maximum; for $|s_g| \longrightarrow \infty$ (1.79) becomes

$$\phi_g'(t) \underset{\text{2-beam}}{\longrightarrow} \frac{i\pi}{\xi_g} \exp(2\pi i s t) \int_0^t \exp(-2\pi i \underline{g}.\underline{R}(z)) \exp(-2\pi i s z)\, dz \qquad (1.80)$$

which is essentially the same as (1.27). Therefore weak-beam peak positions

are approximately given by the kinematical theory (section 1.3). Alternatively, (1.80) is a maximum if $sz + \underline{g}.\underline{R}(z)$ is a constant, or $s + \underline{g}.\frac{d\underline{R}}{dz} = 0$, over the whole range 0 to t . Such a displacement merely rotates the whole perfect crystal into the Bragg position. In practice $\underline{g}.\frac{d\underline{R}(z)}{dz}$ has a range of values in any one column, with a maximum where $\frac{d}{dz}\left(\underline{g}.\frac{d\underline{R}(z)}{dz}\right) = 0$. This suggests another criterion for the peak position: the peak occurs in the column for which, at some specific depth,

$$s_g + \underline{g}.\left(\frac{d\underline{R}(z)}{dz}\right) = 0 \quad ; \quad \frac{d}{dz}\left(\underline{g}.\left(\frac{d\underline{R}(z)}{dz}\right)\right) = 0 \qquad (1.81)$$

(Cockayne, Ray and Whelan 1969)

These criteria give different results; for example, in the case of isotropic elasticity and a screw dislocation with $\underline{g}.\underline{b} = 2$, (1.81) gives the peak column co-ordinate as $X_w = \frac{-1}{\pi s_g}$, whereas the kinematic result (1.34) is $X_k = \frac{-1}{2\pi s_g}$. This difference arises because the latter finds the column where on average the reciprocal lattice point is nearest the Ewald sphere, and so predicts a peak nearer the core where the tilt overcompensates s_g . Many-beam calculations generally give the actual peak position as lying between the two predictions and oscillating with a periodicity given by the effective extinction distance (1.42). For $|s_g| \gg 2.10^{-2}$ Å^{-1} , (1.81) gives the peak position to an accuracy of $\leqslant 10$ Å (Cockayne 1970, 1973). If it is wished to use one of these criteria, (1.81) is easier to apply. However, it must be emphasised that both predictions are only an approximation to the many-beam, finite s_g case given in (1.79), and the results could be misleading for certain types of strain field.

The image half-width and intensity may both be estimated from kinematical theory. As already discussed (section 1.3) , the half-width is inversely proportional to s_g (e.g.(1.34)) , and the intensity to s_g^2 . Fig. 1.5(b) also predicts oscillations in the intensity of periodicity $1/s_g$ with both defect depth and foil thickness. These predictions are confirmed

by many-beam computations (with s_g replaced by s_{eff}, (1.42)) , and by experiment (Cockayne 1970, 1973).

1.6 The practical details of weak-beam experimentation

Most experiments involving the electron microscope at some stage call for the comparison of micrographs with theoretical images. Sections 1.3 and 1.4 outlined two theories of electron diffraction which enable this to be done; and in section 1.5.3 it was seen that the simpler kinematical theory predicts many of the observed properties of weak-beam images. However, because of the approximations involved, it is generally preferable to use many-beam dynamical theory even in the case of large s. This theory is clearly more susceptible to error accumulation in the numerical integration procedure, but such effects can be checked by reducing the integration step-length until the results stabilize. Dynamical theory does not lend itself to simple pictorial representation such as the kinematical theory amplitude-phase diagram, and for the purpose of understanding computed images, a consideration of fig. 1.5(b) is often instructive. It is thus best to regard the two theories as complementary.

The analysis of section 1.5.2 for the case of only one strong reflection operating (the forward-scattered beam) gave the condition (1.77), $|w| \gg 5$, although a consideration of how close to the dislocation core an image is required often results in a more stringent condition on s (based on (1.81)). A convenient figure for dislocation work is $|s| \sim 2.10^{-2}$ Å^{-1} . The s value of a particular reflection is not immediately obvious from a diffraction pattern, so it is usual to operate near a pole and estimate s from the position of the Kikuchi bands. Simple geometry gives the result

$$s = \frac{(n-1)g^2}{2K} \qquad (1.82)$$

where the Ewald sphere cuts the row of systematics at ng (n not necessarily integer).

Having decided on a suitable reflection and value of s , the experimental procedure is as follows:- tilt the incident beam with the

electromagnetic deflection coils so that the required reflection g passes down the optical axis of the objective lens (by checking the current rotation centre); correct the astigmatism of the objective lens; tilt the specimen with the goniometer stage until the required s value is obtained when consulting the diffraction pattern; focus and expose plates. Generally it is safer to take a series of plates at different objective lens strengths since the exact focus is difficult to determine with the naked eye. The ultimate success of the weak-beam technique depends on the ability of the operator to focus the very faint image, and on the electrical and mechanical stability of the microscope. In the author's experience, on a JEM 100B with a top-entry goniometer stage and using Ilford EM4 plates, satisfactory weak-beam pictures can be obtained with exposure times of up to 30 seconds as a matter of routine, and up to one minute fairly frequently.

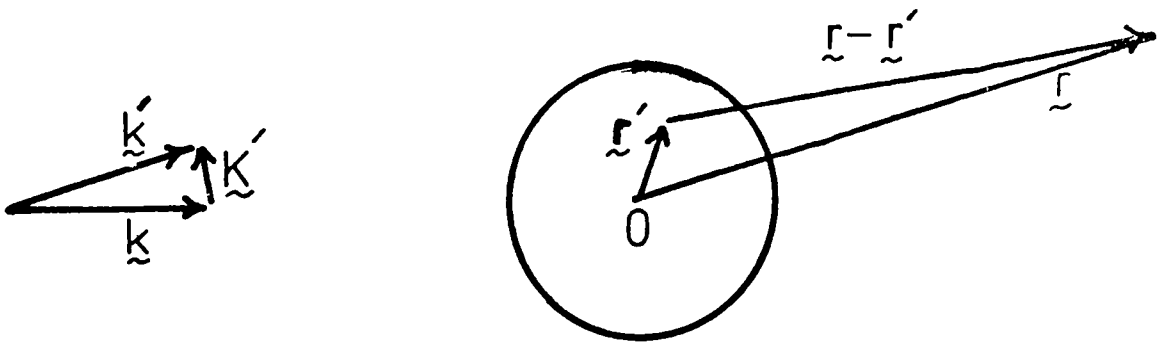

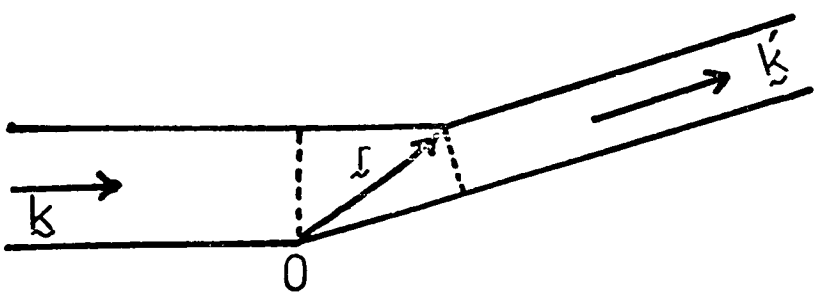

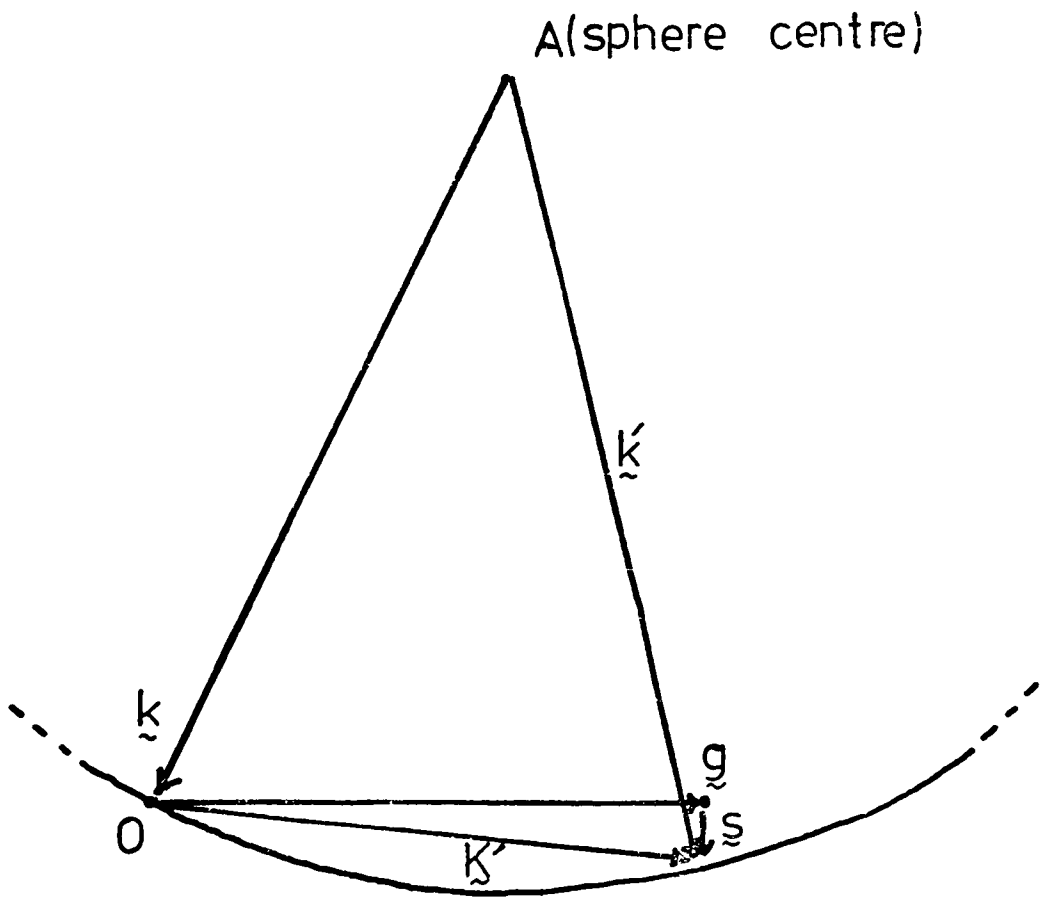

2g

Figure 1.1(a) The scattering of an electron wave $\underline{k}$ by a single atom.

Figure 1.1(b) Scattering by atoms at the origin and $\underline{r}$.

Figure 1.1(c) The reflecting sphere construction.

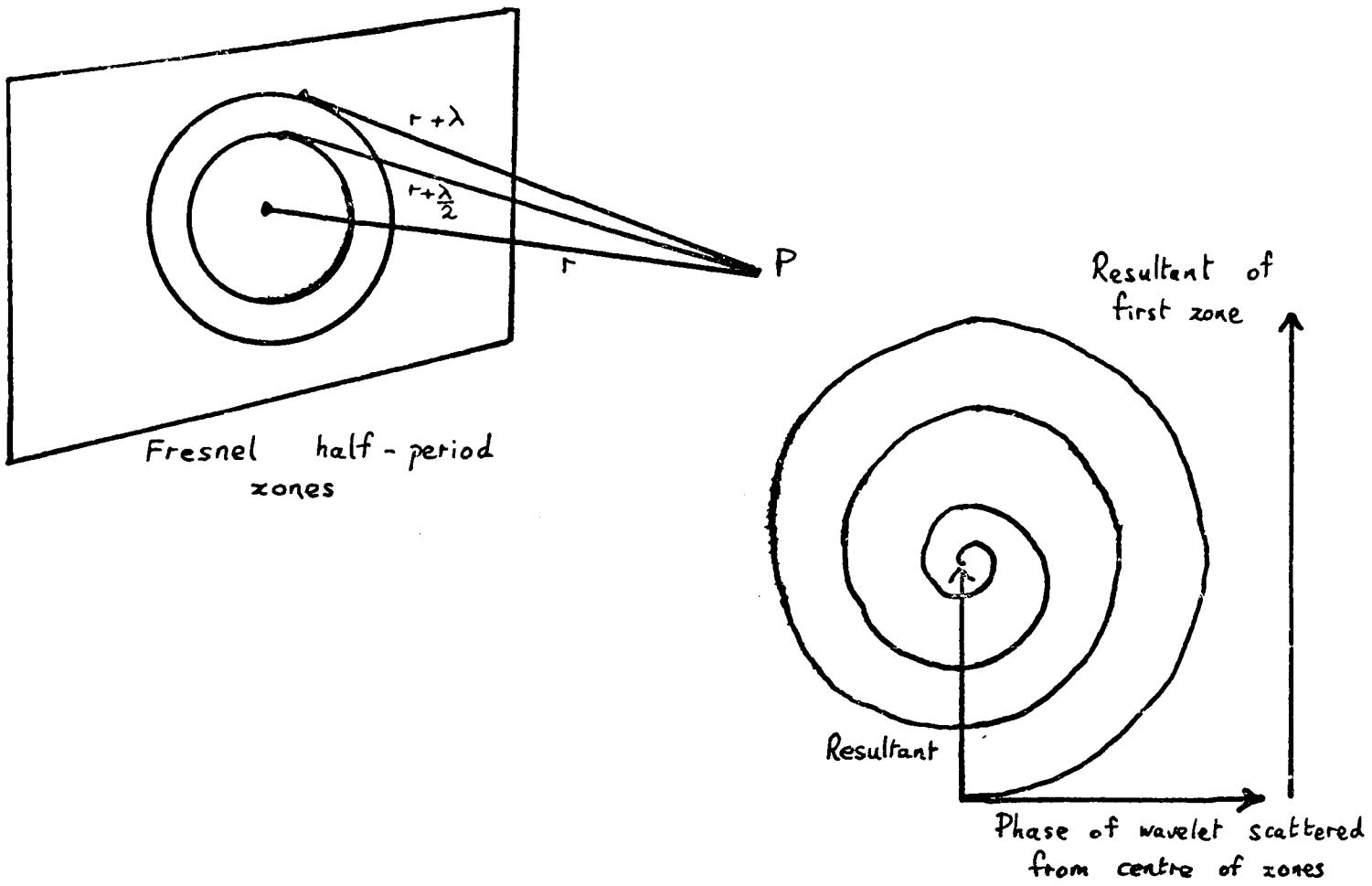
r + λ
r + λ/2
r
P
Fresnel half-period zones
Resultant of first zone
Resultant
Phase of wavelet scattered from centre of zones

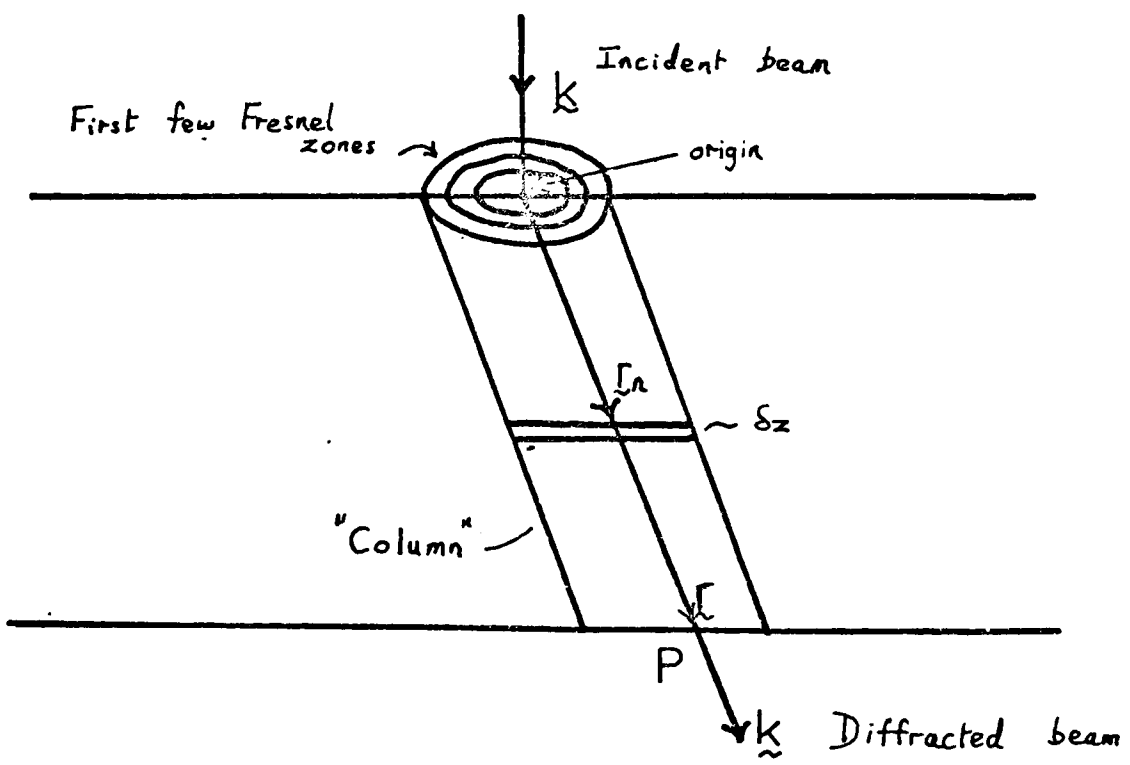
Incident beam
k
First few Fresnel zones
origin
r_n
~ δz
"Column"
r
P
k
Diffracted beam

Figure 1.2(a) Amplitude-phase diagram for the resultant at P due to scattering of plane wave.

Figure 1.2(b) Column of crystal for amplitude at P; see (1.18).

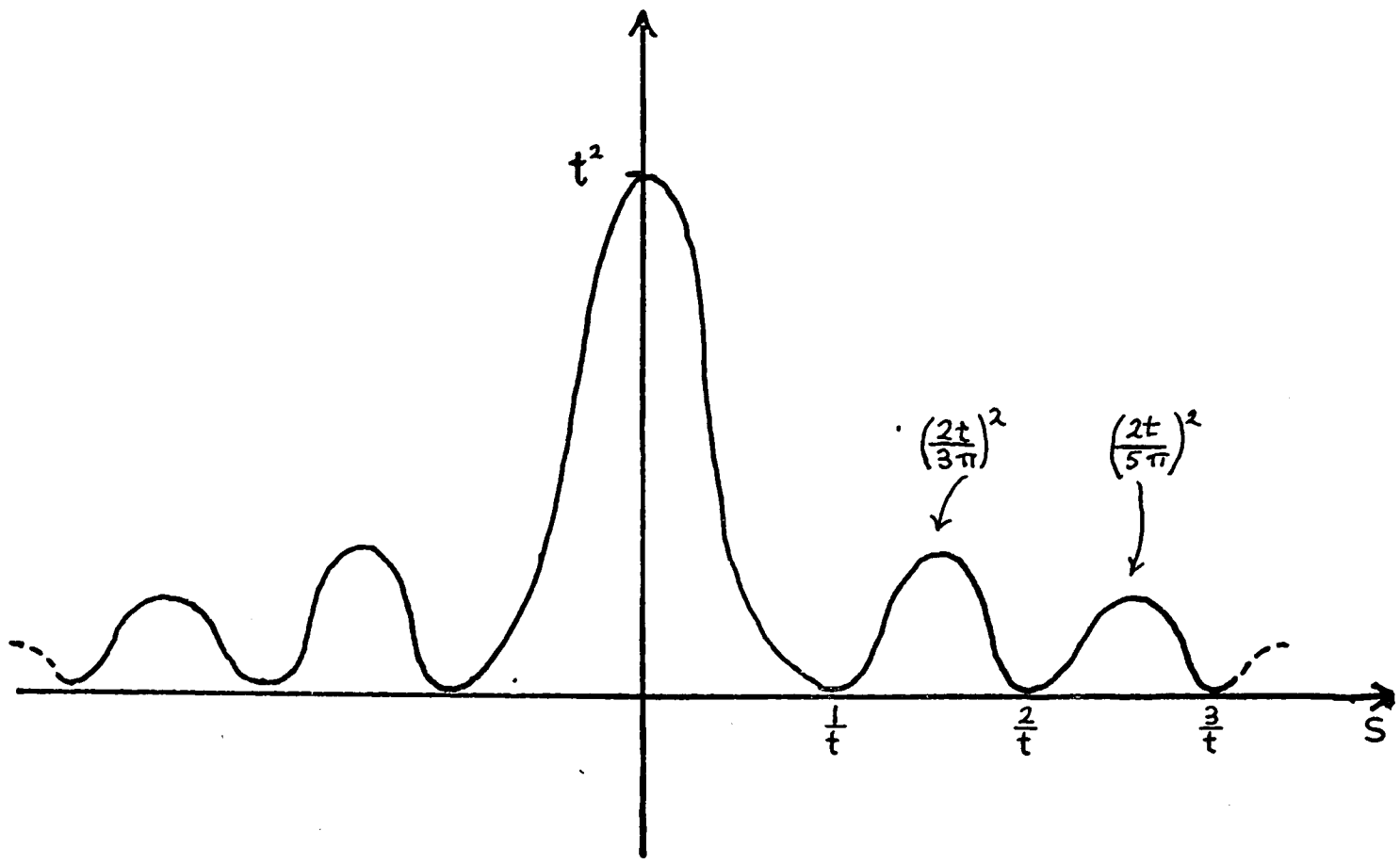
t^2
$\left(\frac{2t}{3\pi}\right)^2$
$\left(\frac{2t}{5\pi}\right)^2$
$\frac{1}{t}$
$\frac{2}{t}$
$\frac{3}{t}$
S

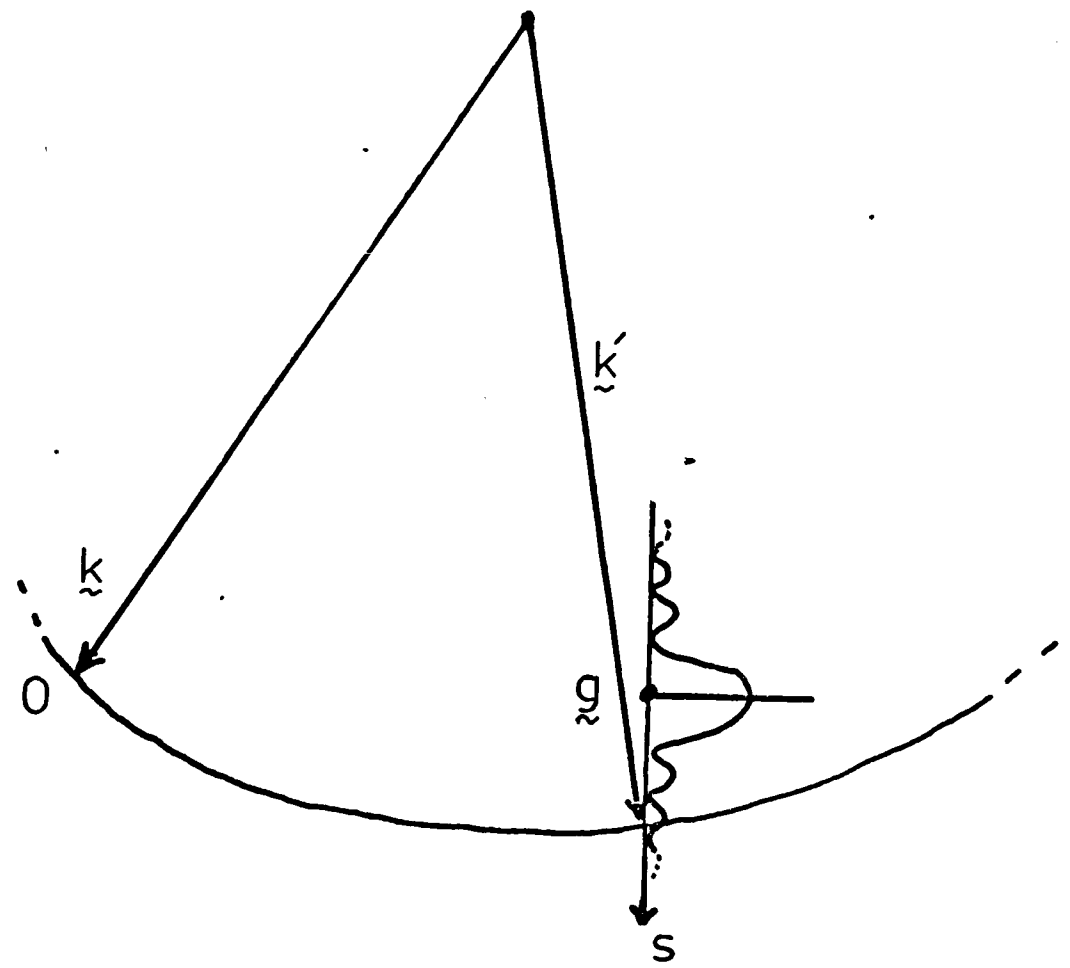
$\underset{\sim}{k}'$
$\underset{\sim}{k}$
0
$\underset{\sim}{g}$
S

Figure 1.3(a) The curve $\frac{\sin^2(\pi ts)}{(\pi s)^2}$ plotted against s (not to scale).

Figure 1.3(b) The curve of fig. 1.3(a) combined with the reflecting sphere construction.

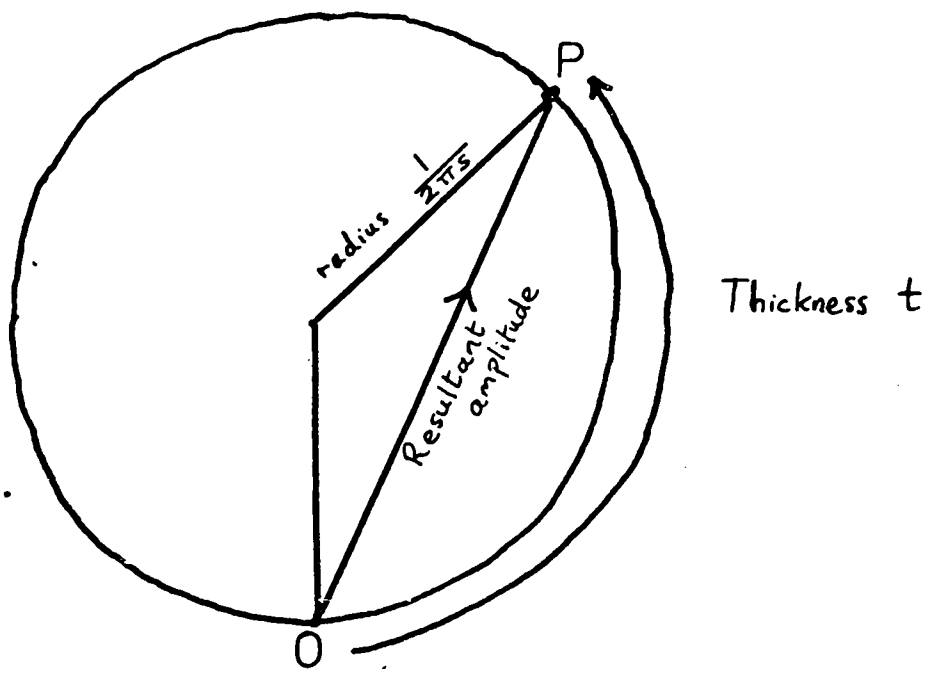

Thickness t

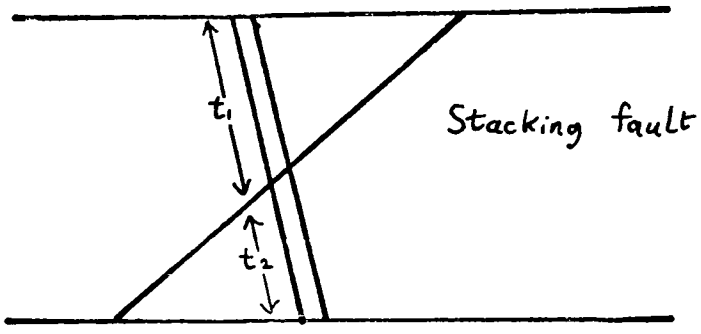

Stacking fault, $\alpha = 2\pi \underset{\sim}{g} . \underset{\sim}{R}$

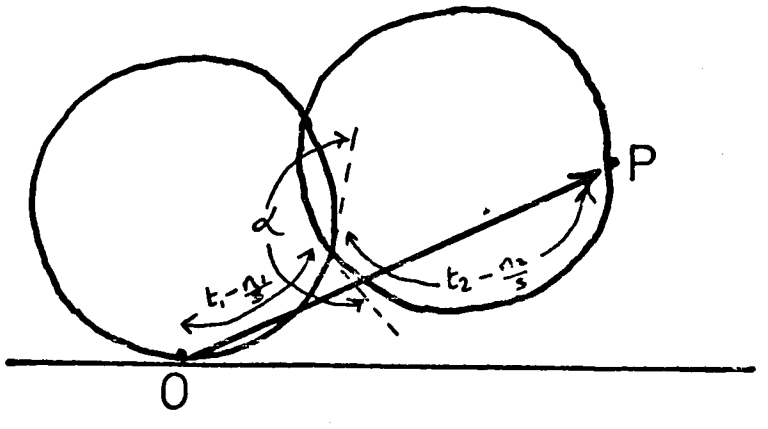

Figure 1.4(a) Amplitude-phase diagram for perfect crystal.

Figure 1.4(b) Amplitude-phase diagram for a stacking fault R at depth t_1 in crystal thickness $(t_1 + t_2)$.

(Based on Hirsch, Howie and Whelan 1960).

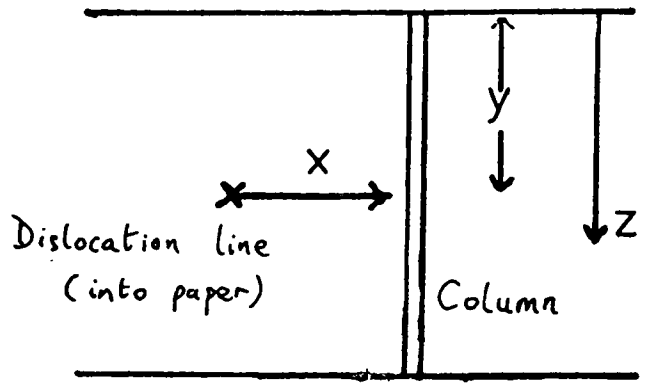
y
X
Z
Dislocation line
(into paper)
Column

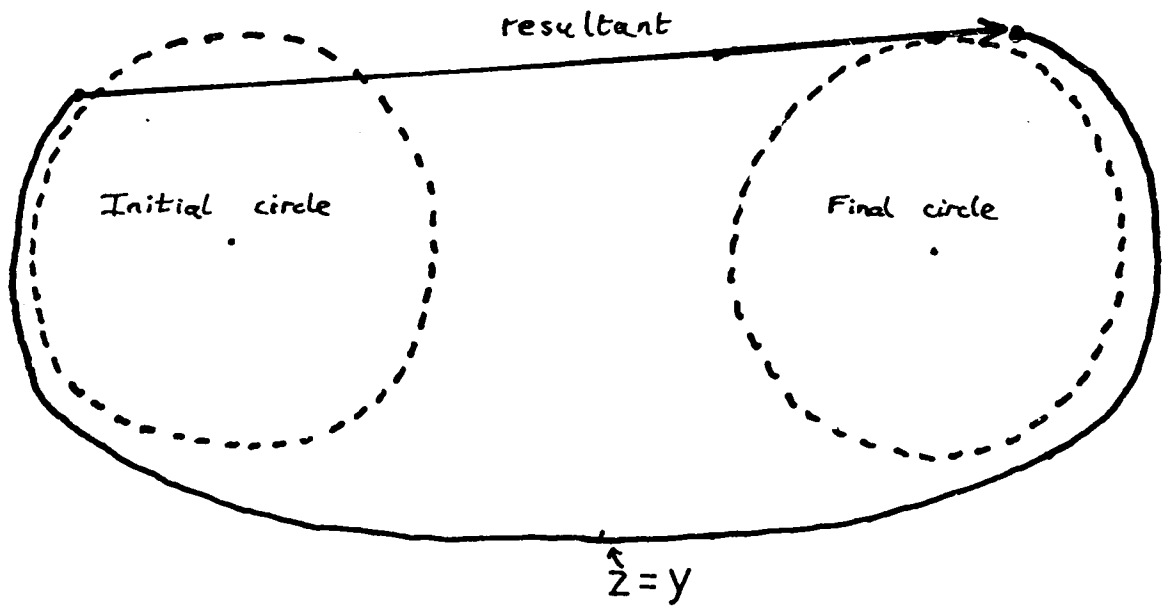
resultant
Initial circle
Final circle
z = y

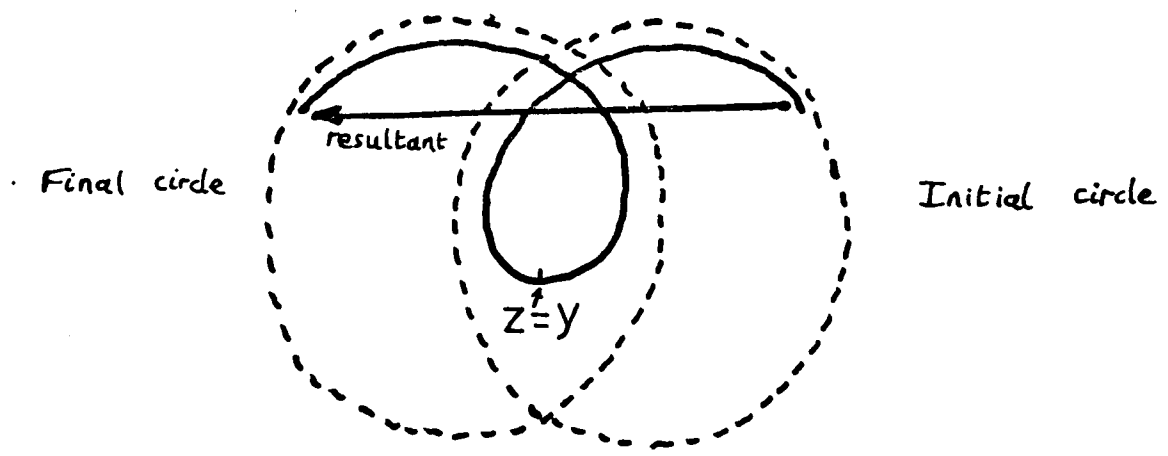
Final circle
resultant
Initial circle
z = y

Figure 1.5(a) Co-ordinates for equation (1.32)

Figure 1.5(b) Amplitude-phase diagram for screw dislocation, sx -ve, $\underline{g}.\underline{b}$ +ve.

Figure 1.5(c) Amplitude-phase diamgram for screw dislocation, sx +ve, $\underline{g}.\underline{b}$ +ve.

(Based on Hirsch, Howie and Whelan 1960).

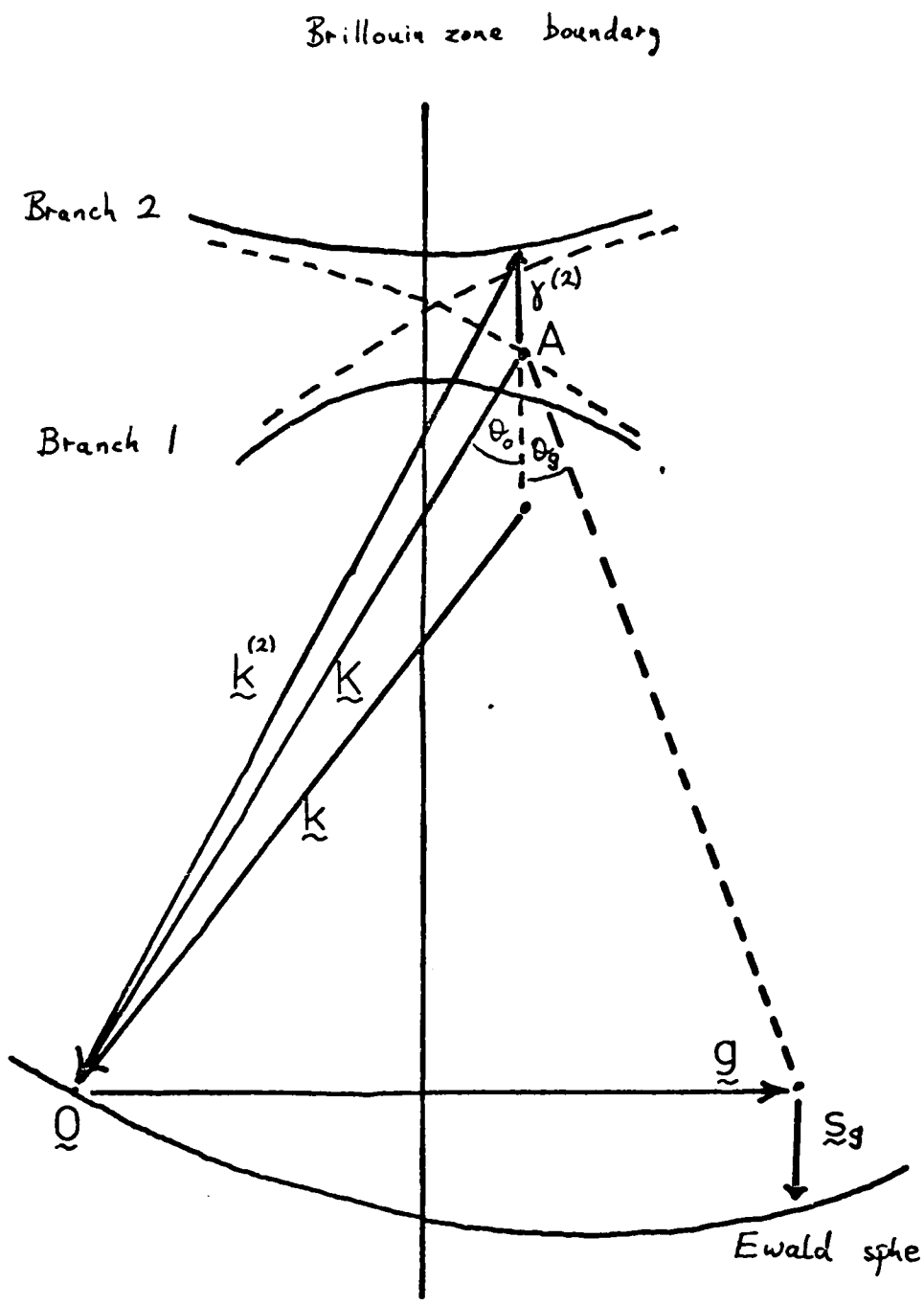

Ewald sphere, radius $|\underset{\sim}{K}|$, centre A.

Figure 1.6 The two-beam dispersion surface. The two branches corresponding to $j = 1,2$ (solid curves) are asymptopic to spheres of radius K centred on $\underline{O}$ and $\underline{g}$ (dotted curves). $\underline{s}^{(1)}$ and $\underline{k}^{(1)}$ are omitted for clarity.

Chapter 2

The application of elasticity theory to dislocations

2.1 Introduction

The mathematical theory of dislocations in an elastic medium predates the postulation of dislocations as defects in a crystalline solid. Thus Volterra (1907) discussed the properties of a cylindrical body which is cut and then deformed, and some of his defects correspond to dislocations; but the edge dislocation in a crystal lattice was first proposed by Orowan (1934), Polanyi (1934), and Taylor (1934). Other types of dislocation, and the concept now called the Burgers vector, were suggested by Burgers (1939). The Burgers vector is now usually defined by the FS/RH perfect crystal convention, given by Frank (1951), and its use is assumed throughout this thesis. The sense of the dislocation line is first defined. Then a closed circuit is made in good crystal round the line in a right-handed sense. When the circuit is repeated in perfect crystal, the vector required to close the circuit from finish to start is the Burgers vector, written $\underline{b}$. This procedure can be given a useful mathematical definition. In a body with orthogonal cartesian co-ordinates x_i $(i=1,2,3)$, a dislocation $\underline{b}$ with line direction x_3 can be created by cutting the material in the plane $x_2 = 0$, $x_1 > 0$ and displacing the two surfaces by $\underline{u}(x_1,x_2)$ such that

$$\underline{b} = \underline{u}(x_1,0^-) - \underline{u}(x_1,0^+) \qquad (2.1)$$

It should be noted that the choice of axes, and hence of the cut, is quite arbitrary; a dislocation is defined only by its line direction and $\underline{b}$. The stresses and strains are not affected by this choice, but the solution for the displacement $\underline{R}$ contains an arbitrary discontinuity. This point is considered further in section 2.6. This chapter is an outline of elasticity theory as applied to (2.1) , in both isotropic and anisotropic media. Further details of dislocation theory can be found in the many standard texts, e.g. Hirth and Lothe (1968).

2.2 The equations of linear elasticity

Let x_i $(i=1,2,3)$ be orthogonal cartesian axes. Define σ_{ij} as the

stress in the x_j direction on the plane with outward normal x_i .

Consideration of the forces on an elemental cube shows that

$$\sigma_{ij} = \sigma_{ji} \tag{2.2}$$

is the condition for rotational equilibrium if no internal torques exist.

If the body force per unit volume is zero, the condition for equilibrium in the x_i direction is

$$\frac{\delta\sigma_{1i}}{\delta x_1} + \frac{\delta\sigma_{2i}}{\delta x_2} + \frac{\delta\sigma_{3i}}{\delta x_3} = 0$$

$$\frac{\delta\sigma_{ij}}{\delta x_j} = 0 \qquad \text{using (2.2)} . \tag{2.3}$$

The components of strain are defined in terms of the displacements u_i by

$$\epsilon_{kl} = \tfrac{1}{2}\left(\frac{\delta u_k}{\delta x_l} + \frac{\delta u_l}{\delta x_k}\right) \tag{2.4}$$

For small deformations the stresses are given by

$$\sigma_{ij} = C_{ijkl}\epsilon_{kl} \tag{2.5}$$

where C_{ijkl} are the 81 elastic constants. Equations (2.2), (2.4) and (2.5) give

$$C_{ijkl} = C_{jikl} = C_{ijlk} \tag{2.6}$$

which reduces the number of independent constants to 36. This is often expressed by writing C_{ijkl} as C_{MN} by the following rule:-

ij or kl	11	22	33	23	31	12
M or N	1	2	3	4	5	6

(2.7)

Equations (2.3), (2.4), (2.5) and (2.6) combine to give

$$C_{ijkl}\frac{\delta^2 u_k}{\delta x_j \delta x_l} = 0 \tag{2.8}$$

Consideration of the strain energy when a volume element is deformed reversibly gives

$$C_{MN} = C_{NM} \tag{2.9}$$

reducing the number of constants to 21. Finally, a cubic crystal is invariant in symmetry to 90° rotation about the cube axes, so

$$C_{11} = C_{22} = C_{33} \;;\; C_{12} = C_{13} \;;\; C_{44} = C_{55} = C_{66} \;;\; \text{all other constants zero} \tag{2.10}$$

There are then only 3 independent constants for a cubic crystal. The ratio

$$A = \frac{2C_{44}}{C_{11}-C_{12}} \tag{2.11}$$

is called the anisotropy factor. For isotropic materials $A = 1$, reducing the number of constants to 2 . The elastic constants C_{11} , C_{12} , C_{44} found in tables are for the crystal cube axes co-ordinate system, x_i . In practice another axes set x_i' may be more useful. Then the stresses and strains σ_{ij}' , ϵ_{kl}' are given by the same equations if the elastic constants are written

$$C_{ijkl}' = T_{ig}\, T_{jh}\, C_{ghmn}\, T_{km}\, T_{ln} \tag{2.12}$$

where T_{ij} is the direction cosine between the x_i' and the x_j axes. The isotropic condition $A = 1$ gives $C_{ijkl}' = C_{ijkl}$ for all choices of x_i' .

2.3 The displacement field of an infinite straight dislocation: isotropic solution

2.3.1 The screw dislocation

The dislocation is formed as described in section 2.1. The Burgers vector $\underline{b}_s$ has only one component, b_s , in the x_3 direction. Assuming that $u_1 = u_2 = 0$, and $u_3 = u_3(x_1,x_2)$ reduces (2.1) to

$$b_s = u_3(x_1,0^-) - u_3(x_1,0^+) \tag{2.13}$$

which suggests the solution

$$u_3 = \frac{b_s}{2\pi} \tan^{-1}\left(\frac{x_2}{x_1}\right) \tag{2.14}$$

Substitution in (2.8) verifies that (2.14) is a satisfactory solution. The stresses follow from (2.4) and (2.5).

2.3.2 The edge dislocation

The edge dislocation is an example of plane strain, defined by

$$u_1 = u_1(x_1,x_2) \;\; ; \;\; u_2 = u_2(x_1,x_2) \;\; ; \;\; u_3 = 0 \;\; ; \;\; \frac{\partial}{\partial x_3} = 0 \tag{2.15}$$

In this case the solution is not obvious, so we solve for stress first. Equation (2.3) is automatically satisfied if the stresses are derived from the Airy stress function χ defined by

$$\sigma_{11} = \frac{\partial^2 \chi}{\partial x_2^2} \quad ; \quad \sigma_{22} = \frac{\partial^2 \chi}{\partial x_1^2} \quad ; \quad \sigma_{12} = \frac{-\partial^2 \chi}{\partial x_1 \partial x_2} \tag{2.16}$$

Differentiation of (2.4) in the condition (2.15) produces the compatibility equation

$$\frac{\partial^2 \epsilon_{11}}{\partial x_2^2} + \frac{\partial^2 \epsilon_{22}}{\partial x_1^2} = \frac{2\partial^2 \epsilon_{12}}{\partial x_1 \partial x_2} \tag{2.17}$$

Combining (2.17) with (2.5) and (2.16) gives

$$\left(\frac{\partial^2}{\partial x_1^2} + \frac{\partial^2}{\partial x_2^2}\right)^2 \chi = \nabla^4 \chi = 0 \tag{2.18}$$

The dislocation line direction $\underline{l}$ is along x_3. As mentioned in section 2.1, the choice of axes x_1, x_2 is arbitrary, but the solution of (2.18) is simplified if $\underline{b}_e$ has only an x_1 component, b_e. Then the particular solution of (2.18) (neglecting boundary condition terms) is

$$\chi = \frac{-\mu b_e x_2}{2\pi(1-\nu)} \ln r \tag{2.19}$$

where $r = (x_1^2 + x_2^2)^{\frac{1}{2}}$. Substituting in (2.16) gives the stresses, hence from (2.5) the strains, and by integrating, the displacements. The result is

$$\underline{R}_e = \frac{\underline{b}_e}{2\pi}\left[\theta + \frac{\sin 2\theta}{4(1-\nu)}\right] + \frac{\underline{b}_e \wedge \underline{l}}{2\pi}\left(\frac{(1-2\nu)}{4(1-\nu)} \ln r + \frac{\cos 2\theta}{4(1-\nu)}\right) \tag{2.20}$$

where $\theta = \tan^{-1}\left(\frac{x_2}{x_1}\right)$.

2.3.3 The general dislocation

This is given by superimposing (2.14) and (2.20). The total Burgers vector $\underline{b} = \underline{b}_e + \underline{b}_s$, and $\underline{b}_e \wedge \underline{l} = \underline{b} \wedge \underline{l}$. Hence

$$\underline{R} = \frac{1}{2\pi}\left[\underline{b}\theta + \underline{b}_e \frac{\sin 2\theta}{4(1-\nu)} + \underline{b} \wedge \underline{l}\left(\frac{(1-2\nu)}{4(1-\nu)} \ln r + \frac{\cos 2\theta}{4(1-\nu)}\right)\right] \tag{2.21}$$

Stresses again follow directly from (2.4) and (2.5).

2.4 The displacement field of an infinite straight dislocation: anisotropic solution

The solution in an anisotropic medium was first derived by Eshelby, Read and Shockley (1953). Stroh (1958) presented the solution in a form more amenable to handling by computer, and the following account is

mainly based on his work. Computer sub-routines using this method have been published by Head et al. (1973).

Let the dislocation line lie along x_3 and assume that $\frac{\partial}{\partial x_3} = 0$.

Then the displacement can be expressed as

$$u_k = A_k \, f(x_1 + p x_2) \tag{2.22}$$

Substituting (2.22) in (2.8) gives 3 equations of 12 terms,

$$(C_{i1k1} + pC_{i1k2} + pC_{i2k1} + p^2 C_{i2k2}) A_k = 0 \tag{2.23}$$

or

$$\underline{S} \; \underline{A} = 0$$

This only has a solution if the determinant

$$[S] = 0 \tag{2.24}$$

Equation (2.24) is a sextic equation in p , with roots in complex conjugate pairs; denote the roots with positive imaginary parts by p_α , $\alpha = 1,2,3$. The corresponding vector A_k may be written $A_{k\alpha}$ and found (except for an arbitrary factor) from (2.23). Throughout this section summation over repeated Latin indices is implied, but summation over α is shown explicitly.

Equation (2.22) now takes the form

$$\begin{aligned} u_k &= \sum_\alpha A_{k\alpha} \, f_\alpha(z_\alpha) + \sum_\alpha A_{k\alpha}^* \, (f_\alpha(z_\alpha))^* \\ &= 2 \, \mathrm{Re} \sum_\alpha A_{k\alpha} \, f_\alpha(z_\alpha) \end{aligned} \tag{2.25}$$

where $z_\alpha = x_1 + p_\alpha x_2$.

Now several new quantities are defined. Firstly,

$$\begin{aligned} L_{i\alpha} &= (C_{i2k1} + p_\alpha C_{i2k2}) \, A_{k\alpha} \\ &= -(C_{i1k2} + \frac{C_{i1k1}}{p_\alpha}) \, A_{k\alpha} \end{aligned} \tag{2.26}$$

and we note that

$$A_{i\beta}^* \, L_{i\alpha} = -A_{i\alpha} \, L_{i\beta}^* \tag{2.27}$$

Next, the vectors reciprocal to $L_{i\alpha}$:

$$M_{\alpha i} \, L_{i\beta} = \delta_{\alpha\beta} \tag{2.28}$$

and (2.27) becomes

$$\sum_\alpha A_{i\alpha} \, M_{\alpha j} + \sum_\alpha A_{j\alpha}^* \, M_{\alpha i}^* = 0 \tag{2.29}$$

Finally, the real matrix

$$B_{ij} = - \, \mathrm{Im} \sum_\alpha A_{i\alpha} \, M_{\alpha j} \tag{2.30}$$

which does not contain the arbitrary factor in both $A_{i\alpha}$ and $M_{\alpha j}$, and its real reciprocal H_{ij} given by

$$B_{ki} H_{ij} = \delta_{kj} \tag{2.31}$$

A stress function ϕ defined by

$$\sigma_{i1} = -\frac{\partial \phi_i}{\partial x_2} \quad ; \quad \sigma_{i2} = \frac{\partial \phi_i}{\partial x_1} \tag{2.32}$$

has the property that the increment $\Delta\phi_i$ in going round a closed curve C is equal to the resultant force F_i acting across C . Equations (2.5), (2.25) and (2.32) give

$$\phi_i = 2\mathrm{Re} \sum_\alpha L_{i\alpha} f_\alpha(z_\alpha) \tag{2.33}$$

Now we define the real vector d_i in terms of the Burgers vector

$$d_i = H_{ij} b_j \tag{2.34}$$

and assume that the unknown function $f_\alpha(z_\alpha)$ can be written as

$$f_\alpha(z_\alpha) = \frac{M_{\alpha i} d_i \ln(z_\alpha)}{4\pi} \tag{2.35}$$

again neglecting boundary condition terms. Then (2.25) becomes

$$u_k = \frac{1}{2\pi} \mathrm{Re} \sum_\alpha A_{k\alpha} M_{\alpha i} H_{ij} b_j \ln(z_\alpha) \tag{2.36}$$

and (2.33) is

$$\phi_i = \frac{1}{2\pi} \mathrm{Re} \sum_\alpha L_{i\alpha} M_{\alpha k} H_{kj} b_j \ln(z_\alpha) \tag{2.37}$$

Applying (2.1) as a check to (2.36) gives

$u_k(x_1,0^-) - u_k(x_1,0^+) = \frac{1}{2\pi} \mathrm{Re} \sum_\alpha A_{k\alpha} M_{\alpha i} H_{ij} b_j 2\pi i = b_k$ as required, and we note from (2.37) that round a closed curve $\Delta\phi_i$ is zero and hence F_i is zero. Therefore (2.35) satisfies the conditions for (2.36) to be the displacement field of a dislocation.

2.5 The force on a dislocation

The force on a dislocation may be derived by considering the movement of a dislocation, line direction l_j and Burgers vector b_h , a distance δr_k in an external stress field σ_{ih} . The area swept out by the dislocation, and the components of the normal to this plane, are given by

$$a_i = \epsilon_{ijk} l_j \delta r_k \quad \text{per unit length} \tag{2.39}$$

where ϵ_{ijk} is the permutation operator. The movement is made by cutting

the material over an area a_i , and displacing the two surfaces by b_h .

The force on the plane a_i is given by

$$f_h = a_i \sigma_{ih} = \varepsilon_{ijk} l_j \delta r_k \sigma_{ih} \tag{2.39}$$

and the work done is

$$f_h b_h = \varepsilon_{ijk} l_j \delta r_k \sigma_{ih} b_h \quad \text{per unit length.} \tag{2.40}$$

If the force per unit length acting on the dislocation due to the stress field σ_{ih} is F_k , then the work done is also $F_k \delta r_k$ per unit length. Equating this and (2.40) gives the required result

$$F_k = \varepsilon_{ijk} l_j \sigma_{ih} b_h \tag{2.41}$$

This formula was first derived by Peach and Koehler (1950). It can be used to calculate the force exerted by one dislocation on another by taking σ_{ih} as the stress field of a dislocation, obtainable from (2.32) and (2.37).

2.6 The application of the dislocation displacement function to image computations

The use of, for example, (2.36) directly in equations (1.36) requires a little care. It has already been pointed out in section 2.1 that the application of (2.1) automatically introduces a displacement discontinuity across the $x_2 = 0$ plane which is in fact arbitrary, depending only on the initial choice of axes. If any column were to cross this plane the effect would be to introduce a non-existent stacking fault. This can be dealt with by setting the x_1 axis to coincide with the axis of integration z . Then there is only a discontinuity between adjacent columns and this has no effect on the calculated image. Once the axes x_i have been chosen, the only quantities dependent on a particular dislocation in (2.36) are b_j and z_α ; the other terms are the same for any dislocation with this choice of axes. Thus the displacements due to a set of parallel dislocations can be set up easily, and in this respect (2.36) is more flexible than (2.21).

A common configuration for calculation involves a set of partial dislocations separated by ribbons of stacking fault. The displacements due to the dislocations follow the same equations as those for perfect dislocations. The stacking faults are included by introducing the relevant

fault vector $\underline{R}$ whenever a column crosses the plane joining the partial dislocations in question. A useful rule here is that the vector $\underline{R}$ to be introduced when crossing a fault plane is the sum of the Burgers vectors of all the dislocations crossed by following the faults to the right until perfect crystal is reached, when looking from above and along the dislocation lines.

Part II

Chapter 3

A study of faulted dipoles in copper using weak-beam electron microscopy

3.1 Introduction

Mader (1963) first reported the existence of faint, straight lines along <110> directions in strong-beam electron micrographs of deformed face-centred cubic metals. It was suggested by Hirsch (1963) that these were images of dipoles consisting of two Frank partial dislocations which bounded a ribbon of stacking fault on a {111} plane whose normal was inclined to the primary glide plane. The geometry was discussed in greater detail by Seeger (1964) who proposed that the Frank dislocations were dissociated on the primary glide plane. Such faulted dipoles could be formed either by the transformation of an ordinary dipole or by the glide of a dislocation containing a dissociated sessile superjog. The equilibrium configurations of faulted dipoles have been computed by Seeger and Wobser (1966) and Steeds (1967a). These caculations have been used in conjunction with experimental micrographs and computed strong-beam images to determine the stacking-fault energy of several face-centred cubic pure metals and alloys (Häussermann and Wilkens 1966; Steeds 1967b). The results reported by Steeds are somewhat higher than those of Häussermann and Wilkens, especially in the case of pure copper (150 erg cm^{-2} as opposed to 59 erg cm^{-2}).

It has been shown by Cockayne (1970, 1972), as discussed in Chapter 1, that the fundamental condition for obtaining weak-beam images from a reflection g is that the deviation parameter $|w| = |s_g \xi_g| > 5$, and that the width and position of a peak from a dislocation then depends on the value of s_g (s_g is the distance from the reciprocal lattice point g to the Ewald sphere and ξ_g is the extinction distance for the reflection g). If no reflection is strongly excited, and $|s_g| > 2.10^{-2}$ Å^{-1}, the image peak has a half-width of $\sim$ 15 Å and lies close to (within 20 Å of) the defect core (Cockayne 1973). Such images are thus very suitable for investigating the geometry of the closely-spaced dislocations found in faulted dipoles. This chapter describes the application of the theories outlined in Part I to the analysis of experimental micrographs of faulted

dipoles in copper. The electron microscopy and measurement of recorded images was expertly performed by Mr. C.B. Carter.

3.2 The geometry of faulted dipoles

3.2.1 The application of elasticity theory to faulted dipoles

Faulted dipoles consist of four parallel partial dislocations, two Shockleys and two stair-rods, and may occur theoretically in two basic configurations which have been called Z and S by Seeger (1964). These are portrayed in fig. 3.1 for a (111) foil together with a consistent set of Burgers vectors (the dislocations are also numbered for convenience). When in the (111) orientation, the height of the dipole is written as H, and the horizontal separation of the Shockley dislocations as Δ; when the foil is tilted so that the electron beam is along the $[\bar{1}\bar{1}\bar{2}]$ direction, the new horizontal separation is distinguished by a dashed superscript, Δ', and the vertical stair-rod to stair-rod distance is written as H' (these should not be confused with the H and Δ used by Steeds). The partial dislocations enclose three ribbons of stacking fault. These are either all intrinsic or all extrinsic in the case of a Z dipole, but for an S dipole the inner ribbon, bounded by the stair-rods, is of opposite character to the other two. In fig. 3.1 the Burgers vectors have been chosen such that the faults are all intrinsic for the Z, and intrinsic-extrinsic-intrinsic for the S. (It has been assumed that the stair-rods are those with the lowest energy, i.e. that the Burgers vectors are of the type $\frac{a}{6}\langle 110\rangle$. The next highest energy stair-rods have Burgers vectors of the type $\frac{a}{6}\langle 00\bar{2}\rangle$ and the three stacking-faults of an S dipole containing such dislocations are identical. The isotropic elasticity calculations of Steeds (1967a) showed that the likelihood of this occurring can safely be ignored).

Equilibrium configurations of faulted dipoles may be calculated using the anisotropic elasticity relations for infinite straight dislocations given by Stroh (1958) and outlined in Chapter 2. The application of these

expressions to dissociated dipoles has been discussed by Morton and Forwood (1973), though the present case is simpler since for a given value of H the positions of the stair-rods are fixed, and the Shockleys are symmetrically displaced about the centre of the dipole, their separation Δ depending on the value of the stacking-fault energy γ. Using the co-ordinate system defined in fig. 3.1, the net force per unit length on dislocation 4 in the x_1 direction, using the Peach-Koehler formula (2.41), is

$$F_1 = \sum_{n=1}^{3} b(4)\, \sigma_{12}(n) \quad - \quad \gamma \tag{3.1}$$

where $\sigma_{12}(n)$ is a component of the stress field due to dislocation n and b(4) is the x_1 (in fact the only) component of the Burgers vector of dislocation 4. The stress $\sigma_{12}(n)$ at the point z (n) is obtainable from (2.32) and (2.37) as

$$\sigma_{12}(n) = \frac{1}{2\pi}\ \mathrm{Re}\sum_{\alpha} \frac{L_{1\alpha}\, M_{\alpha k}\, H_{kj}\, b_j(n)}{z_\alpha(n)} \tag{3.2}$$

where $z_\alpha(n) = x_1(n) + p_\alpha x_2(n)$, and $x_1(n)$, $x_2(n)$ are the co-ordinates of the point in question when the x_3 axis coincides with the line of dislocation n. Then (3.1) becomes

$$F_1 = \frac{1}{2\pi}\ \mathrm{Re}\sum_{n=1}^{3}\sum_{\alpha} \frac{b(4)\, L_{1\alpha}\, M_{\alpha k}\, H_{kj}\, b_j(n)}{z_\alpha(n)} \quad - \quad \gamma. \tag{3.3}$$

where $z_\alpha(n)$ now involves the co-ordinates of dislocation 4 with respect to dislocation n. The quantities p_α, $L_{1\alpha}$, $M_{\alpha k}$ and H_{kj} depend only on the elastic constants of the material and the choice of co-ordinate axes. They may be evaluated from computer sub-routines given by Head et al. (1973). The required solution for Δ at a particular H and γ occurs when F_1 is zero. This may easily be found by moving dislocations 1 and 4 by fixed increments and evaluating F_1 each time, reversing the direction of motion and reducing the increment whenever F_1 changes sign. The curves of Δ against H for various values of γ are plotted for Z dipoles in fig. 3.2 and for S dipoles in fig. 3.3 using the elastic constants of pure copper given by Huntington (1958).

3.2.2 Energy considerations and the critical height

Not all the points on the curves of figs. 3.2 and 3.3 correspond to physically possible faulted diples. Above a certain height the unfaulted form of four Shockley partial dislocations will have a lower energy. The exact value of this height depends on whether the pure edge (E) or the mixed character (M) Shockleys are taken as nearest each other in the unfaulted form since there are two equilibrium configurations of the dissociated dipole. Both the calculations of Seeger and Wobser (1966) and Steeds (1967a) for pure copper show that the E-Z and M-S transitions give the maximum values of this critical height in Z and S dipoles at a particular Δ or γ ; the curves of Steeds are plotted in figs. 3.2 and 3.3. Steeds further demonstrated that the curves for S dipoles depend strongly on the ratio of γextrinsic/γintrinsic , here taken as unity (for $\gamma_E > \gamma_I$, the critical height at a particular γ_I decreases); and that the curves are relatively independent of changes in the core cut-off radii. The Z dipole transition curves as calculated by both Seeger and Wobser and Steeds are plotted in fig. 3.4. It can be seen that there is some disagreement between the two sets of results although both predict that $H_{E-Z} > H_{M-Z}$. This disagreement has been explained by Steeds in terms of the cutting procedure used in forming the dipoles when calculating the energy.

An S faulted dipole may have values of Δ and H such that it lies between the transition curves in fig. 3.3. The E configuration then has a lower energy and it is favourable for the dipole to unfault. However, were this to occur, the dissocated dipole would initially be closer to the equilibrium M configuration which still has a higher energy than the faulted dipole. We therefore expect the M-S curve to represent the S faulted dipoles with the largest H. In the case of Z dipoles no such argument applies. Faulted dipoles lying between the transition curves will probably unfault to the M form. Therefore we expect the M-Z curve to

represent the Z faulted dipoles with the largest H.

The curves of figs. 3.2, 3.3 and 3.4 can be used to estimate γ in several ways. Values of H derived from experimental images may be compared with the M-Z or M-S transition curves to give an upper limit on the stacking-fault energy. This approach was employed by Häussermann and Wilkens (1966) and Steeds (1967b). The difference between the M-Z curves used in the two cases, as shown in fig. 3.4, is one reason for the lack of agreement in their results for copper. (Their work is discussed further in section 3.6). An alternative method is to estimate Δ from experimental images. Then an upper limit can be set on γ directly from the equilibrium curves in the case of Z dipoles, and from the M-S transition curve in the case of S dipoles. Such measurements have been made from weak-beam images, and their interpretation is described in sections 3.3 and 3.5. The ideal approach would be to determine H and Δ of the same dipole. In the case of both S and Z dipoles the value of γ would then be unambiguously defined from the equilibrium curves. It should be possible to apply this method by using the weak-beam technique and tilting the specimen through a large angle, but this has not yet been attempted.

3.3 The weak-beam image contrast calculations

3.3.1 Weak-beam images at the (111) pole

Image profiles of faulted dipoles in copper were computed using the many-beam dynamical equations with the column approximation (Howie and Whelan 1961), equations (1.36), and an anisotropic strain field of the form (2.36) with the elastic constants of pure copper given by Huntington (1958). The atomic scattering factor was calculated using the analytic representation of Smith and Burge (1962), and absorption effects were included by using a straight-line approximation to the data given by Humphreys and Hirsch (1968). The upward foil normal was taken as [111] and the dislocation Burgers vectors were as given in fig. 3.1. Calculations were performed for the electron beam incident along $[\bar{1}\bar{1}\bar{1}]$ and $[\bar{1}\bar{1}2]$ directions (see fig. 3.1); hereafter

referred to as (111) and (112) poles respectively.

Of the six {220} reflections at the (111) pole, two of these, $\pm (2\bar{2}0)$, are parallel to the dipole line direction. Since all the dislocations are pure edge in character, and they have a $[\bar{1}10]$ line direction, there is no displacement in this direction and so $\underline{g}.\underline{R} = 0$ for all the partials. No contrast is expected in these reflections. The other two pairs, $\pm (20\bar{2})$ and $\pm(02\bar{2})$, have identical $\underline{g}.\underline{R}$ products and so images were calculated in the plus and minus $\underline{g}$ pair $20\bar{2}$ and $\bar{2}02$. The deviation parameter s_g was $2.38.10^{-2}$ Å^{-1} , satisfying the requirements that $|s_g| > 2.10^{-2}$ Å^{-1} and that no reflection should be strongly excited, as discussed by Cockayne (1972) and in Chapter 1. Five-beam image profiles were computed for a range of foil thickness from 2.0 to $2.2\xi_g$ (ξ_g = 418 Å). This is a span of two effective extinstion distances for the value of s_g chosen and so should display any relevant thickness dependence effects. The general features of the contrast may be seen in fig. 3.5, which is an intensity profile in $\pm \underline{g}$ from a Z dipole. The positions of the outer Shockley partials, dislocations 1 and 4, are marked on the x_1 axis. The profiles are in the form of two peaks, assocated with the Shockley dislocations, which display inside-outside contrast behaviour. There is no contrast from the outer stacking faults in these reflections, but the inclined fault can give rise to stacking-fault fringes. It is not in general possible to distinguish these from the faint contrast due to the stair-rods. In the inside contrast case (the $(\bar{2}02)$-type reflection) such contrast is superimposed on that due to the Shockley partials, giving rise to two broad intense peaks. Separate contrast from the central section is only visible in dipoles of large height. No useful information can be deduced from the relative intensity of the two peaks in fig. 3.5 since this effect depends on the defect depth and the foil thickness. In the outside contrast case (the $(20\bar{2})$-type reflection) the peaks from the Shockley partials are weaker, and again the relative intensity is dependent on depth and thickness.

For dipoles of small height the central stacking-fault and stair-rod contrast is generally weaker than the outer peaks and is often invisible. As the height increases this central contrast can occasionally become stronger than the outer peaks at certain defect depths and foil thicknesses, and for dipoles of large height several fringes can occur. However, the outer peaks from the Shockley partials are always distinguishable from such effects. All these features are also displayed by S dipoles, except that the two main peaks in either reflection can have a larger difference in intensity than in the Z dipole case. It is unlikely that this feature could be reliably used in practice to distinguish between the two configurations. Images recorded in the $(20\bar{2})$-type reflection (outside contrast) are more useful in practice because of the greater ease and accuracy in measuring wider peak separations.

The object of the image computations is to derive a relation between the observed peak separation, Δ_{obs}, and Δ, by systematically varying the size and shape of the defect, its depth in the foil and the foil thickness. The results of this process for Z dipoles are illustrated in figs. 3.6, 3.7 and 3.8 where the displacements of the two peaks from the positions of dislocations 1 and 4 are plotted against foil thickness. Fig. 3.6 shows the results for a faulted dipole with $\Delta_z = 47$Å, $H_z = 19$Å, positioned at five depths in the range $d = 1.0 \rightarrow 1.1\ \xi_g$ (the depth is defined as that of the centre of the dipole). The peak positions vary with thickness with a periodicity of the effective extinction distance, $\sim 0.1\ \xi_g$. It can be seen that this is also the period of the depth oscillations. Fig. 3.7 investigates the effect of varying H_z. The six curves are for faulted dipoles at a depth of $d = 1.0\ \xi_g$, with $\Delta_z = 33.5$ Å and a range of $H_z = 9.5 \rightarrow 56.5$ Å. The spread in peak positions is greater here and appears to vary with H_z with a periodicity of twice the effective extinction distance. This is because the variations are essentially due to the depth of the Shockley partials in the foil, and the wider spread

reflects the fact that changing H_z at a fixed Δ_z has a more complicated effect on the image than simply changing the depth of a dipole of fixed dimensions. Fig. 3.8 is for four faulted dipoles at depth d = 1.0 ξ_g with different values of Δ_z in the range 33 $\rightarrow$ 60 Å and H_z = 19 $\rightarrow$ 85 Å. In all three graphs it can be seen that one or other of the peaks can disappear at certain thicknesses; however, this is unlikely to be noticed in practice due to the averaging effect of the divergent incident beam (Holmes, Cockayne and Ray 1974; Melander and Sandström 1974; and see Chapter 4). To the right of each set of curves have been drawn two dotted boundary lines. These are the result of comparing all three graphs and represent the limits outside which no peaks are expected to occur. From these we deduce that, for Z dipoles in $(20\bar{2})$-type reflections,

$$\Delta_z = \Delta_{z\ obs} - 10 \pm 11 \text{ Å} \qquad (3.4)$$

If the value of H_z were known, then a set of curves such as fig. 3.6 would provide a more useful relation with a different correction factor and somewhat lower limits. When this information is not available, as is the case here, all one can say is that Δ_z lies in the range given by (3.4).

Fig. 3.9 displays the results of calculations on five S dipoles with various combinations of the parameters Δ_s, H_s and d as follows:- Δ_s = 33 $\rightarrow$ 60 Å, H_s = 19 $\rightarrow$ 85 Å, d = 1.00 $\rightarrow$ 1.05 ξ_g. Again estimates of the likely variations in peak positions have been made and the value of Δ_s deduced from $(20\bar{2})$-type images is expected to lie in the range

$$\Delta_s = \Delta_{s\ obs} - 13 \pm 11 \text{ Å} \qquad (3.5)$$

3.3.2 Weak-beam images at the (112) pole

The reflection of interest here is $11\bar{1}$. As $|\underline{g}.\underline{b}| = \frac{2}{3}$ for the Shockley partials, the outer stacking faults now give contrast. When imaged using the $\bar{1}\bar{1}1$ reflection, the peaks from the Shockley dislocations lie inside the stacking fault region and the resulting image is complex. The $11\bar{1}$ images, which display outside contrast, are thus more useful. Preliminary six-beam calculations have been performed for this

configuration with $s_g = 2.34.\ 10^{-2}$ Å^{-1} for one Z and S faulted dipole only. These have the dimensions $\Delta'_z = \Delta'_s = 48.5$ Å and $H'_z = H'_s = 38$ Å. The curves of peak position are shown in figs. 3.10 and 3.11 for four different depths, $d = 0.5 \longrightarrow 1.05\ \xi_g$. As can be seen, the occasional disappearance of one or other of the peaks is far more common here than in the case of the $20\bar{2}$ reflection. The effect of the incident beam divergence is unlikely to prevent large variations in intensity. The expected range of peak positions based on these initial computations is as follows:-

$$\Delta'_z = \Delta'_{z\ obs} - 6 \pm 6 \text{ Å} \qquad (3.6)$$

$$\Delta'_s = \Delta'_{s\ obs} - 8 \pm 7.5 \text{ Å} \qquad (3.7)$$

3.4 Experimental procedure

(111) slices of pure (Johnson-Matthey 99.998%) copper, spark-cut from single crystals, were deformed by bending, and 3 mm discs cut from them. Specimens were then prepared by a two-stage electropolishing process. Dishes were formed in the discs by jet-polishing with a 15% by volume solution of HNO_3 in distilled water at 80 V with a current of 300 mA. Finally the foil was thinned to perforation in a 33% by volume solution of HNO_3 in methanol at 3 V and a temperature of $\sim -60^{\circ}$C.

The specimens were studied in a Jeol JEM 100B operating at 100 kV. Weak-beam micrographs of the defects were recorded in the six $\{220\}$ reflections at the (111) pole and in the $\{111\}$ reflections at the (112), (121) and (211) poles. The value of s_g for each reflection was estimated from the position of Kikuchi bands in the diffraction pattern and was set as near as possible to that used in the computations. This corresponded to the Ewald sphere cutting the row of systematic reflections at 3.1g for the $\{220\}$ images and 6.5g for the $\{111\}$ images. Care was taken to ensure that no reflection was strongly excited since this can introduce undesirable thickness and depth oscillation effects (Cockayne 1972). Strong-beam images from the incident beam were also recorded with s_g small and positive for the coupled beam.

3.5 Results from the weak-beam observations

3.5.1 The weak-beam {220} images

Numerous faulted dipoles of various size were observed, all displaying similar features of contrast. The most relevant one for the purpose of estimating the stacking-fault energy is that with the largest Δ_{obs} in $20\bar{2}$ (or $02\bar{2}$), and micrographs of this dipole taken under different diffraction conditions are shown in fig. 3.12. The experimental {220} images display the features predicted from the computations as discussed in section 3.3. The $\bar{2}02$ and $0\bar{2}2$ images have two relatively intense closely-spaced peaks (these merged into one in observations of narrower dipoles). The $20\bar{2}$ and $02\bar{2}$ images have two weaker but more widely separated peaks. Inside these peaks one or two extremely faint peaks can occasionally be seen. These are associated with the stair-rod dislocations and the central stacking fault, and a suggestion of one such peak can be seen in the theoretical profile of fig. 3.5. The separation of the Shockley peaks is not constant along the length of the dipole; in several places the peaks deviate from the straight-line configuration. Such deviations may be due to discrete steps in the dipole height. The image at these points is similar in appearance to those of jogs on dissociated dislocation ribbons (Carter and Ray 1974, Carter unpublished). The $2\bar{2}0$ image, for which $\underline{g}$ is parallel to the line of the dipole, shows no contrast as expected.

The average separation of the peaks in the $(20\bar{2})$-type image, as measured along the widest section where both peaks are reasonably straight, is 70 Å. It is not possible from such an image to say whether it is a Z or an S dipole. Applying the relations (3.4) and (3.5) derived in section 3.3.1 gives the possible range of Δ_z and Δ_s for the widest image of a faulted dipole in copper observed under weak-beam conditions:

$$\Delta_z = 60 \pm 11 \text{ Å} \tag{3.8}$$

$$\Delta_s = 57 \pm 11 \text{ Å} \tag{3.9}$$

These results can be used in conjunction with figs. 3.2 and 3.3 to derive

an upper limit on the stacking-fault energy. From fig. 3.2 relation (3.8) gives for the Z dipole

$$\gamma_{max(z)} = 47 \pm 8 \text{ erg cm}^{-2} \qquad (3.10)$$

This follows simply from the equilibrium curves and does not involve the energy calculations. In the case of an S dipole it is assumed that a faulted dipole cannot have a height greater than that given by the M-S transition curve in fig. 3.3. Then (3.9) gives for the S dipole

$$\gamma_{max(s)} = 57 \pm 10 \text{ erg cm}^{-2} \qquad (3.11)$$

3.5.2 The weak-beam {111} images

The weak-beam images in $1\bar{1}1$ and $\bar{1}11$ are similar and narrow in appearance. Occasionally two closely-spaced peaks may be observed. In the $11\bar{1}$ reflection, perpendicular to the dipole line direction, the image is much wider and consists of two broad peaks which display large variations in intensity. This is in agreement with the computer calculations of section 3.3.2 and the curves of figs. 3.10 and 3.11 where it can be seen that the disappearance of one or both peaks is predicted for certain values of dipole depth and foil thickness.

The average peak separation was measured over the same section of the dipole as was used for the $(20\bar{2})$-type images and found to be 70 Å. Applying the relations (3.6)and(3.7) gives the possible range in widths of Z and S dipoles as

$$\Delta'_z = 64 \pm 6 \text{ Å} \qquad (3.12)$$

$$\Delta'_s = 62 \pm 7.5 \text{ Å} \qquad (3.13)$$

It was stated in section 3.3.2 that these relations are only based on initial computations for one size of faulted dipole and so should be applied with caution. However, the calculations of the $(20\bar{2})$-type images show that a wide range of dipole widths and heights give rise to peaks with similar behaviour. It is likely that this is also true for the $11\bar{1}$ reflection, so the results (3.12) and (3.13) are probably good approximations. Simple geometry produces formulae for the height of Z and S dipoles with

particular values of Δ and Δ' as follows:-

$$H_z = 3\left[\Delta'_z - \frac{2\sqrt{2}}{3}\Delta_z\right] \tag{3.14}$$

$$H_s = 3\left[\frac{2\sqrt{2}}{3}\Delta_s - \Delta'_s\right] \tag{3.15}$$

Substitution of (3.4), (3.5), (3.6) and (3.7) into (3.14) and (3.15) shows that the possible errors in determining H by this method are very large. This is because of the small angle ($\sim 20^{\circ}$) of tilt between the two poles; the value of Δ is insensitive to small changes in H. However, (3.14) and (3.15) give the maximum possible values of H in the worst case. These are

$$H_{max(z)} = 71 \text{ Å} \tag{3.16}$$

$$H_{max(s)} = 30 \text{ Å} \tag{3.17}$$

We therefore conclude that the dipole in fig. 3.12 could not have been higher than this, and may well have had a considerably lower value of H. Comparison of $H_{max(s)}$ with fig. 3.3 and the result from (3.9) that $\Delta_{min(s)} = 46$ Å shows that the maximum possible value of γ in the S case is reduced to

$$\gamma_{max(s)} = 36 \text{ erg cm}^{-2} \tag{3.18}$$

This result is not now dependent on the energy calculations of the critical height but only on the elasticity equilibrium calculations, as is the case for $\gamma_{max(z)}$ given in (3.10) . Therefore this result for $\gamma_{max(s)}$ does not depend on the assumed ratio of γ_E / γ_I (unless this was so high that the M-S transition curve lay to the left of the point $\Delta_s = 46$ Å , $H_s = 30$ Å in which case $\gamma_{max(s)}$ would be reduced even further).

3.5.3 Faulted dipoles in other orientations

The results obtained in this section from the weak-beam micrographs in fig. 3.12 have been based on the computed images of section 3.3 where it was assumed that the Shockley partial dislocations bounded faults on the (111) plane (i.e. the foil plane). Another orientation of faulted dipole is possible having the same line direction but in which the Shockley partials bound faults on the $(\bar{1}\bar{1}1)$ plane. It is not immediately obvious in which orientation an observed dipole lies since in both cases the dipole is invisible in the $\pm(2\bar{2}0)$ reflections and in eachcase the two

images obtained in $\pm(20\bar{2})$ are identical to those obtained in $\pm(02\bar{2})$.

Images have been computed for 'inclined' dipoles with dimensions in the range $\Delta_z = \Delta_s = 47 \longrightarrow 84$ Å , $H_z = H_s = 19 \longrightarrow 65.5$ Å . The results indicate that the inside-outside contrast effect is small for the inclined dipoles, the difference in Δ_{obs} being $\lesssim 10$ Å . This figure was found to be much larger in the computations of section 3.3. For example, the profiles in fig. 3.5 have peak separations differing by ~ 25 Å . The fact that the value is smaller in the case of the inclined dipole may be understood by noting that the Burgers vectors of the partial dislocations then make relatively small angles with the direction of the electron beam and hence $\underline{g}.\underline{b}_{\wedge}\underline{u}$ contrast effects are dominant in the image. The measured difference is ~ 30 Å for the dipole in fig. 3.12. It is therefore concluded that this dipole is in fact of the type assumed in section 3.3.

3.6 Strong-beam images and their interpretation

3.6.1 Strong-beam {220} images

Previous studies of faulted dipoles in pure copper have used conventional strong-beam imaging techniques (Hüssermann and Wilkens 1966; Steeds 1967b). In this section their results and interpretations are compared, and the experimental and theoretical images obtained in the present study are also discussed. The strong-beam {220} images shown in fig. 3.12 display contrast effects typical of such images observed in this investigation. Two intensity minima can be seen, whose width and intensity vary considerably along the length of the dipole, and which are not sensitive to the fine detail observed in the weak-beam images. The lines in the $(\bar{2}02)$-type images are darker than those in the $(20\bar{2})$-type images, and the latter also tend to be asymmetrical, in that one of the lines is generally lighter than the other. In view of these effects it is difficult to define a meaningful image width (minima separation), but an approximate value for the $(20\bar{2})$-type images is 90 Å . The widest image in copper observed by Steeds (1967b) was 68 Å , and 125 Å was reported by Hüssermann and Wilkens (1966).

From his calculations for Z dipoles at various depths in foils of thickness $t \geqslant 4\,\xi_g$, Steeds (1967b) found that the bright-field $\{220\}$ image width was related to H and independent of Δ for $\Delta \leqslant \frac{H}{\sqrt{2}}$. (The line $\Delta = \frac{H}{\sqrt{2}}$ lies just under his M-Z transition curve in fig. 3.2). Using this result and attributing his widest image to the transition configuration he derived a value for the stacking-fault energy. This interpretation of the image width differs from the weak-beam case discussed in section 3.3.1, where it was shown that Δ_{obs} depends on Δ rather than on H. Häussermann and Wilkens (1966) did not observe separate minima in every case and in their analysis preferred to use the half-width of the whole image. They calculated half-widths and minima separations for transition configuration dipoles at a depth of $d = 0.25\,\xi_g$ in a foil of thickness $t = 3\,\xi_g$. From computations for other dipoles they found that, at a given value of γ, dipoles of height less than the transition height resulted in smaller minima separations and half-widths, and that for dipoles lying at depths greater than $d = 0.4\,\xi_g$ the half-width was reduced by up to 20%. (Presumably the minima separation is also reduced by a similar figure). Like Steeds, they concluded that the widest possible image width would correspond to the transition configuration dipole. Use of their analysis on a dipole which is not in the transition configuration or is not close to the surface should underestimate the height and so overestimate the stacking-fault energy. Values of γ obtained in this way are therefore to be regarded as upper limits.

The dipole in fig. 3.12 was selected for having the largest value of Δ_{obs} in the $(20\bar{2})$-type weak-beam image, and from the results of section 3.5 is probably not in the transition configuration. However, its bright-field image width ($\sim$ 90 Å) does lie between the previously reported widest images of faulted dipoles in copper, 68 Å and 125 Å. The high value of γ given by Steeds (1967b), 150 ± 30 erg cm^{-2}, must result from his not having observed the widest possible image. The analysis of a bright-field image

from the results of previous workers is uncertain because of two conflicting effects. Firstly, the curve of Häussermann and Wilkens (1966) gives a larger dipole height than that of Steeds (1967b) for the same image width. For example, taking the widest reported image of 125 Å , the two heights are 67 Å and 61 Å . (This discrepancy increases with decreasing image width; for an image width of 90 Å the two heights are 32 Å and 44 Å . This effect would become important for materials with smaller dipoles). Secondly, the M-Z transition curve of Seeger and Wobser (1966) gives a higher value of γ than that of Steeds (1967a) for the same height (see fig. 3.4). Taking H = 67 Å gives γ = 73 and 51 erg cm^{-2} ; H = 61 Å results in γ = 79 and 55 erg cm^{-2} . Therefore different values of γ arise depending on the analysis used. In the present case this is mainly because of the differences in the transition curves, but the relation between image width and dipole height would become more important in other materials with smaller transition dipoles.

The author's calculations suggest that the dependence of the image on foil thickness is more complicated than previously thought, and that this makes the analysis of strong-beam images even more difficult. To illustrate this point, two-beam computed images for two Z dipoles in $\underline{g} = \pm(20\bar{2})$ are shown in figs. 3.13 and 3.14 for different foil thicknesses and it can be seen that the general features of the curves agree with the experimental images in fig. 3.12 as described above. The dipole dimensions approximately correspond to the Steeds M-Z transition configurations for γ = 40 erg cm^{-2} and γ = 100 erg cm^{-2} . At these thicknesses in both $\pm \underline{g}$ the image width for the γ_{40} dipole is greater than that for the γ_{100} dipole. However, there is a considerable overlap in widths; for example, in fig. 3.13 the two widths for the γ_{40} dipole are 52 Å and 118 Å , whereas those for the γ_{100} dipole are 36 Å and 90 Å . A similar overlap occurs in the case of S dipoles. This shows that the image width of a dipole in the critical configuration can vary considerably, so that even with careful

averaging of observed widths along the length of the dipole it is difficult to specify an accurate figure for use with either of the published curves. Such effects may explain to some extent the large spread in reported maximum widths of faulted dipole images in copper. It is possible that larger variations in image width than would have been noted previously occur because of the thinner foils used in the present calculations. These were chosen to correspond with the order of thickness usual in weak-beam investigations, and so are applicable to the strong-beam images obtained in this study.

It is concluded that in the case of these strong-beam images the determination of the dipole height is susceptible to large errors because of the substantial overlap in possible image widths from dipoles of greatly differing dimensions. Such effects may also apply to strong-beam images in thicker foils in which case the possible spread in the value of the stacking-fault energy determined from the widest image is even larger than shown above. It has been demonstrated that it is possible in the case of copper to obtain an upper limit to the stacking-fault energy from weak-beam images (which are relatively independent of depth and thickness effects) without reference to the transition curves; such methods are therefore preferable to strong-beam imaging techniques when studying faulted dipoles in this material.

3.6.2 Strong-beam $\{111\}$ images

The strong-beam images taken in $\{111\}$ reflections display contrast effects analagous to the weak-beam case, in that the $1\bar{1}1$ and $\bar{1}11$ images are similar in appearance, narrow, and occasionally have two closely-spaced minima. The $11\bar{1}$ image is wider and has two broad intensity minima whose width and intensity vary along the length of the dipole. The average separation of these lines is 106 Å. This result is interesting in that Steeds (1967b) did not observe two intensity minima in $\{111\}$ images in the case of copper, but preferred such images in the case of silver and gold since their interpretation does not involve the use of transition curves. Applying his analysis gives $\gamma_{max} = 33.5$ erg cm^{-2}. Calculations of strong-beam $11\bar{1}$ images

have not been performed here, but it seems likely that the usefulness of this result is limited because of large variations in the possible image width, as is the case for $\{220\}$ reflections.

3.7 Summary and conclusions

Because of the many points covered in this chapter, it seems preferable for the sake of clarity to present a summary and general conclusions in note form.

(i) It has been shown that from $\{220\}$ weak-beam images of faulted dipoles in copper it is possible to determine the horizontal separation of the Shockley partials to within a random error of $\pm$ 11 Å , which is caused by the dependence of the image width on the depth of the dipole in the foil, its height, and the foil thickness. Precise knowledge of the dipole height would reduce this uncertainy in Δ.

(ii) Many faulted dipoles were studied under both weak-beam and strong-beam conditions. The dipole with the widest $(20\bar{2})$-type weak-beam image was selected for detailed study and the width corresponded to $\Delta_z = 60 \pm 11$ Å , or $\Delta_s = 57 \pm 11$ Å .

(iii) Equilibrium configurations of both Z and S faulted dipoles have been computed using the elastic constants of Huntington (1958) and the anisotropic elasticity expressions of Stroh (1958) for infinite straight dislocations. The value of Δ_z obtained from the $(20\bar{2})$-type weak-beam images gives the result $\gamma_{max(z)} = 47 \pm 8$ erg cm^{-2} from these curves. The value of Δ_s when combined with these curves and the M-S transition curve of Steeds (1967a) gives $\gamma_{max(s)} = 57 \pm 10$ erg cm^{-2} .

(iv) Weak-beam $11\bar{1}$ images enable a maximum limit to be set on the height H of the dipole although the actual height could be much lower than this. For the dipole studied here $H_{max(z)} = 71$ Å and $H_{max(s)} = 30$ Å . It may be possible to obtain a precise figure for H as well as Δ by tilting the specimen through a large angle. An exact value of γ , rather than an upper limit, would result.

(v) The figure for the maximum height in the case of an S dipole sets a new lower maximum limit on the stacking-fault energy when combined with the minimum value of Δ_s . The new result is $\gamma_{max(s)} = 36$ erg cm^{-2} . This result is now independent of the transition curve calculations, as is $\gamma_{max(z)}$ in (iii) above. The independence is an advantage since previous authors' transition curves differ significantly (Seeger and Wobser 1966; Steeds 1967a).

(vi) Previous studies of faulted dipoles in copper have disagreed on the value of the transition heights (Seeger and Wobser 1966; Steeds 1967a), and on the relationship between the strong-beam image width and dipole height (Häussermann and Wilkens 1966; Steeds 1967b). A large range of γ therefore results from possible interpretations of the same image. The present calculations also suggest that there is a wide overlap of image width from dipoles of greatly different dimensions due to the dependence of the image on foil thickness. It is concluded that the determination of the stacking-fault energy from strong-beam images is susceptible to large errors.

(vii) It is not possible to state for certain whether the dipole of fig. 3.12 was in the S or Z configuration. From the values for the upper limit on the stacking-fault energy derived in the two cases it follows that, for copper

$$\gamma_{max} = 47 \pm 8 \text{ erg } cm^{-2} .$$

(viii) The stacking-fault energy of copper has been determined by Cockayne, Jenkins and Ray (1971) and Stobbs and Sworn (1971) from weak-beam observations of single dissociated dislocations and found to be 41 ± 9 and 41 erg cm^{-2} , respectively. The elasticity calculations and the displacement fields in the image computation used in these and the present investigations assumed the dislocation cores to be singular. It has been shown by Cockayne and Vitek (1974) that in the case of a dissociated dislocation the use of a finite core width as opposed to a singular core

can alter the value of γ derived from weak-beam images. As an interaction of extended cores would involve different dislocations and line orientations in the two types of defect, it is interesting to note that, assuming singular cores, the upper limit for γ obtained here is close to the values of γ derived in studies of dissociated dislocations.

(ix) The good agreement noted in (viii) suggests that weak-beam observations of faulted dipoles may reliably be used to estimate the stacking-fault energies of materials for which γ and the elastic constants are such that the dissociation of single dislocations cannot be resolved with ease.

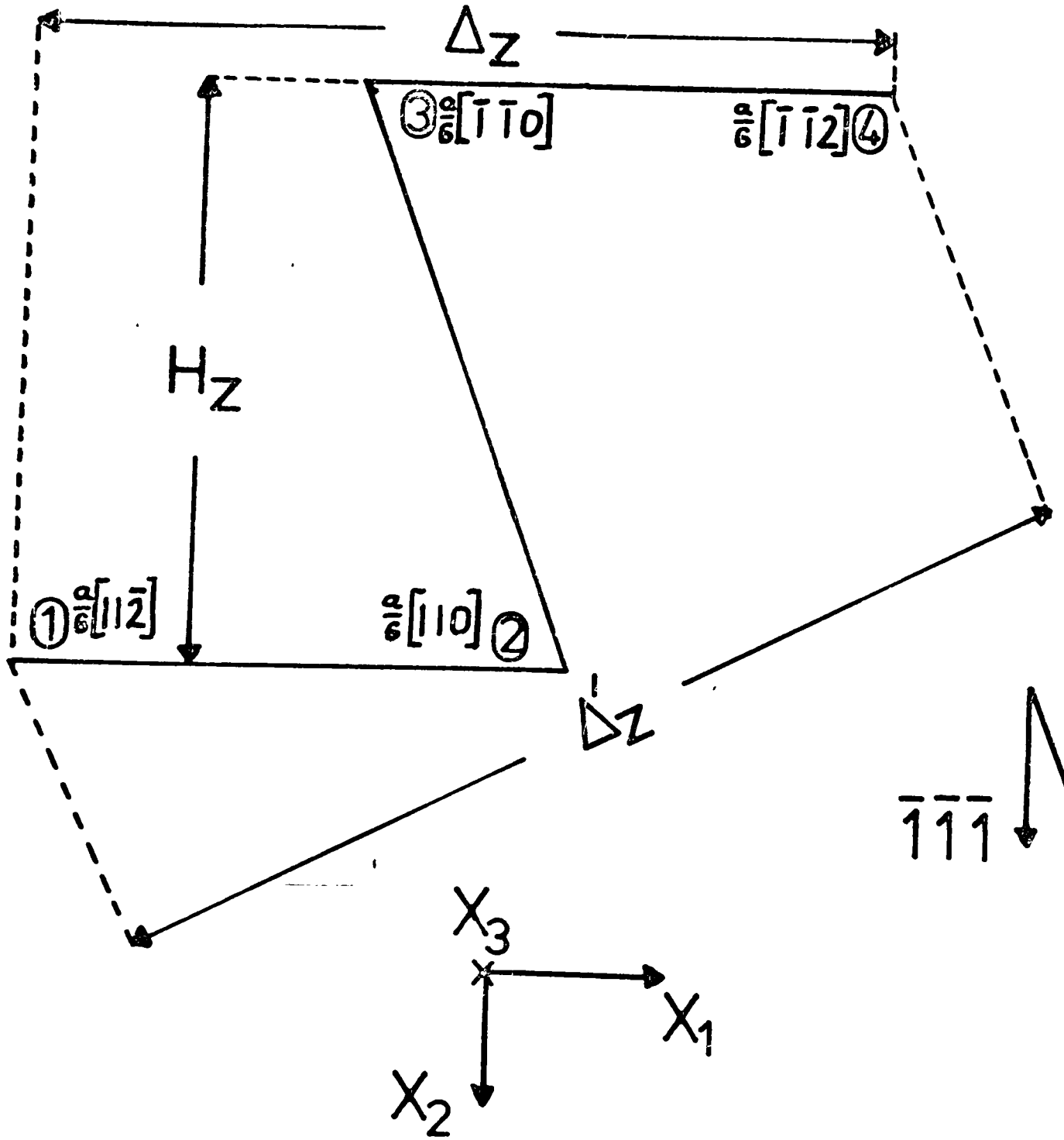
Δz
Hz
③ a/6[1̄1̄0]
a/6[1̄1̄2] ④
① a/6[112̄]
a/6[110] ②
Δ'z
X3
X1
X2

1̄1̄1̄
1̄1̄2̄

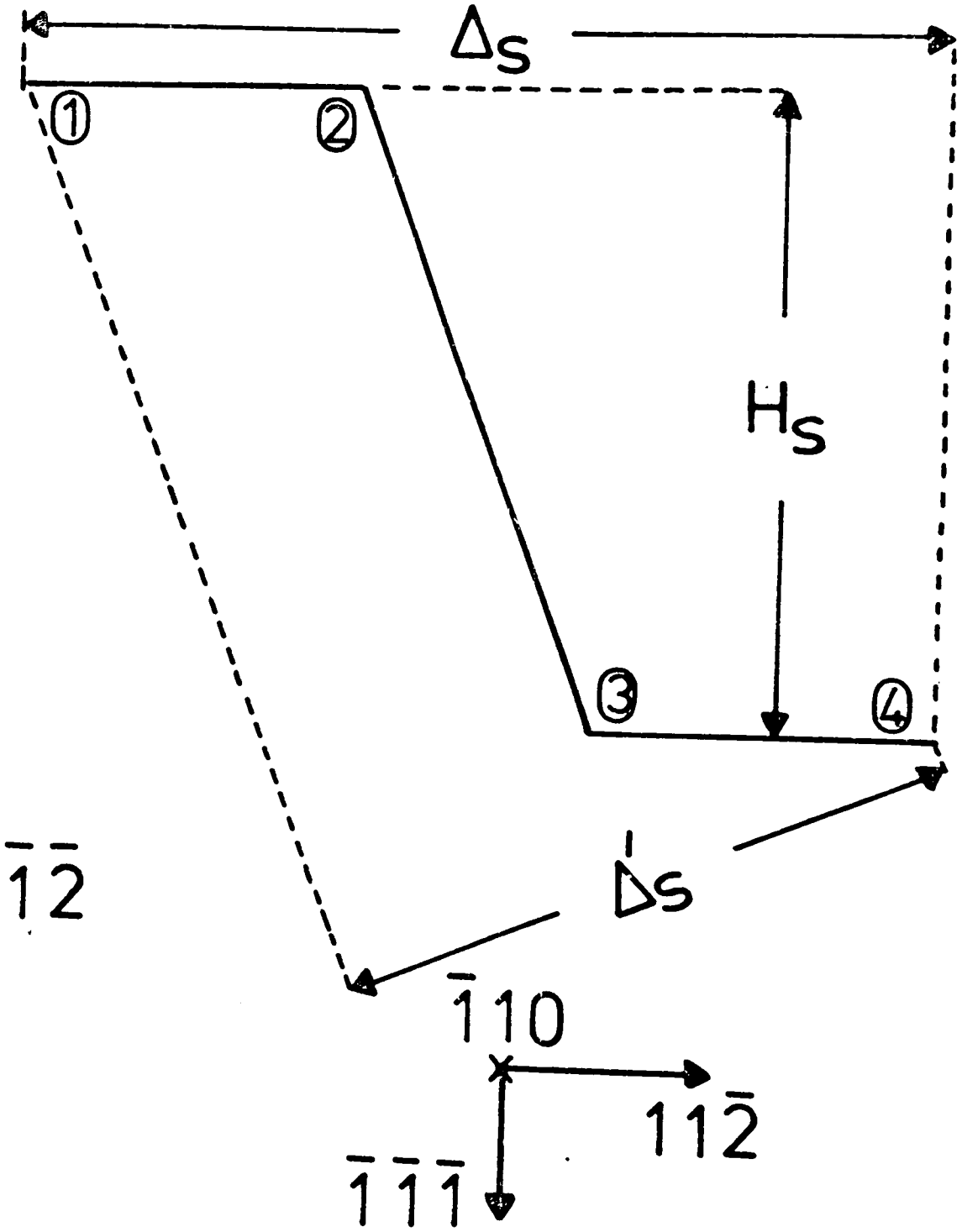
Δs
①
②
Hs
③
④
Δ's
1̄10
11̄2̄
1̄1̄1̄

Figure 3.1 The geometry of Z and S faulted dipoles. The dislocations all have the line direction $[\bar{1}10]$ which is into the paper.

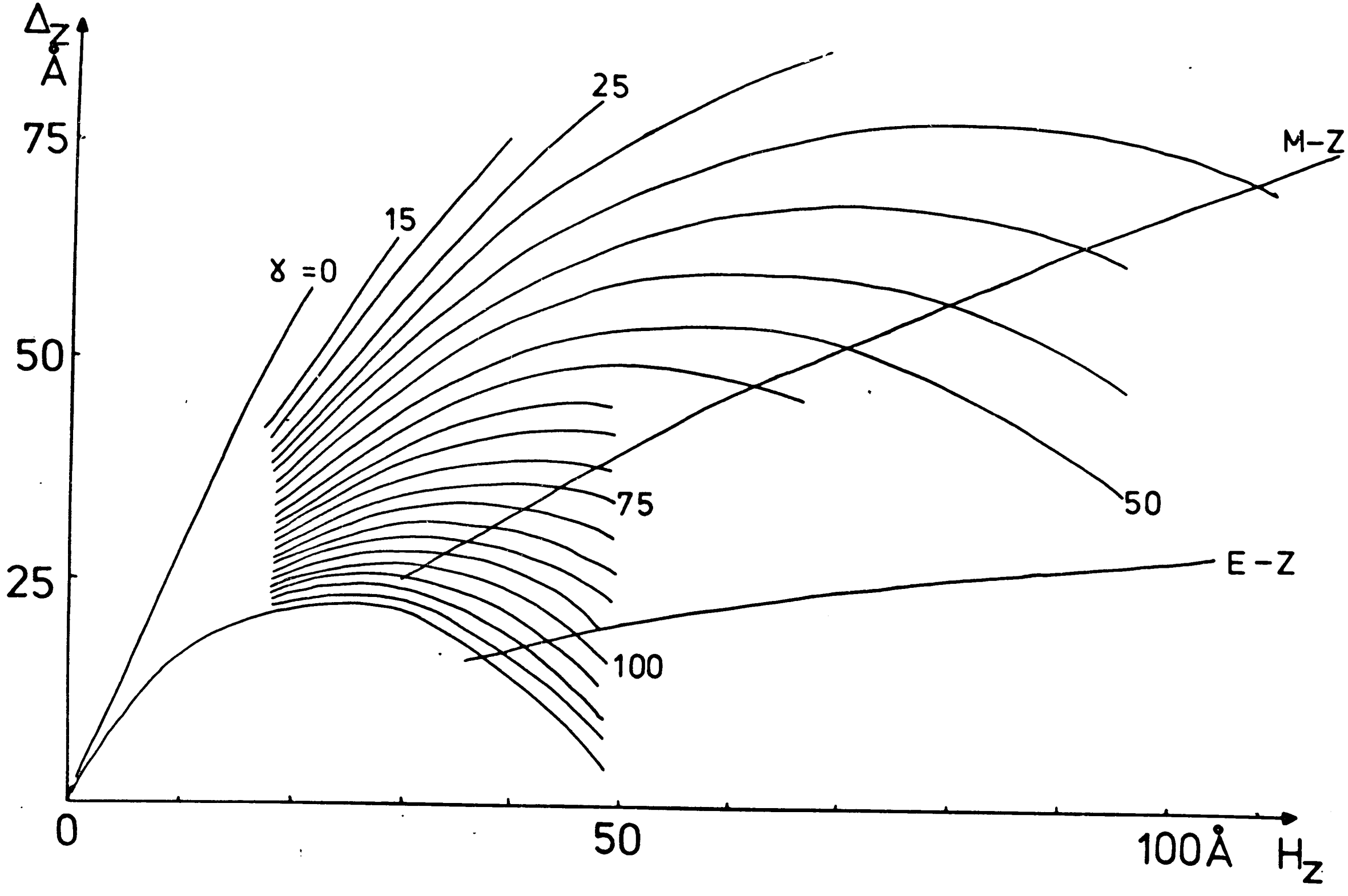
Δ_Z
Å
75
50
25
0
50
100Å
H_Z
γ =0
15
25
75
100
M-Z
50
E-Z

Figure 3.2 Equilibrium curves for Z faulted dipoles in copper calculated using anisotropic elasticity with different possible values of δ. The transition curves of Steeds (1967a) are also shown.

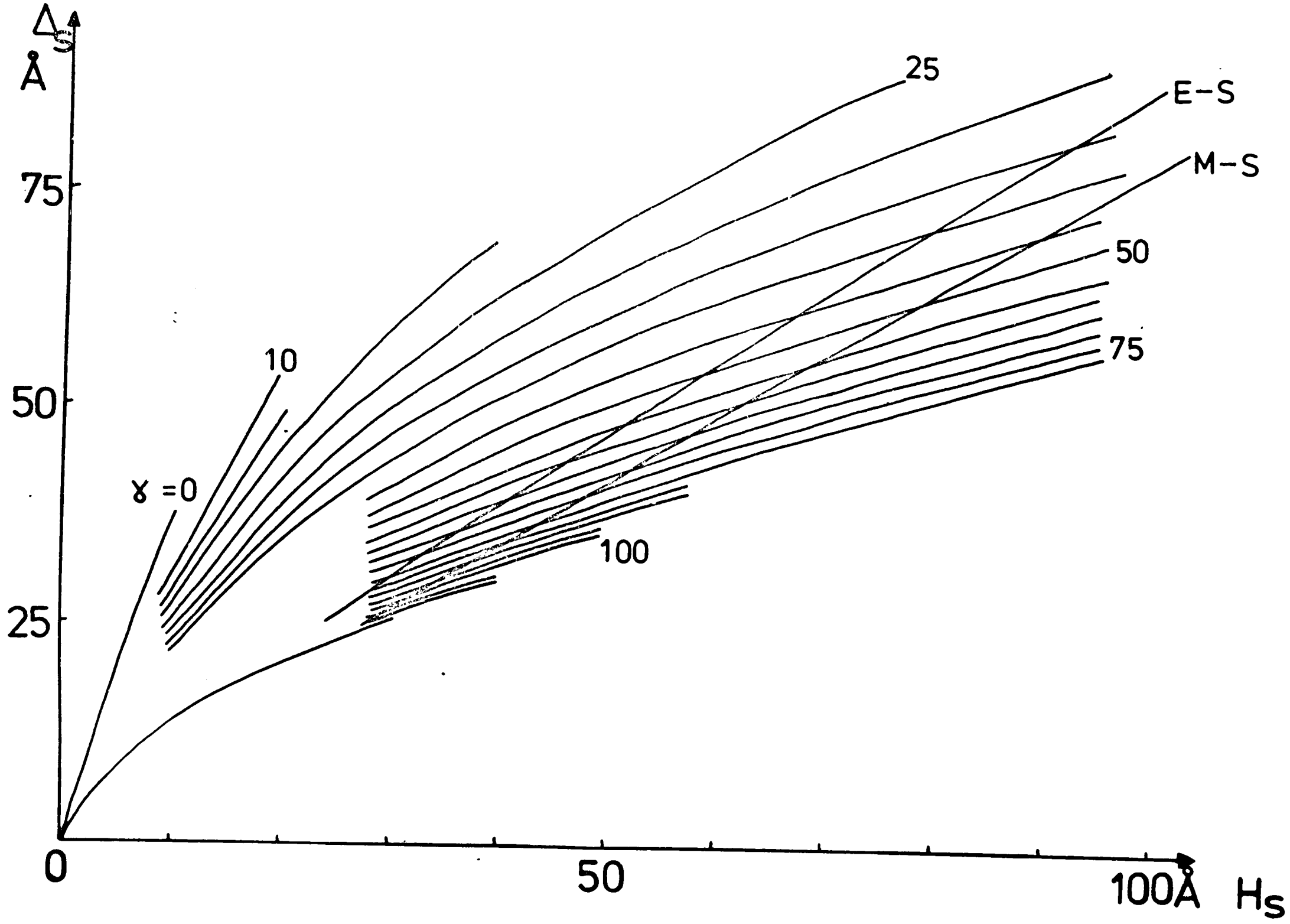
Δs
Å
75
50
25
0
50
100Å
Hs
25
E-S
M-S
50
75
10
γ =0
100

Figure 3.3 Equilibrium curves for S faulted dipoles in copper calculated using anisotropic elasticity with different possible values of γ. The transition curves of Steeds (1967a) are also shown.

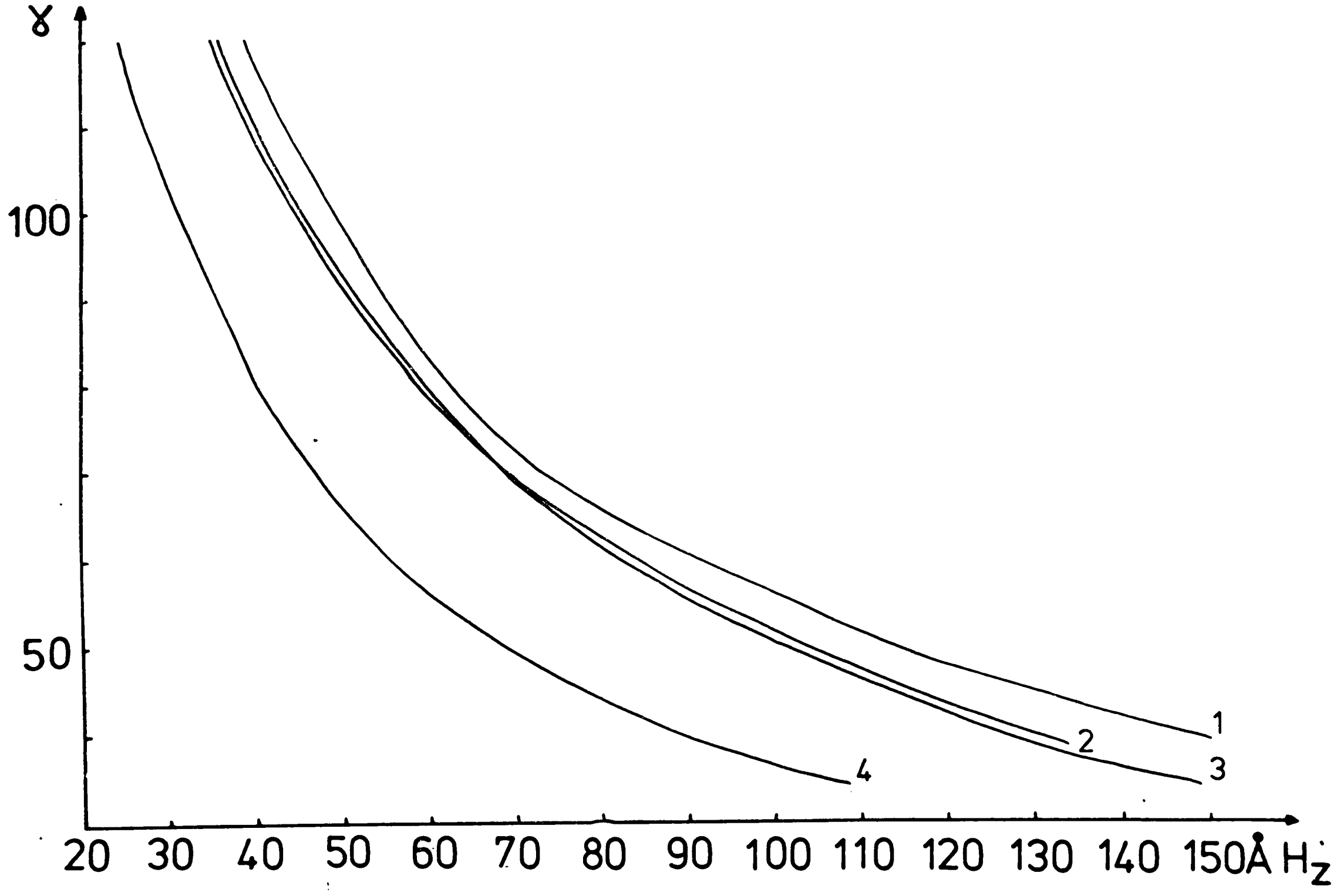
%
100
50
1
2
3
4
20 30 40 50 60 70 80 90 100 110 120 130 140 150Å Hz

Figure 3.4 A comparison of transition curves for Z-faulted dipoles in copper.

(1) E-Z
(2) M-Z
} Seeger and Wobser (1966)

(3) E-Z
(4) M-Z
} Steeds (1967a)

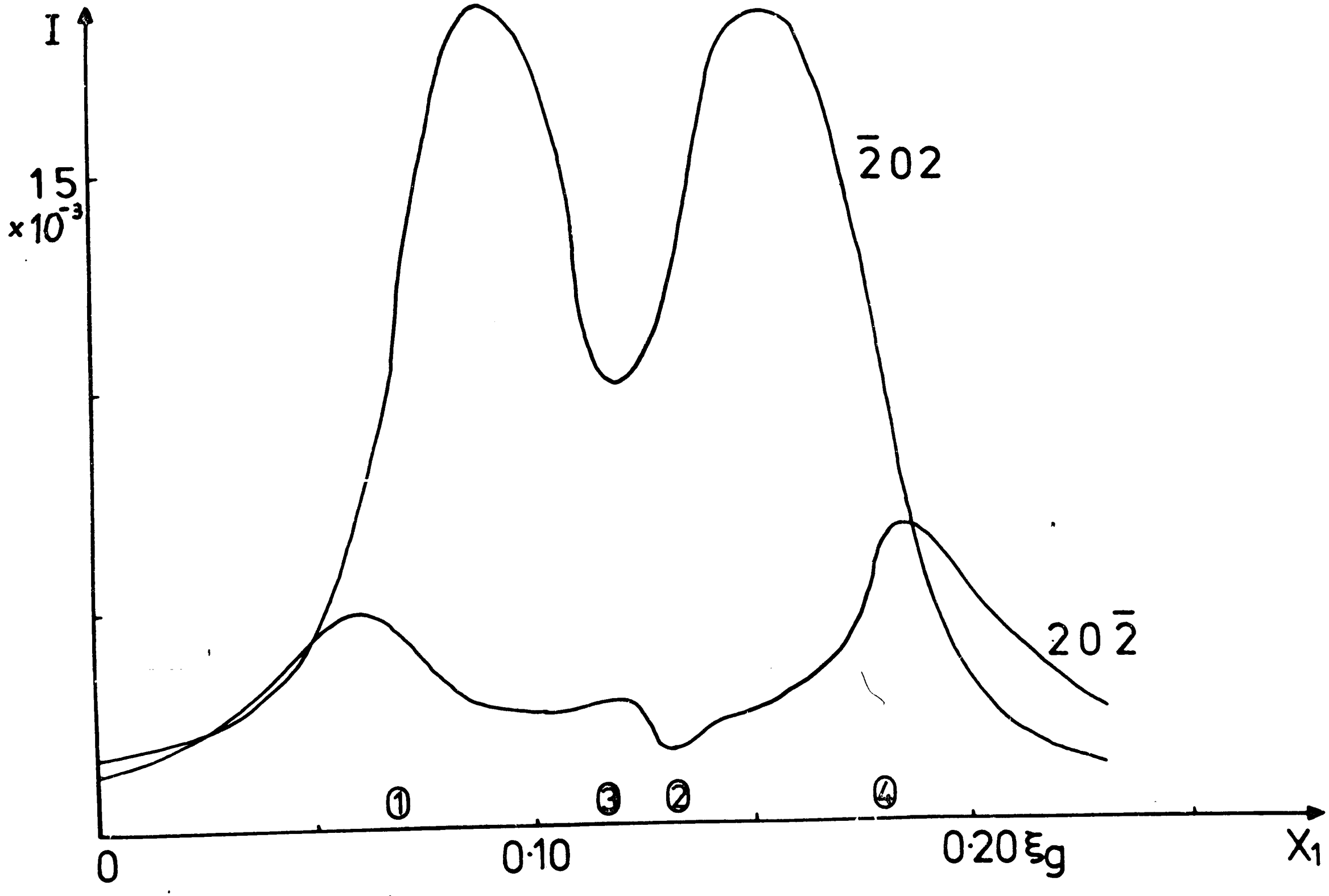
I
15
×10⁻³
0
0·10
0·20 ξg
X1
1
3
2
4
2̄02
202̄

Figure 3.5 Computed weak-beam image profiles for a Z-faulted dipole in $\pm(20\bar{2})$. H=0.045, Δ =0.112, d=1.0, and t=2.11 ξ_g (ξ_g=418 Å). (1) to (4) indicate the relative positions of the partial dislocations as given in fig. 3.1.

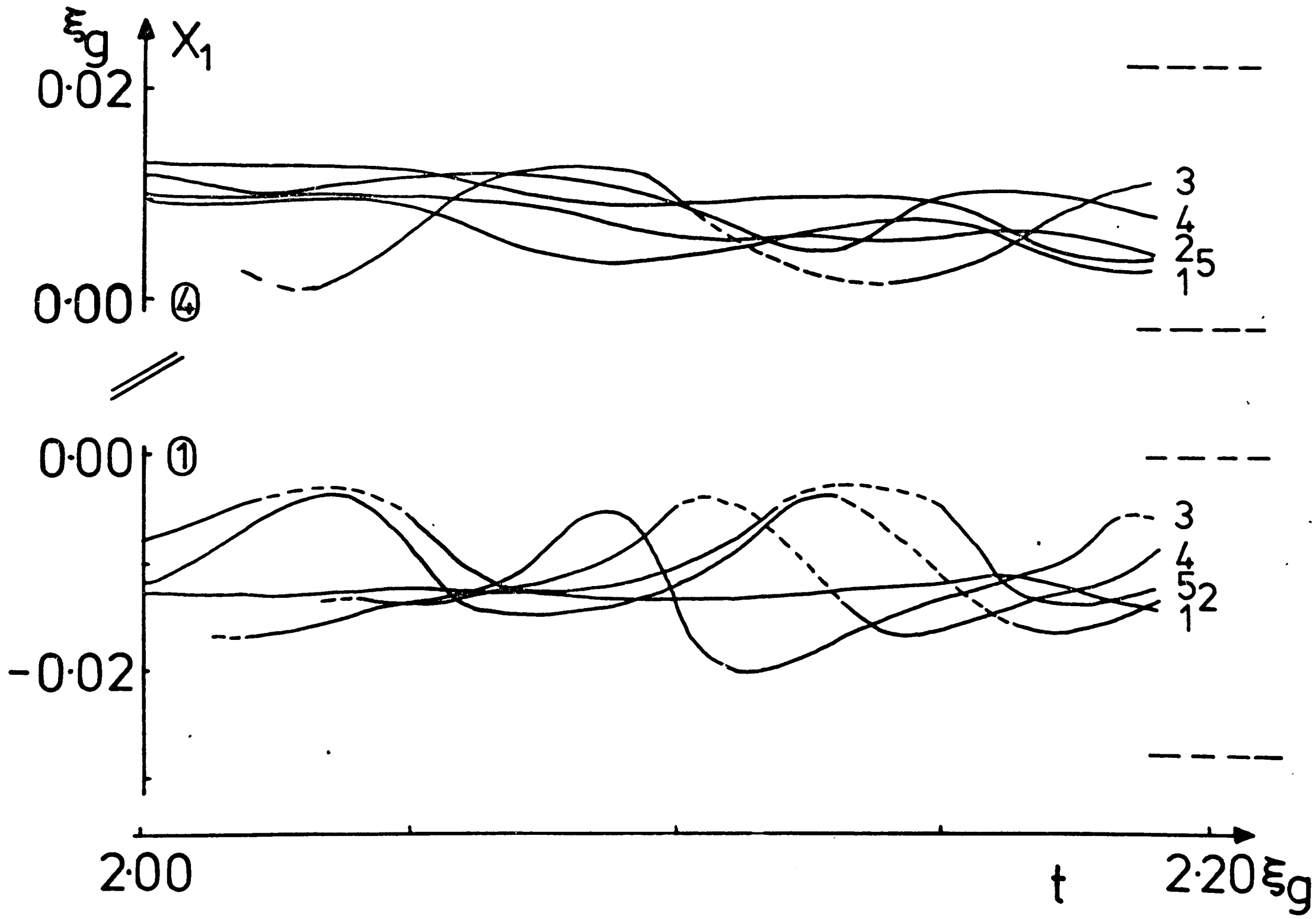
ξ_g
X_1
0·02
0·00
④
0·00
①
3
4
2
5
1
3
4
5
2
1
-0·02
2·00
t
2·20 ξ_g

Figure 3.6 The variations in the positions of the outer image peaks with thickness. Z dipole, $\underline{g}=20\bar{2}$, Δ =0.112, H=0.045 ξ_g, various d as marked:-

(1) 1.000 ξ_g

(2) 1.025

(3) 1.050

(4) 1.075

(5) 1.100

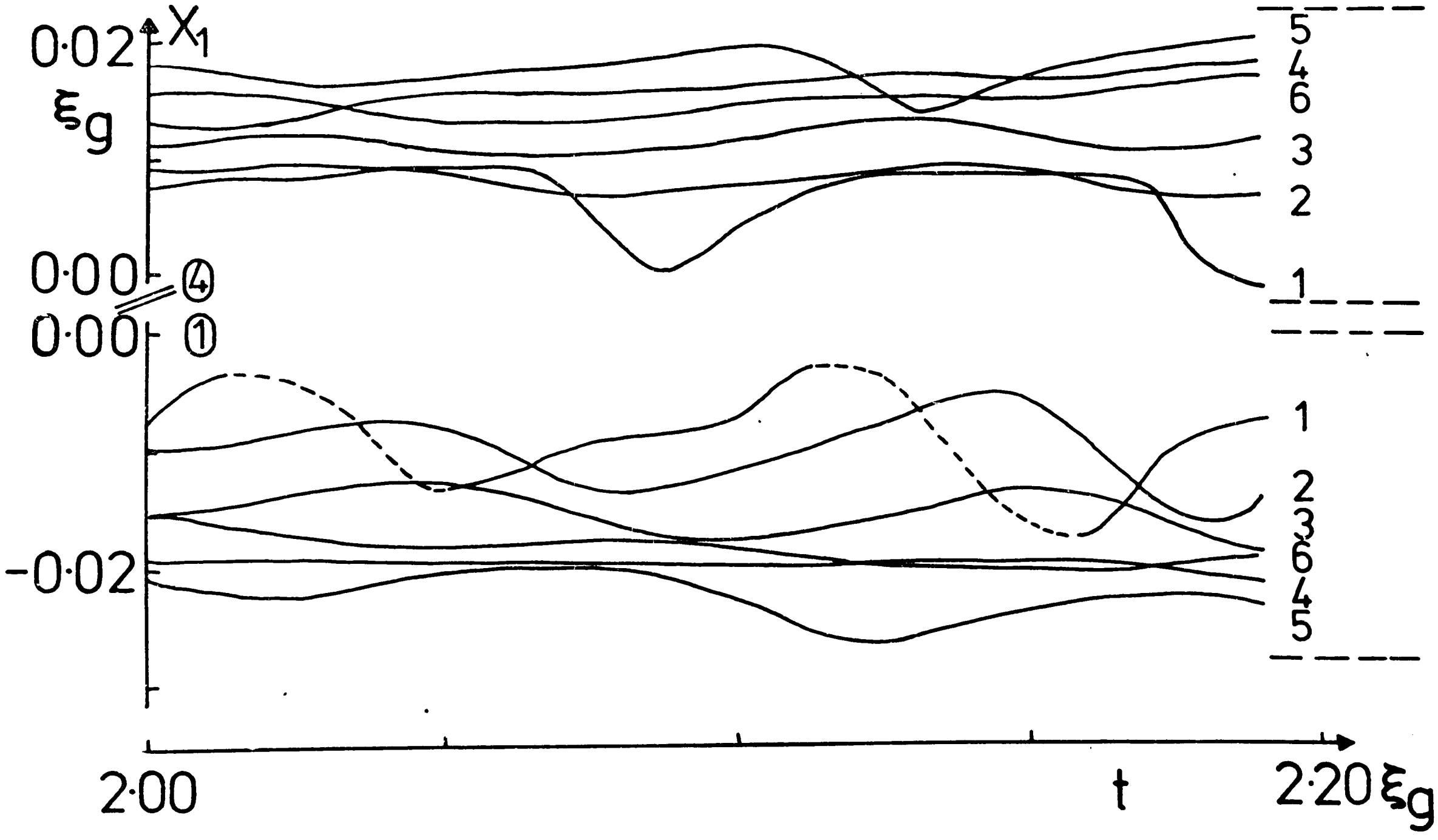
0·02
X1
ξg
0·00
④
0·00
①
-0·02
5
4
6
3
2
1
1
2
3
6
4
5
2·00
t
2·20 ξg

Figure 3.7 The variations in the positions of the outer image peaks with thickness. Z dipole, $\underline{g}=20\bar{2}$, Δ =0.08, d=1.0 ξ_g, various H as marked:-

(1) 0.0226 ξ_g

(2) 0.0450

(3) 0.0676

(4) 0.0900

(5) 0.1126

(6) 0.1352

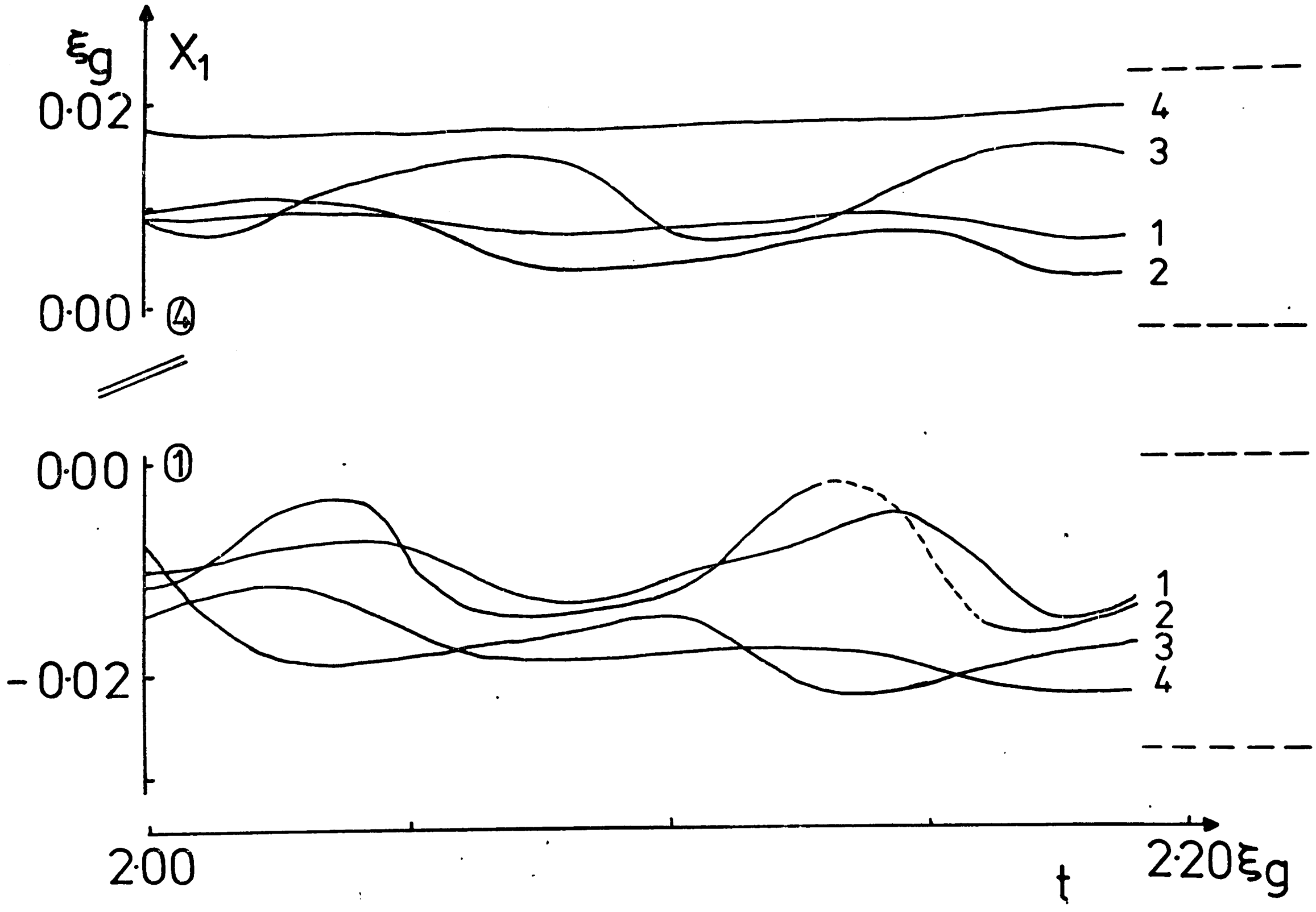
ξ_g
X_1
0·02
0·00
④
4
3
1
2
0·00
①
-0·02
1
2
3
4
2·00
t
2·20ξ_g

Figure 3.8 The variations in the positions of the outer image peaks with thickness. Z dipole, $\underline{g}=20\bar{2}$, $d=1.0\,\xi_g$, various Δ and H as marked:-

(1)	$\Delta = 0.080\,\xi_g$	$H = 0.0450\,\xi_g$
(2)	0.112	0.0450
(3)	0.144	0.1466
(4)	0.144	0.2026

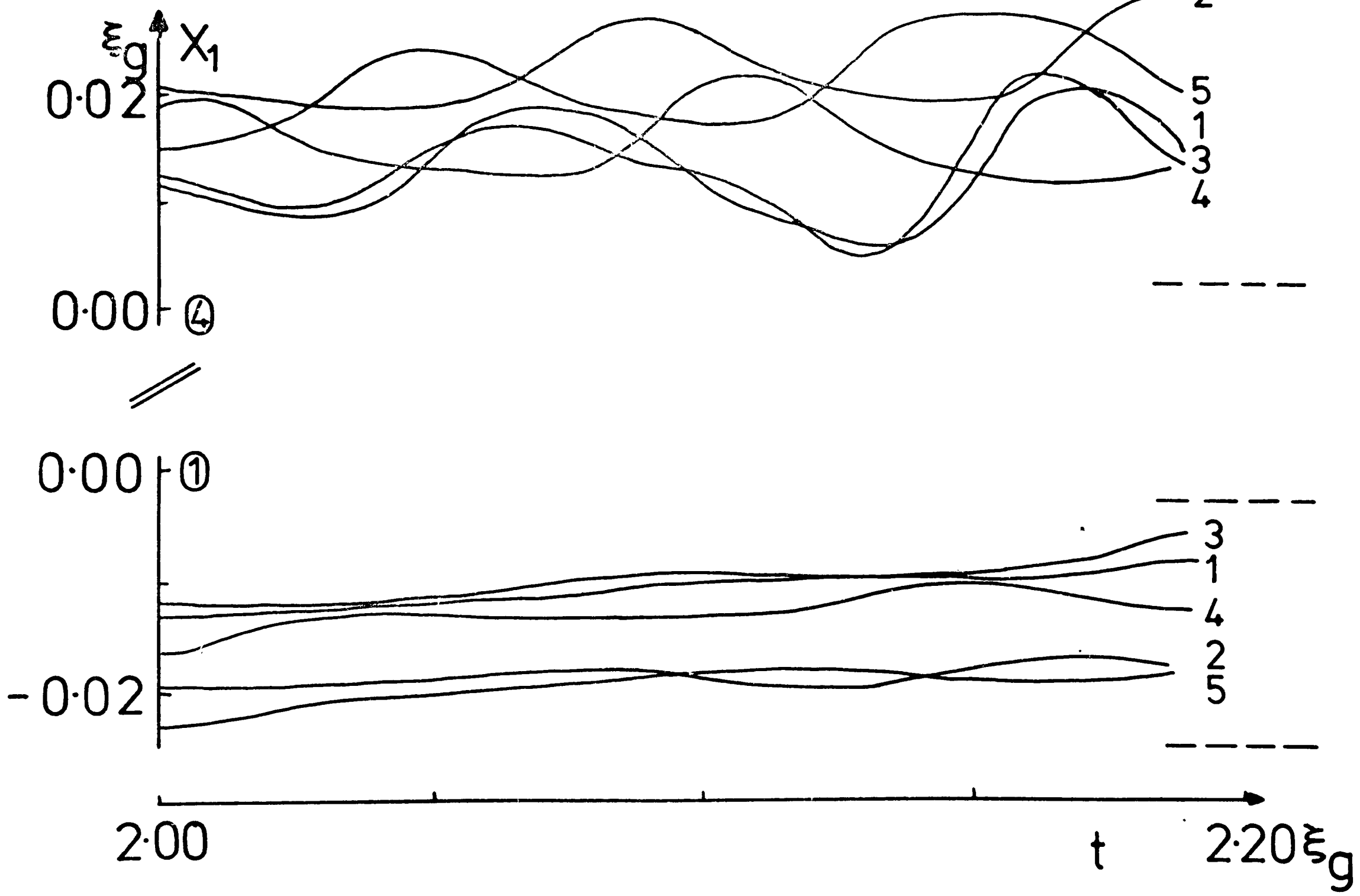
ξ_g
X_1
0·02
0·00
④
0·00
①
-0·02
2·00
t
2·20ξ_g
2
5
1
3
4
3
1
4
2
5

Figure 3.9 The variations in the positions of the outer image peaks with thickness. S dipole, $\underline{g}=20\bar{2}$, various Δ, H and d as marked:-

(1)	Δ = 0.080 ξ_g	H = 0.045 ξ_g	d = 1.00 ξ_g
(2)	0.080	0.090	1.00
(3)	0.112	0.045	1.00
(4)	0.112	0.045	1.05
(5)	0.144	0.2026	1.00

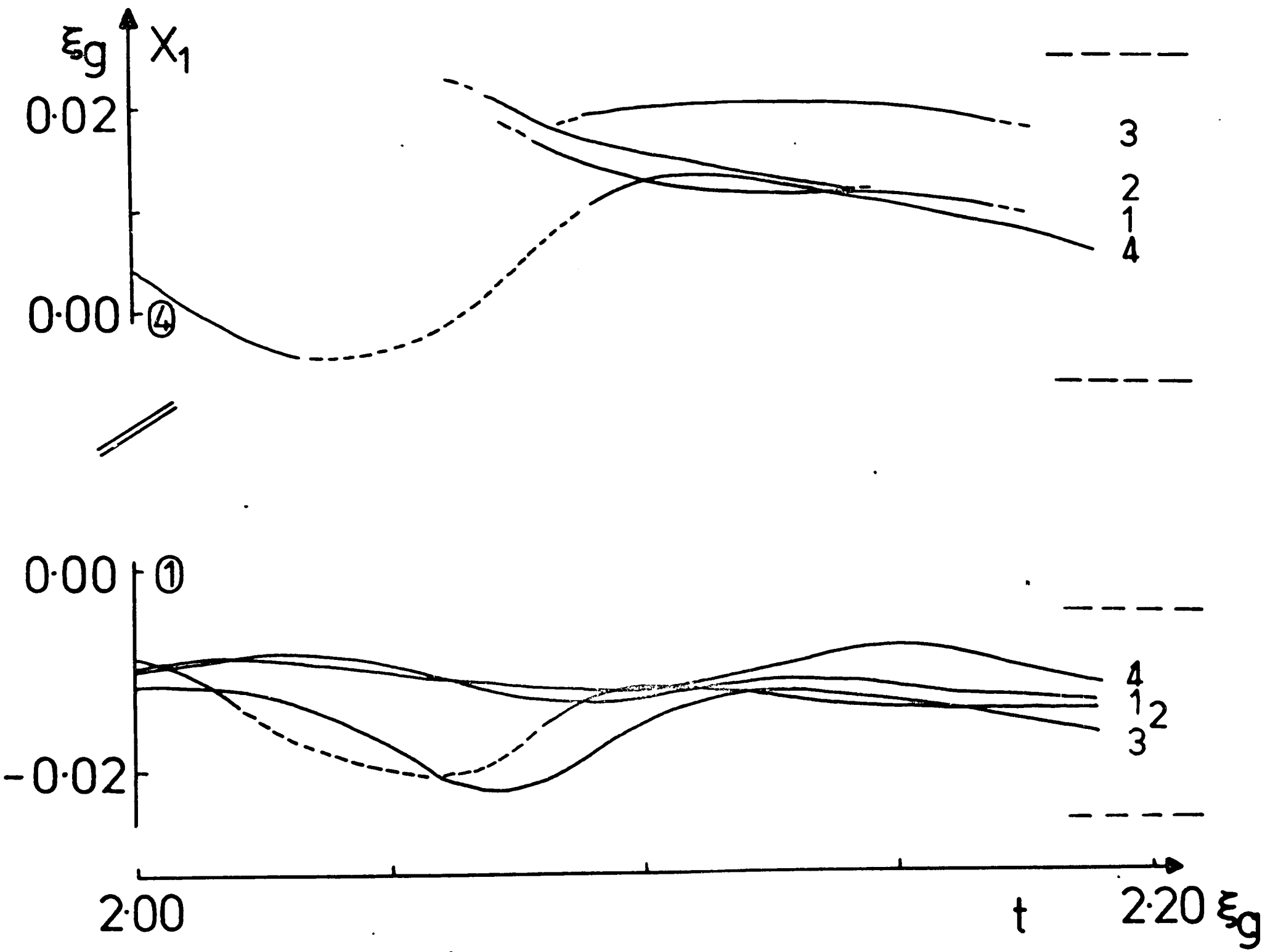
ξ_g
X_1
0·02
0·00
④
3
2
1
4
0·00
①
-0·02
4
1
2
3
2·00
t
2·20 ξ_g

Figure 3.10 The variations in the positions of the image peaks with thickness at the (112) pole. Z dipole, $\underline{g}=11\bar{1}$, $\Delta'=0.2$, $H'=0.1556\,\xi_g$, various d as marked:-

(1) $0.500\,\xi_g$

(2) 1.000

(3) 1.025

(4) 1.050

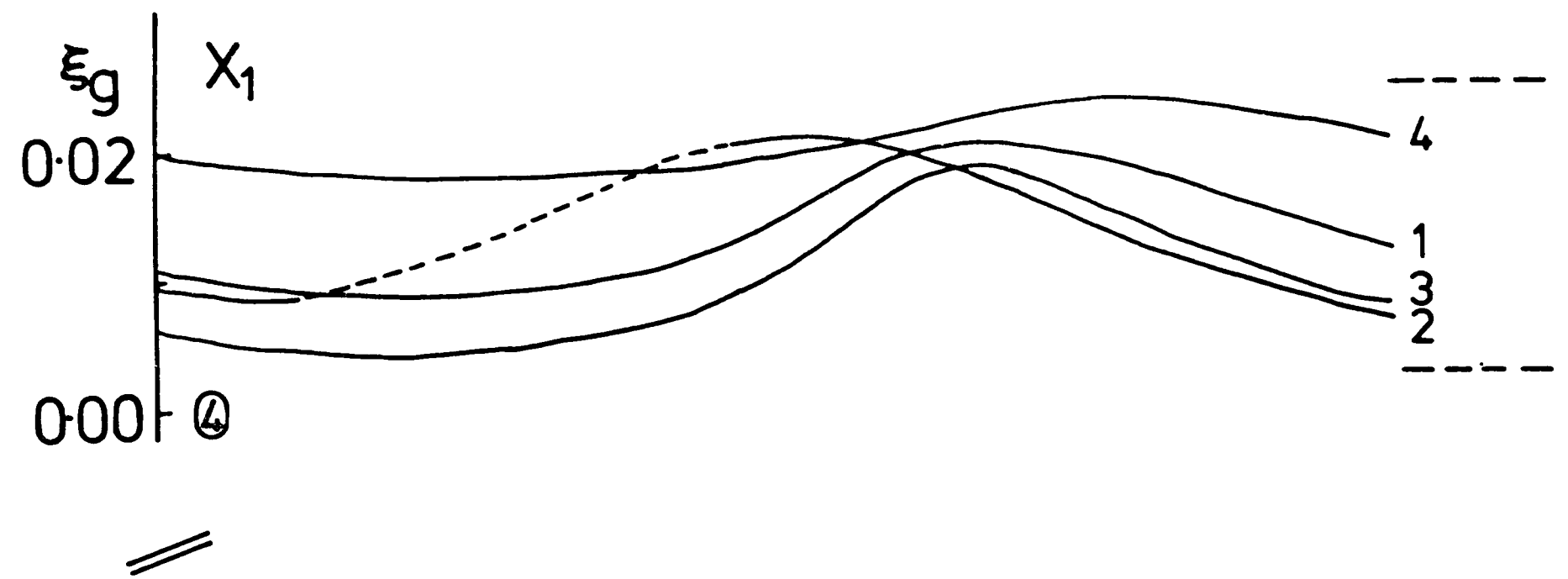
ξg
X1
0·02
0·00
④
4
1
3
2

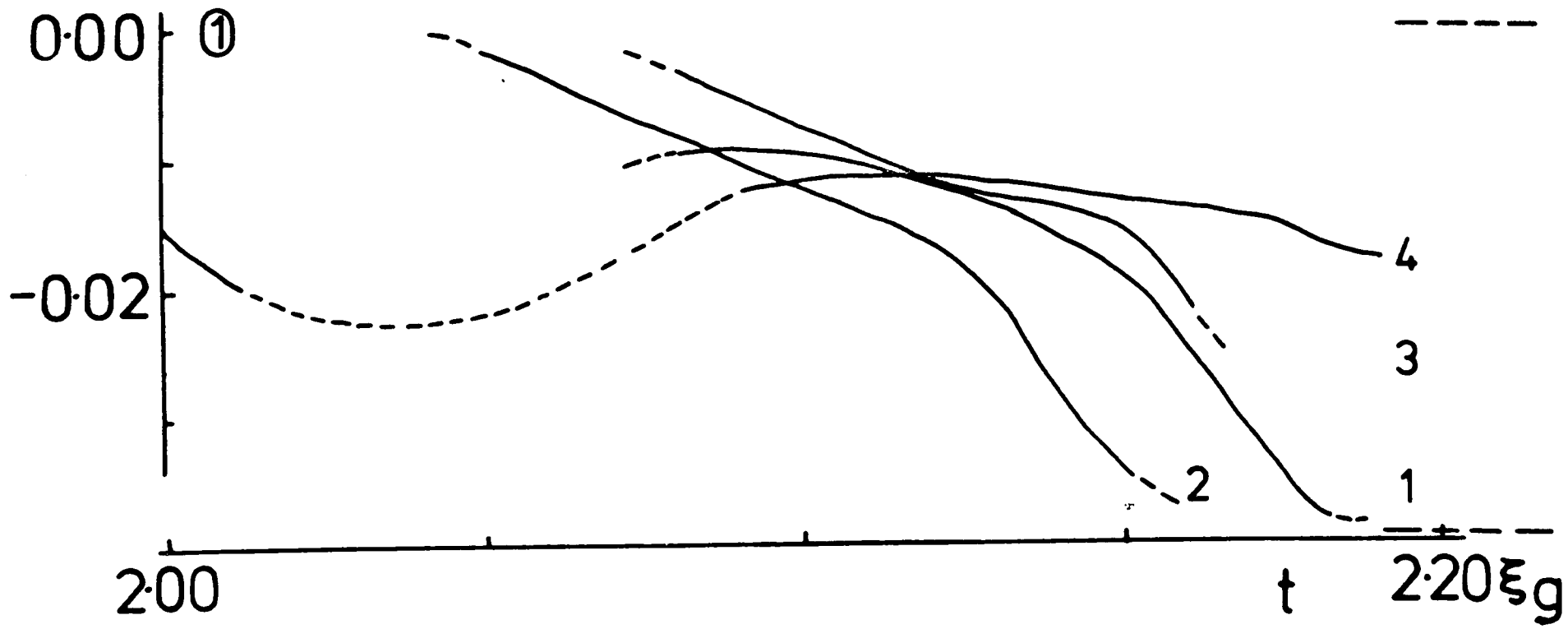
0·00
①
-0·02
4
3
2
1
2·00
t
2·20ξg

Figure 3.11 The variations in the positions of the image peaks with thickness at the (112) pole. S dipole, $\underline{g}=11\bar{1}$, $\Delta'=0.2$, $H'=0.1556\,\xi_g$, various d as marked:-

(1) $0.500\ \xi_g$

(2) 1.000

(3) 1.025

(4) 1.050

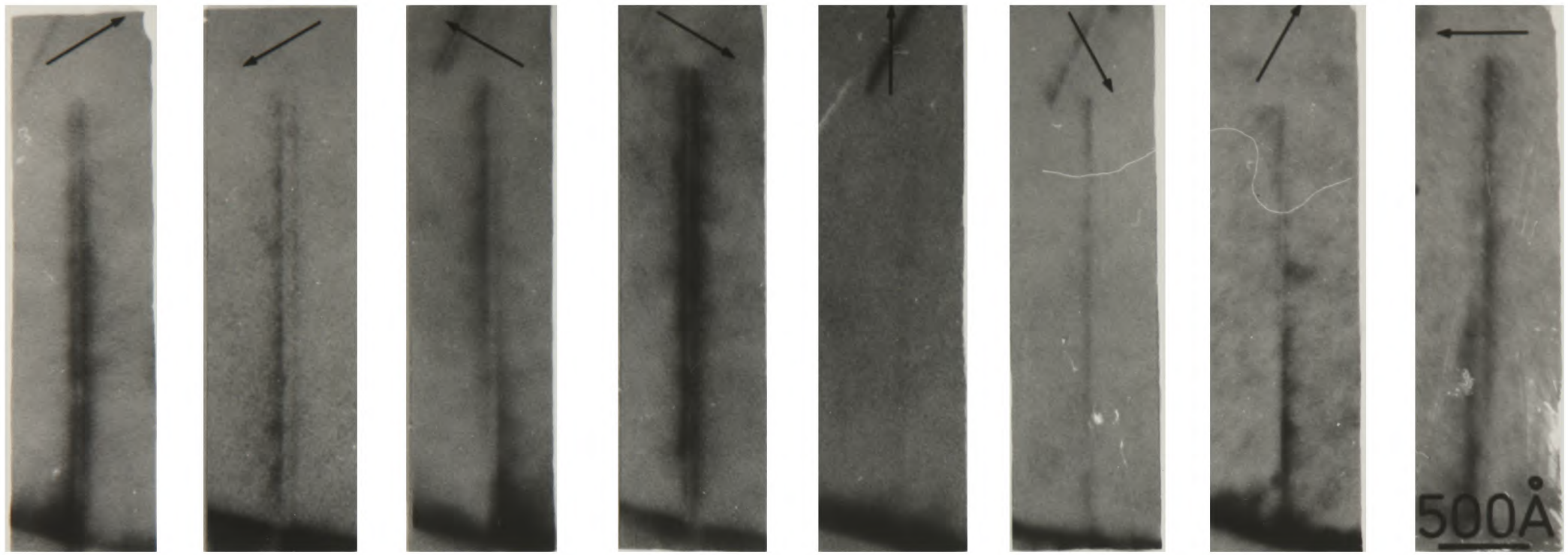
500Å

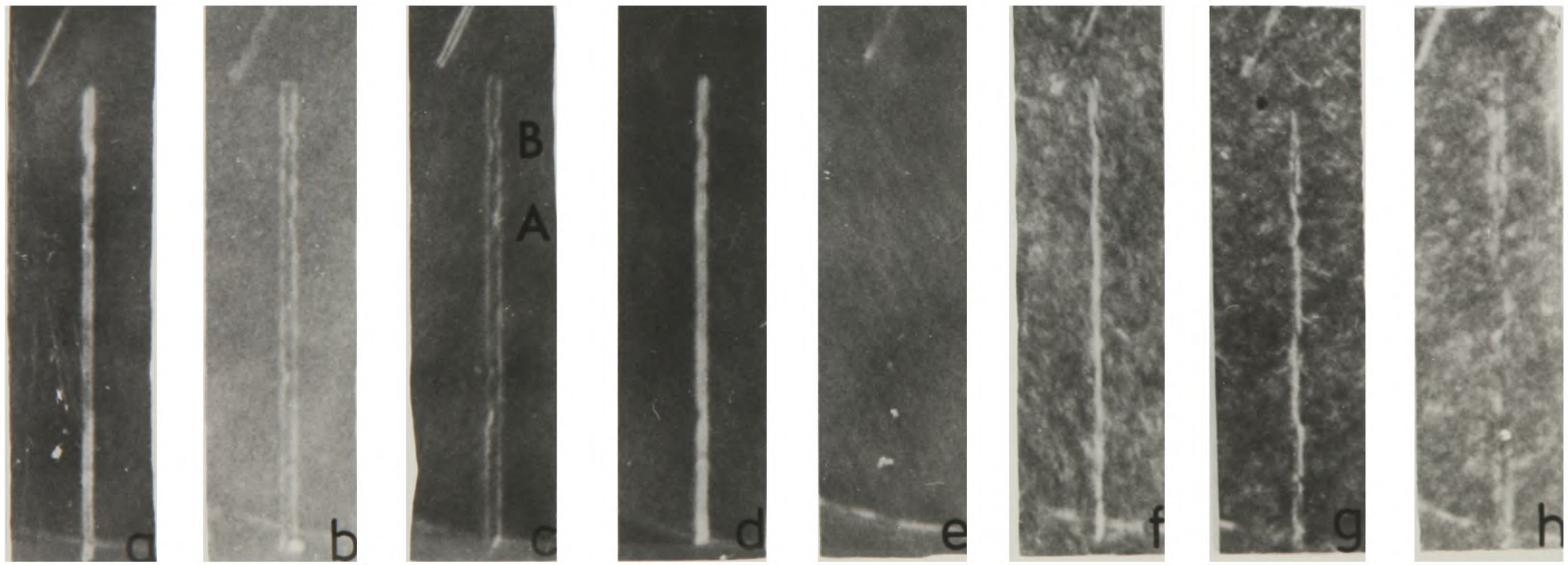
B
A
a
b
c
d
e
f
g
h

Figure 3.12 Experimental images of a faulted dipole in copper taken under different diffraction conditions. The images are displayed in pairs with the lower micrograph that taken under weak-beam dark-field diffraction conditions and the upper that taken under strong-beam bright-field diffraction conditions. The diffraction vector for each pair is shown on the bright-field image and 500 Å scale markers are also shown. The diffraction vectors are: (a) $0\bar{2}2$ (b) $02\bar{2}$ (c) $20\bar{2}$ (d) $\bar{2}02$ (e)$2\bar{2}0$ (f) $\bar{1}11$ (g) $1\bar{1}1$ (h) $11\bar{1}$.

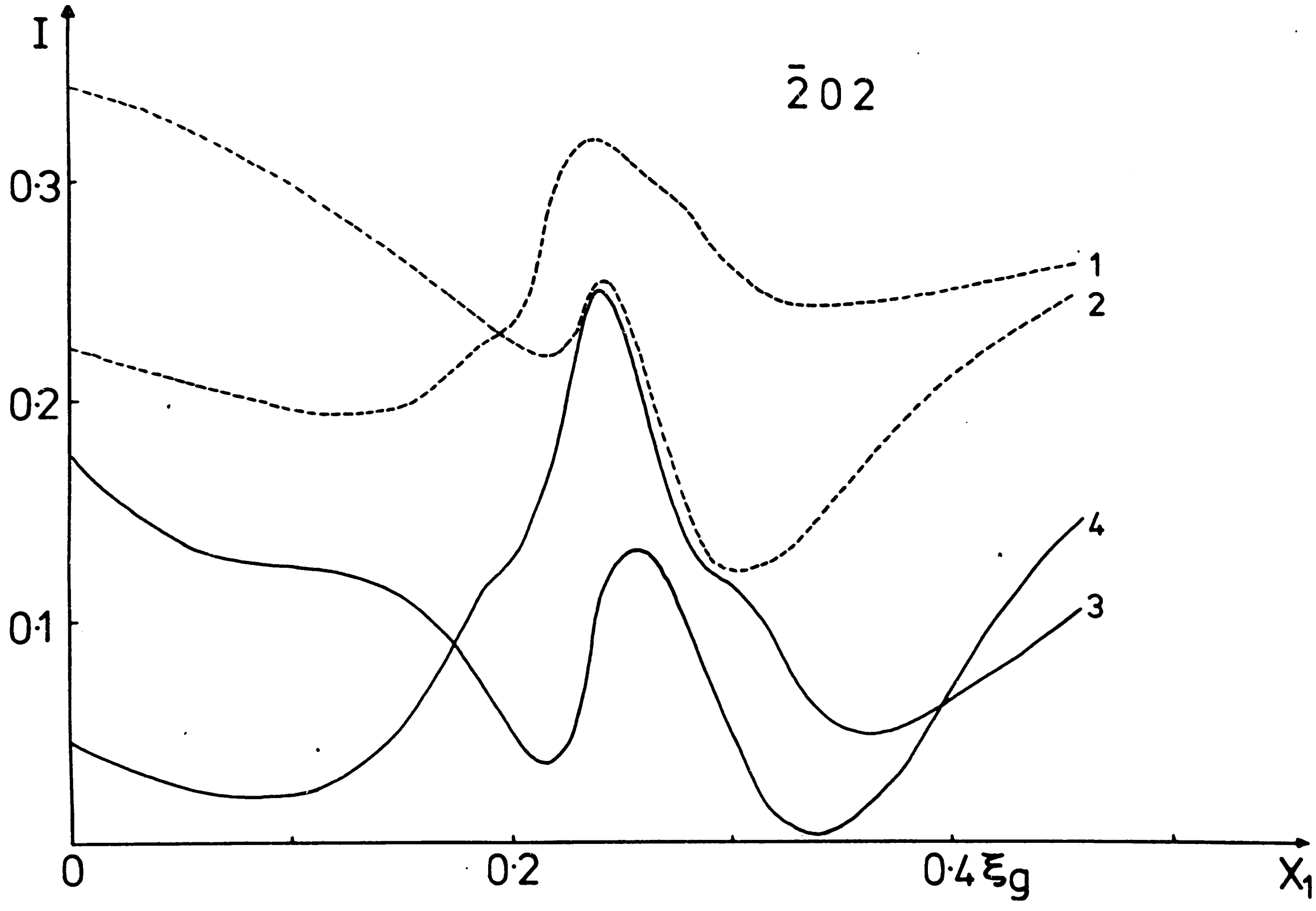
I
0·3
0·2
0·1
0
0·2
0·4 ξg
X1
1
2
3
4
2̄02

Figure 3.13 $\bar{2}02$ computed bright field image profiles of two Z faulted dipoles lying at depth $d=1.0\,\xi_g$ in foils of various thicknesses. The dipoles approximately correspond to the Steeds M-Z transition configurations at $\gamma=40$ and 100 erg cm^{-2}.

(1) γ_{100}, $t=1.92\xi_g$ (2) γ_{100}, $t=1.68\xi_g$ (3) γ_{40}, $t=1.92\xi_g$ (4) γ_{40}, $t=1.68\xi_g$.

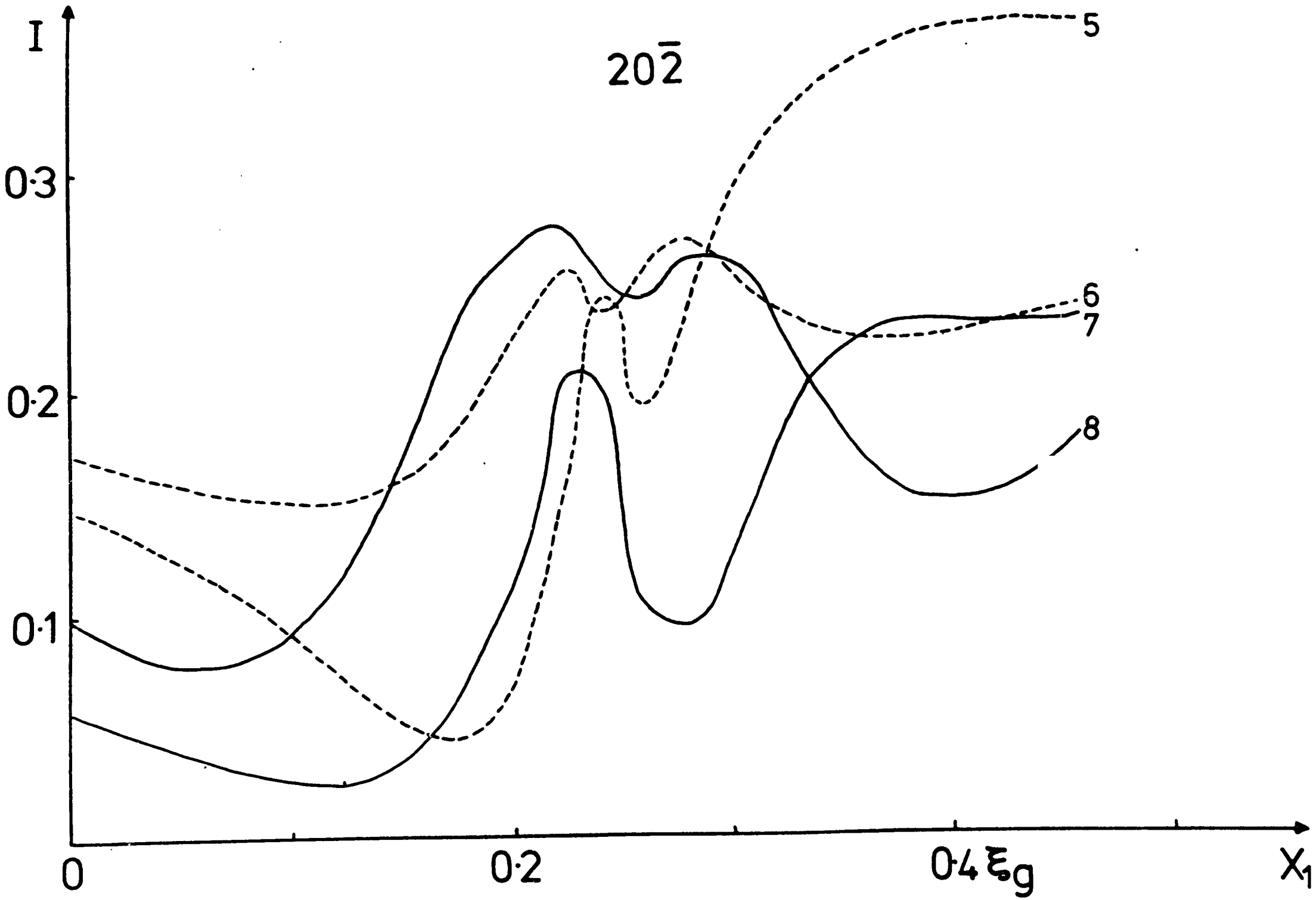
I
0·3
0·2
0·1
0
0·2
0·4 ξg
X1
20$\bar{2}$
5
6
7
8

Figure 3.14 $20\bar{2}$computed bright field image profiles of two Z faulted dipoles lying at depth $d=1.0\,\xi_g$ in foils of various thicknesses. The dipoles approximately correspond to the Steeds M-Z transition configurations at γ=40 and 100 erg cm^{-2}.

(5) γ_{100}, $t=1.56\xi_g$ (6) γ_{100}, $t=2.08\xi_g$ (7) γ_{40}, $t=1.56\xi_g$ (8) γ_{40}, $t=2.08\xi_g$.

Part III

Weak-beam electron microscopy with divergent-beam illumination

Chapter 4

The effect of divergent-beam illumination on weak-beam images

4.1 Introduction

The theories of electron diffraction presented in Chapter 1 represented the incident electrons by a plane wave with a constant wave vector $\underline{k}$. It is important to consider if this assumption of a parallel incident beam, and computed images based upon it, may not be misleading when studying experimental images of specimens illuminated by a divergent beam, since in practice the illumination is always divergent to a certain extent. This chapter discusses the factors controlling the magnitude of the divergence, the measurement of the divergence, and the likely effects of such illumination on weak-beam images. Chapter 5 presents calculations of weak-beam images from dislocations (undissociated and dissociated) in pure copper assuming a divergent beam. Chapter 6 describes experimental observations of interstitial Frank loops in Cu - Al alloys, and it is shown that the effect of the divergent beam is an essential factor in understanding the images.

4.2 Divergent-beam illumincation in the electron microscope

4.2.1 The origin of the divergent beam

In an electron microscope with two condenser lenses, the first lens forms a demagnified image of the beam crossover which is then projected on to the specimen by the second lens. The purpose of this arrangement is to reduce the area of the specimen being illuminated, which helps to prevent contamination and charging problems. The relation between the divergence of the beam at the specimen and the strength of the second condenser lens follows from simple geometry and the application of the formula M = v/u (see e.g. Grivet (1965) p.453). If we define

d = size of crossover image formed by C_1

p = distance from crossover image to specimen

$(1 - k)p$ = distance from C_2 to specimen

v = C_2 image distance

α = angular divergence at specimen (see fig. 4.1(a))

then
$$\alpha = \left(\frac{v}{kp}\right) d \cdot \frac{1}{p(1-k) - v} = \frac{\alpha_o}{k(1-k)p \cdot \frac{1}{v} - k} \qquad (4.1)$$

where α_o is the divergence which would result if C_2 were absent. It appears that if the strength of C_2 were such that $v = (1 - k)p$, then $\alpha \to \infty$. However, the C_2 aperture of diameter 2R limits the maximum value of α to

$$\alpha_{max} = \frac{2R}{(1 - k)p} \qquad (4.2)$$

The curve of α against 1/v resulting from (4.1) and (4.2) is plotted in fig. 4.1(b). In standard texts on optics (e.g. Longhurst 1973 p.450) it is shown that in a given optical system in which the transmission factor is unity and the Abbé sine relation is obeyed, the ratio of current density to α^2 is a constant. Therefore in weak-beam work, where one instinctively adjusts C_2 for maximum intensity, most experiments will be performed with the divergence α_{max} given by (4.2). The computation of divergent-beam images requires knowledge of the distribution function $I(\underline{k})$, which is defined such that $I(\underline{k})\, d\underline{k} = I(\underline{k})\, dk_x\, dk_y$ is the probability that an incident electron has x and y components of the wave vector in the range k_x , $k_x + dk_x$ and k_y , $k_y + dk_y$. It is convenient to normalize this function so that

$$\int I(\underline{k}) d\underline{k} = 1 \qquad (4.3)$$

The measurement of this function in a practical case is described in the next section.

4.2.2 The intensity distribution in the divergent beam

The function $I(\underline{k})$ was determined by recording a plate with the intermediate lens adjusted to image the back focal plane of the objective lens on the final screen. No specimen was present, but otherwise the microscope (a JEM 100B operating at 100kV) was set to reproduce the conditions usual in weak-beam experimentation, i.e. with α given by α_{max} . The purpose of this was to obtain an estimate of $I(\underline{k})$ which could usefully be applied in calculating images to compare with the author's experimental micrographs. With the shortest possible exposure, the density of the recorded spot was very great, but this problem was alleviated by using slower plates (Ilford EM5) and the largest available camera length. The angular divergence α_{max} determined by the C_2 aperture was measured by

comparing the size of the spot with the diffraction pattern from a specimen of known lattice constant and found to be

$$\alpha_{max} \sim 2.5.10^{-3} \text{ radians} \tag{4.4}$$

The variation in intensity within the spot was measured by a Joyce-Loebl microdensitometer. This stage requires a consideration of the response of photographic plates to electrons, which has been reviewed by Valentine (1966). The plate 'emulsion' is a suspension of approximately spherical crystals of a silver halide (usually Ag Br) , $\sim 0.1\mu$ to 1μ , in gelatin. In the electron microscope, only one electron is required to form tiny clusters of silver atoms in a crystal (the latent image). The developer can, given time, reduce all the crystals to grains of metallic silver; however, the silver atoms in the affected crystals act as catalysts and cause these to be rapidly converted. The microdensitometer gives a linear measurement of the optical density D defined by

$$D = \log_{10}\left(\frac{1}{T}\right) \tag{4.5}$$

where T is the fraction of incident light transmitted by the plate. The fraction F of all crystals hit at least once is given by Poisson's Law as

$$F = 1 - \exp(-EA) \tag{4.6}$$

where A is the mean cross-sectional area of a crystal

E is the number of electrons per unit area(exposure)

The relation between T and F is then

$$\ln\left(\frac{1}{T}\right) = A'FN \tag{4.7}$$

where A' is the mean opaque area of a developed grain

Combining (4.5), (4.6) and (4.7) gives

$$D = D_s(1 - \exp(-EA)) \tag{4.8}$$

where $D_s = \frac{A'N}{2.3}$ is the saturation density.

For small values of E, (4.8) reduces to the linear law $D = D_s AE$. In any one exposed plate of the beam spot, the exposure E at a particular point corresponding to the wave vector $\underline{k}$ will be directly proportional to $I(\underline{k})$.

Some care is needed when applying (4.8) to very high values of D, since the resulting density is then sensitive to the exact development conditions. For this reason a calibration set of plates was exposed and then developed in the same rack as the test plate to ensure uniformity of development. Initially the denser plates displayed an asymmetry whereby the edge nearest the bottom of the tank was lighter than that near the top. This problem was satisfactorily overcome by repeating the experiment and developing in a tank with an automatic 'nitrogen-burst' agitation facility. The result is displayed in fig. 4.2. The curve is of the form predicted theoretically in (4.8). The density marked D_M corresponds to the maximum measured on the beam spot plate. Although well into the non-linear region, the existence of densities much greater than this shows that no problem was encountered with saturation.

Previous calculations of divergent-beam images have tended to assume a Gaussian form for $I(\underline{k})$ (Lynch and O'Keefe 1972; Howie, Krivanek and Rudee 1973; Melander and Sandström 1974), but when the beam crossover image is focussed on the specimen plane a top-hat function is more reasonable. This is confirmed by the microdensitometer trace which was constant at D_M for over 90% of the spot width. It was therefore decided to represent $I(\underline{k})$ at the mean value of k_y as a constant over the whole range of k_x. Consequently, references to a specific divergence angle will henceforth imply an $I(\underline{k})$ distribution of this form. Reasonable agreement should be obtained between images computed in this manner and those using other forms of the function with equivalent half-widths.

4.3 The calculation of divergent-beam images

If $\phi_g(\underline{k},z)$ is the amplitude in beam g in a column at depth z calculated assuming a parallel incident beam of wave vector $\underline{k}$, then the resultant intensity due to a divergent beam is

$$|\phi_g(\alpha,z)|^2 = \iint |\phi_g(\underline{k},z)|^2 \, I(\underline{k}) \, dk_x \, dk_y \qquad (4.9)$$

The intensities, and not the amplitudes, have been superimposed in (4.9) since the source is effectively incoherent; any two electrons with different wave vectors $\underline{k}$ cannot interfere with each other (Lenz 1965). This method of calculating divergent-beam images has been proposed for stacking faults (Whelan and Hirsch 1957) and dislocations (Hirsch, Howie and Whelan 1960). It has been applied to images of lattice fringes (Lynch and O'Keefe 1972), amorphous materials (Howie, Krivanek and Rudee 1973), and to weak-beam images of dislocations (Holmes, Cockayne and Ray 1974 ; Melander and Sandström 1974). In practice the integral of (4.9) may be approximated by a sum over a finite number of calculations for different k_x , where the x axis is along the line of $\underline{g}$ ($\phi_g(\underline{k},z)$ is independent of k_y). Five to ten terms in this summation is probably a reasonable compromise between the requirements of accuracy and time of computation. Adding the results of several calculations in this manner is equivalent to assuming that the beam spot is rectangular; naturally it should be a circle, and comparison of the half-widths of the two cases shows that to simulate the effect of a round spot of divergence α , the square spot calculations should cover a range of 0.87α .

4.4 The effect of divergent-beam illumination

The intensity and position of a weak-beam peak vary as a function of foil thickness, defect depth, and deviation parameter s. The intensity oscillations have a periodicity with foil thickness and defect depth given by the effective extinction distance, (1.42). Examples of the oscillations have been seen in figs. 3.6 to 3.11. If we now consider the illumination to be divergent, there is a spread in the value of s given by

$$\Delta s = g\alpha \qquad (4.10)$$

and the image profile may be calculated from (4.9). Such an averaging process should reduce the effect of depth and thickness variations in the image. The spread in s values corresponds to a spread in effective extinction distances, so that a defect may be considered to lie at a range

of 'effective depths' below the surface. For a depth d, and a range of effective extinction distances $\xi_g^{w'} \longrightarrow \xi_g^{w}$, the range of effective depths will be greater than half a period if

$$d\left(\frac{1}{\xi_g^{w'}} - \frac{1}{\xi_g^{w}}\right) \geqslant \tfrac{1}{2}$$

i.e.
$$d \geqslant \tfrac{1}{2}\left(\frac{1}{\Delta s}\right) \qquad (4.11)$$

We might expect depth oscillations to be greatly reduced if (4.11) is satisfied. This argument was first proposed by Jenkins (1973). For a $\{220\}$ reflection in copper, and using α_{max} from (4.4), (4.10) and (4.11) give

$$d \geqslant 250 \text{ Å} \qquad (4.12)$$

An equivalent result can be obtained from the kinematical theory amplitude-phase diagram, fig. 1.5(b). The extreme values of s correspond to two separate diagrams, the circles of which have different radii and whose centres are slightly displaced. Considering the initial circles, the diagrams unwind significantly from them at points corresponding to the same depth, d_1. Then the starting points on these circles will be displaced from one another by at least half a mean revolution if

$$2\pi d_1(\Delta s) \geqslant \pi \qquad (4.13)$$

The above analysis will only apply if the dislocation is at a depth greater than d_1; $\therefore\ d \geqslant d_1$, or, from (4.13),

$$d \geqslant \tfrac{1}{2}\left(\frac{1}{\Delta s}\right) \qquad (4.14)$$

which is identical to (4.11). The interesting point here is that the same argument clearly applies when considering the distance of the defect from the bottom of the foil. This is not so easy to see on the method of Jenkins. The kinematical theory approach suggests that both thickness and depth oscillations are averaged out as long as the defect does not approach either surface nearer than d, (4.14).

The averaging effect should also reduce the oscillations of the peak position, and slightly increase the peak half-width. However, the

spread in s considered so far is only sufficient to remove oscillations with the periodicity of the effective extinstion distance. Saldin (unpublished, reported in Cockayne 1973) has shown that in many-beam computations of weak-beam peak positions, oscillations with a periodicity much greater than ξ_g^w may occur, corresponding to beating between Bloch waves on other branches of the dispersion surface. In such cases a much larger value of Δs would be needed to remove all variation in peak position, although the smaller periodicity oscillations should be effectively damped.

4.5 The importance of the divergent beam effect

Section 4.4 argued that the value of beam divergence normally used in weak-beam microscopy is sufficient to effectively dampen intensity oscillations and peak position variation with depth and thickness, for dislocations a certain critical distance from the foil surfaces. An example of the removal of intensity oscillations by focussing the beam is given in fig. 4.3. Fig.4.3(a) is a conventional weak-beam image of a dissociated dislocation in silicon using a fully divergent beam, and an exposure time of 16 secs. Fig. 4.3(b) was taken with an almost parallel beam, obtained by reducing the strength of C_2 (see fig. 4.1(b)). The exposure time was 10 mins. Intensity oscillations are much more apparent along the length of the dislocation, and the background thickness fringes are now visible as well. It is clear that in normal weak-beam imaging these effects are suppressed.

In many cases this is a beneficial result. For example, Chapter 6 shows that in the computation of images of large Frank loops in Cu-Al alloys, the divergent beam effect alters the character of the images significantly, and greatly simplifies the interpretation of experimental micrographs. Again, the calculations of Häussermann, Katerbau, Rühle and Wilkens (1973) for images of small ($\lesssim 50$ Å) point-defect clusters suggested that the image geometry and intensity were greatly influenced by foil thickness and defect depth; in some cases the image was invisible. They concluded

that this could cause errors in the weak-beam determination of defect numbers and size-density counts. However, the experimental results of Jenkins (1973) in heavy-ion irradiated copper indicated that the appearance of very small defects did not change significantly with a different value of s. Further calculations including a finite beam divergence may show that the images of such defects not close to the surfaces are relatively insensitive to s, depth and thickness.

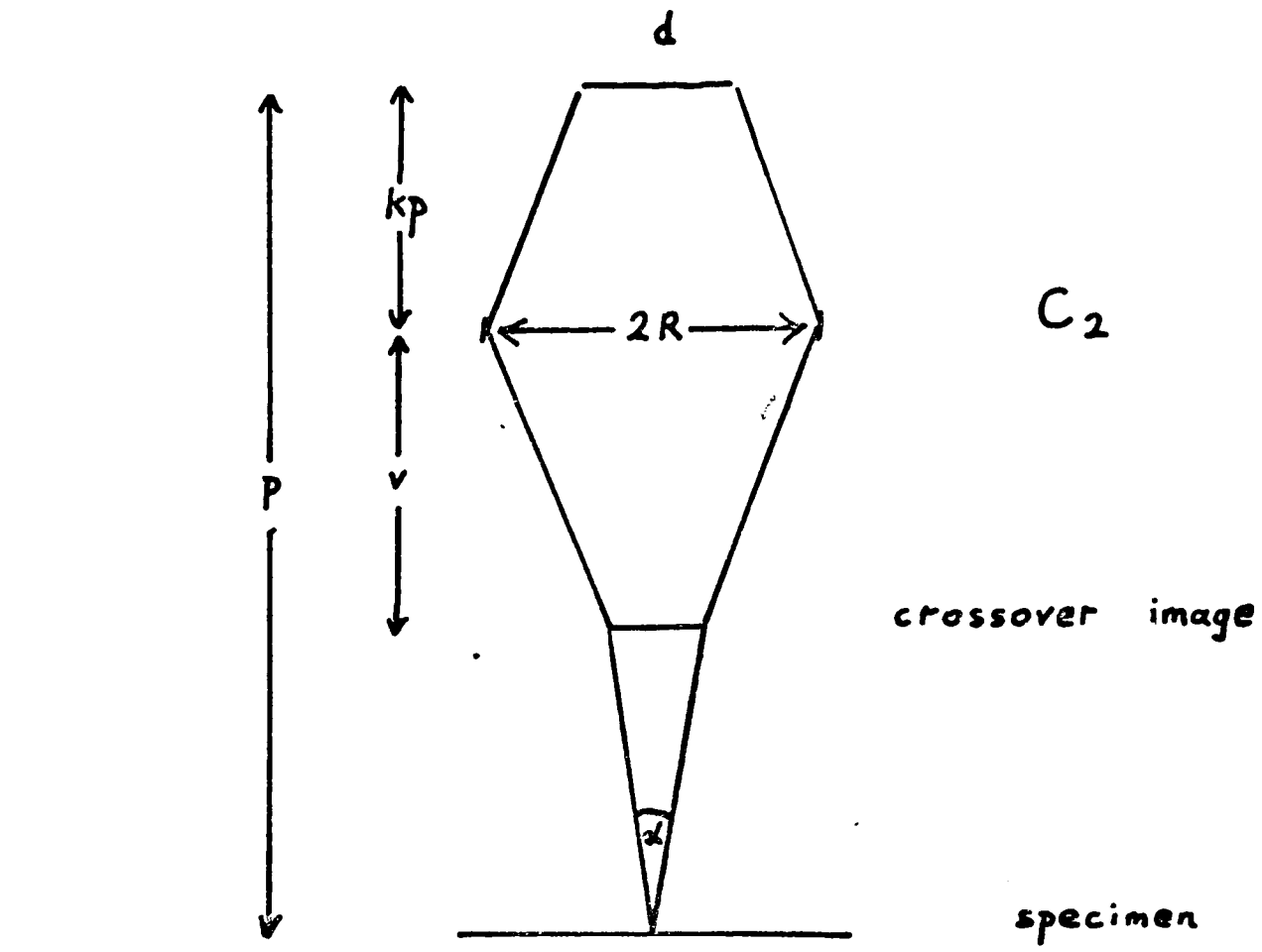
d
kp
2R
v
P
C2
crossover image
α
specimen

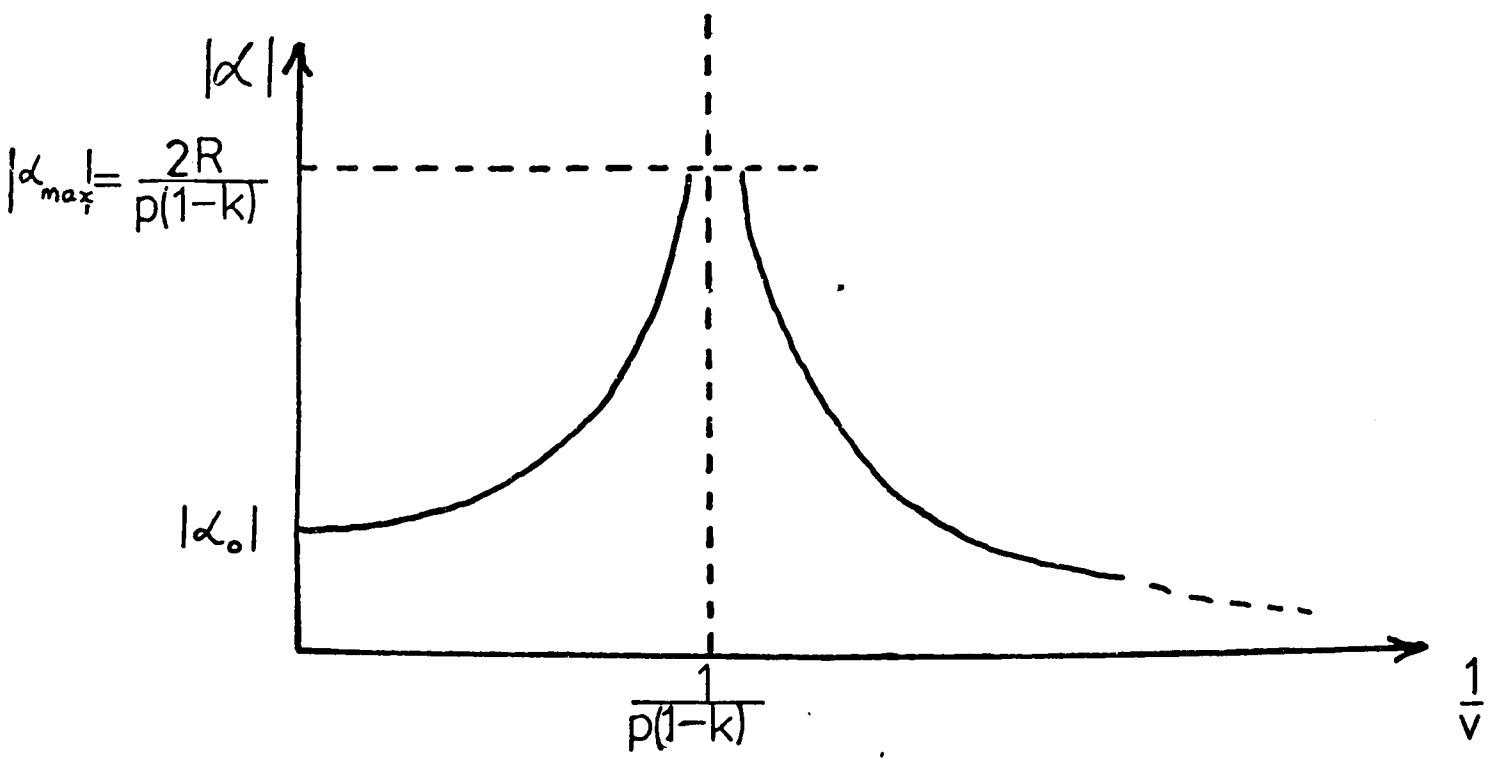
|α|
|α_max| = 2R / p(1−k)
|α_o|
1 / p(1−k)
1/v

Figure 4.1(a) Specimen illumination with divergence α.

Figure 4.1(b) The variation of α with the strength of the second condenser lens.

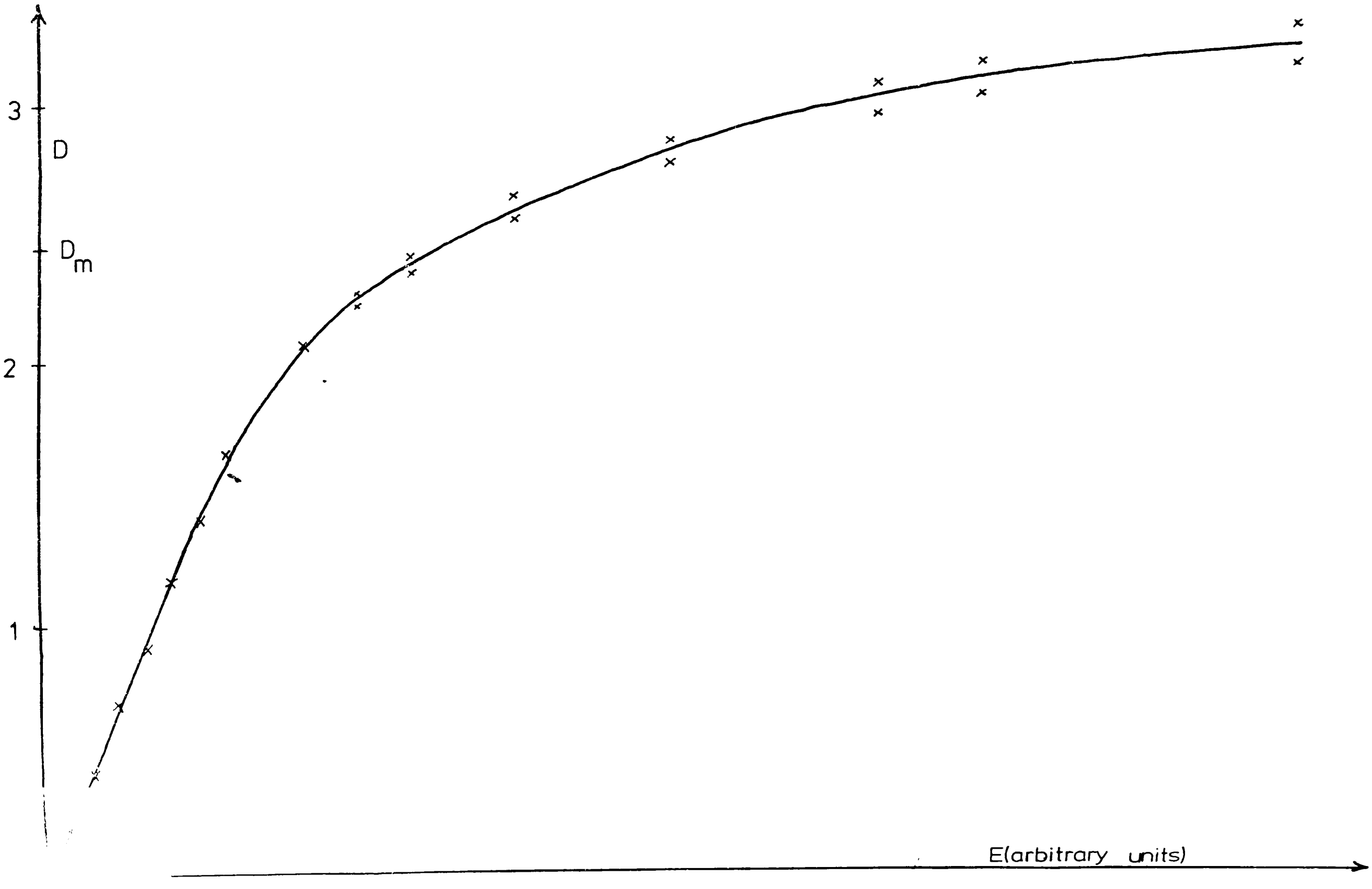
3
D
D_m
2
1
E(arbitrary units)

Figure 4.2 Calibration curve of optical density D against exposure E (arbitrary units) for Ilford EM5 plates.

(a)

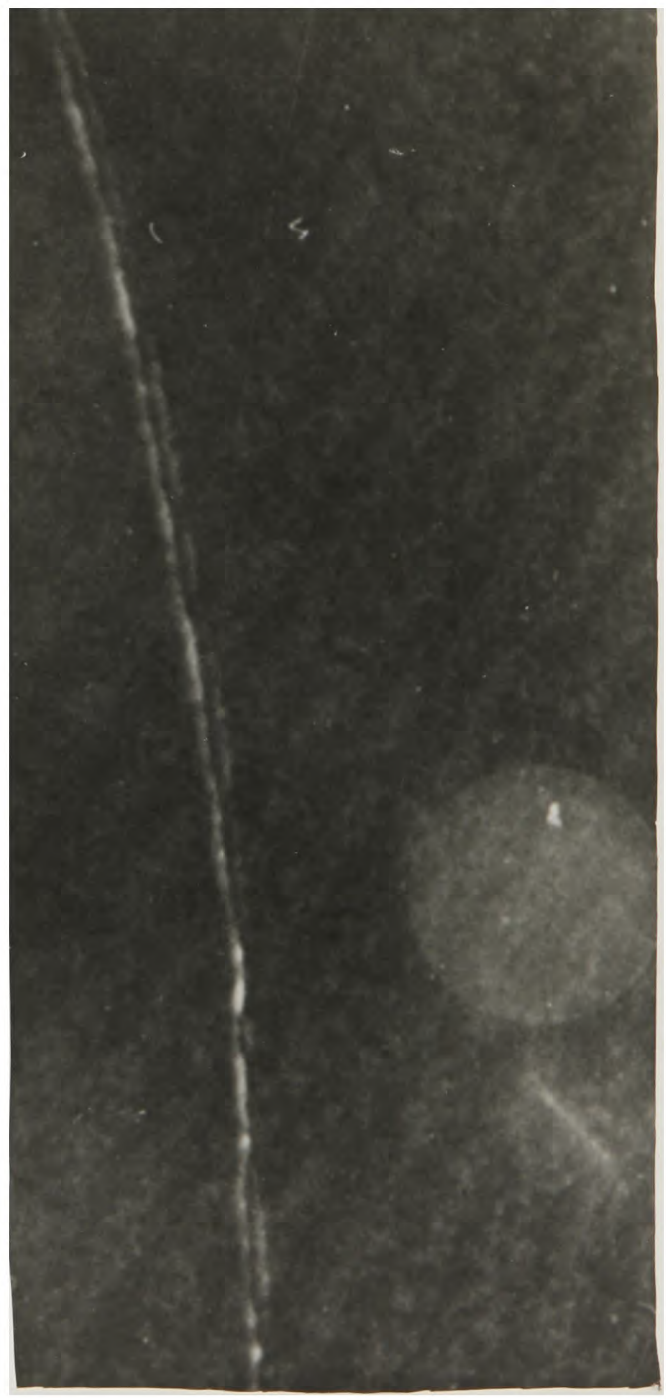

(b)

Figure 4.3 The smoothing of intensity oscillations by the divergent-beam effect for a dislocation in silicon.
(a) fully-divergent beam, exposure time 16 secs.
(b) 'parallel' beam, exposure time 10 mins.

Chapter 5

Weak-beam images of single dislocations using divergent illumination

5.1 Introduction

In Chapter 4 it was shown, from an argument based on the kinemtatical theory amplitude-phase diagram, that the images of defects formed from a divergent beam of incident electrons should not display large depth and thickness oscillation effects if the defect is greater than a certain critical distance from either foil surface, the exact value of the distance depending on the size of the divergence. Five-beam images, computed as outlined in section 4.3, are presented in this chapter to demonstrate the validity of that hypothesis. Both undissociated and dissociated dislocations in the edge and screw orientations have been considered and the calculations used the various parameters for pure copper described in section 3.3.1. Three values of beam divergence have been used as follows:-

(i) Zero, at a value of the deviation parameter $s = 2.5.10^{-2}$ Å^{-1}, hereafter called the parallel beam.

(ii) $1.1.10^{-3}$ radians, hereafter called the semi-divergent beam.

(iii) $2.2.10^{-3}$ radians, hereafter called the fully-divergent beam.

In cases (ii) and (iii) the range in s values was symmetrical about the parallel-beam value of $s = 2.5.10^{-2}$ Å^{-1}. When due allowance has been made for the factor of 0.87 relating the effects of a square and round beam spot (as discussed in section 4.3), the fully-divergent beam case approximately corresponds to the experimentally determined value of $\alpha_{max} = 2.5.10^{-3}$ radians (4.4).

The chapter concludes with an analysis based on these computations of the author's experimental observations of dissociated dislocations in copper, and a discussion on the determination of stacking-fault energies by this approach.

5.2 Calculated images of undissociated dislocations

5.2.1 The screw dislocation

For these computations the dislocation line was taken along

$[\bar{1}10]$, the upward foil normal was $[111]$, the Burgers vector was $\frac{a}{2}[\bar{1}10]$ and the reflection used was $\bar{2}20$, so that $\underline{g}.\underline{b} = 2$. The dislocation was placed at two different depths in the foil, d = 1.00 and 1.05 ξ_g , and results obtained for a range of thicknesses t = 1.00 to 2.00 ξ_g (ξ_g = 418 Å). The image peak intensity is plotted against thickness for the two depths in figs. 5.1(a) and (b). The three curves in each figure correspond to the three values of beam divergence used. Because of the equal weighting procedure used in the computations when adding the results for different values of s , the final images represent the experimental case of having the second condenser lens fully focussed and varying the size of the second condenser aperture. The relative intensities in the three curves are thus misleading since in the fully-divergent beam case far more electrons contribute to the image, and so (for example) the fully-divergent images represented in fig. 5.1(b) should always be brighter than the other two images. However, the important parameter affecting the visibility of any defect whose image displays regular intensity oscillations of this type is the ratio of the spread in intensity to the average intensity, $\frac{\Delta I}{I_{av}}$. It is the increase in this which causes the dislocation image in fig. 4.3(b) to appear more dotted than in fig. 4.3(a). This parameter may be most conveniently compared if the images are calculated as outlined above and the results plotted as in figs. 5.1(a) and (b).

It can be seen that in all cases the intensity oscillations have a periodicity with thickness of the effective extinction distance, $\sim 0.1\ \xi_g$. These oscillations are superimposed on another variation with a much larger wavelength, $\sim 0.7\ \xi_g$, an effect which has been noted previously by Saldin in calculations of weak-beam image peak positions (unpublished, reported in Cockayne 1973). As discussed in section 4.4, such large wavelength phenomena are only expected to be damped by a normal value of beam divergence in very thick crystals. The value of the critical distance in the fully-divergent beam case is given by (4.11) as $0.7\ \xi_g$. The

dislocation depths applicable to figs. 5.1(a) and (b) are both greater than this, and so section 4.4 predicts effective damping of both depth and thickness oscillation effects if the foil thickness is more than $\sim 1.7\ \xi_g$ ($0.7\ \xi_g$ below the dislocation). It can be seen that from this thickness onwards the value of $\frac{\Delta I}{I_{av}}$ is rapidly reduced in the fully-divergent beam case.

In the semi-divergent beam case the critical distance is $1.4\ \xi_g$, so the depth of the dislocation does not now satisfy (4.11). This means that depth oscillations can not be effectively damped by the divergent beam effect, but thickness oscillations should be removed if the bottom of the foil is more than $1.4\ \xi_g$ below the dislocation, which means a foil thickness of $\sim 2.4\ \xi_g$ here. Therefore little change in $\frac{\Delta I}{I_{av}}$ is expected for the range of foil thicknesses plotted, and it can be seen in figs. 5.1(a) and (b) that any reduction is much smaller than in the fully-divergent beam calculations.

The effect of varying the dislocation depth may most easily be seen in fig. 5.2(a) where the curves from figs. 5.1(a) and (b) for the parallel and fully-divergent beam cases have been superimposed. Although the comparison of intensities from calculations assuming different values of beam divergence is not meaningful for the reasons given above, one can of course compare different computations which assume the same value of the divergence. Fig. 5.2(a) shows that varying the dislocation depth with a parallel beam has a large effect on the resulting intensities, but with the fully-divergent beam, and thicknesses satisfying (4.11), there is little change in the peak intensities. It is concluded from figs. 5.1 and 5.2(a) that the predictions of Chapter 4 concerning the dependence of the image peak intensity on defect depth and foil thickness when the illuminating beam of electrons has a finite divergence are confirmed by computed images of an undissociated screw dislocation.

It is reasonable to expect that some averaging of the image peak position will also occur with divergent illumination. Fig. 5.2(b) shows the variation of peak position with thickness for both the parallel and fully-divergent beam conditions with the disloaction at the two depths $d = 1.0$ and $1.05\ \xi_g$. The defect is positioned at $X_1 = 0.075\ \xi_g$. The large wavelength oscillation is more in evidence here than in the curves of peak intensity. In the fully-divergent beam calculation for thicknesses $t \geqslant 1.7\ \xi_g$ it can again be seen that the variations are damped and that the deviation of the peak position from the defect is tending to a constant value irrespective of depth and thickness. Dotted boundary lines have been drawn in the manner of Chapter 3 to define the range of expected peak positions with fully-divergent illumination and so derive an average correction factor and error limits. The mean peak position is marked on the X_1 axis by the arrow X_c. This is ~ 12 Å from the position of the dislocation, X_d, and the actual peak position varies about this point by ± 5.5 Å. We therefore obtain for the peak position with fully-divergent illumination at $s = 2.5.10^{-2}$ Å^{-1},

$$X_c = X_d = 12 \pm 5.5 \text{ Å} \qquad (5.1)$$

It can be seen that the random error would have been somewhat larger if the parallel beam calculations had been used. Two approximate criteria for predicting the position of a weak-beam peak were discussed in section 1.5.3 ; X_w from (1.81) (Cockayne, Ray and Whelan 1969), and X_k from the kinematical theory (Hirsch, Howie and Whelan 1960). These give the deviation of the image peak from the dislocation as 12.5 Å and 6.5 Å respectively in the present case. They are marked on the X_1 axis in fig. 5.2(b). It can be seen that the average position X_c derived from the calculations is much nearer to X_w than to X_k.

Although the curve of peak position is tending to a fixed value in fig. 5.2(b), this does not enable the error limits in (5.1) to be reduced when analysing an experimental micrograph unless the dislocation

depth and foil thickness are known reasonably accurately; and unless several different micrographs of the defect of interest were obtained (e.g. stereo pairs), this information is not available. Alternatively, it is possible, in theory, to associate a particular value of $\frac{\Delta I}{I_{av}}$ from figs.5.1 or 5.2(a) with the stabilization of peak position in fig. 5.2(b), but this would be a very difficult procedure in practice. In any case, the precise position of an isolated dislocation is only of limited interest, but these points will become important when considering dissociated dislocations in section 5.3.

5.2.2 The edge dislocation

Similar calculations have been performed for the case of a pure edge dislocation with Burgers vector $\underline{b} = \frac{a}{2}[\bar{1}10]$, line direction $\underline{u} = [11\bar{2}]$, and $\underline{g} = \bar{2}20$. Curves of peak intensity are plotted against foil thickness in figs. 5.3 and 5.4(a), and of the variations in peak position in fig. 5.4(b). The various beam divergences and dislocation depths all have the same values as for the screw dislocation case plotted in figs. 5.1 and 5.2. These curves provide further confirmation of the predictions in Chapter 4 and of (4.11) since in the fully-divergent case $\frac{\Delta I}{I_{av}}$ is effectively damped from $t \sim 1.7\ \xi_g$ onwards. Fig. 5.4(a) again demonstrates the little effect that changing the depth has for foil thicknesses greater than this. In fig. 5.4(b) it can be seen that the oscillations of periodicity $\sim 0.1\ \xi_g$ in the peak position are much less noticeable for the edge dislocation than was the case for the screw and the larger wavelength effect is dominant. However, varying the defect depth generally has a smaller effect on the peak position with the fully-divergent beam, and at the larger thicknesses the positions at the two depths are converging. The dislocation is placed at $X_1 = 0.055\ \xi_g$. The mean image peak position is $X_c = 0.0055\ \xi_g$, or ~ 21 Å from the defect. The approximate criteria for the peak position give $X_k = X_d - 13$ Å and $X_w = X_d - 22$ Å, and these are marked on the X_1

axis. Again the prediction of (1.81), X_w, is much nearer to the calculated mean X_c than is X_k. From these computations we obtain for the edge dislocation

$$X_c = X_d - 21 \pm 5 \text{ Å} \tag{5.2}$$

5.3 Calculated images of dissociated dislocations

5.3.1 Shockley partials in the face-centred cubic lattice

The energy of a dislocation is proportional to the product of the line length and the square of the Burgers vector. In the face-centred cubic lattice an energy reduction is possible if a normal dislocation dissociates into two Shockley partials in the following manner:-

$$\frac{a}{2}[\bar{1}10] \rightarrow \frac{a}{6}[\bar{2}11] + \frac{a}{6}[\bar{1}2\bar{1}] \tag{5.3}$$

The partial dislocations bound a ribbon of stacking fault. Faults can be formed either by removing a plane of atoms to form the intrinsic fault sequence ABCBCAB , or by inserting a plane and forming the extrinsic fault ABCBABC . With Shockley partials these stacking sequences can be created by shearing processes rather than by inserting or removing material. Given a particular orientation of the crystal, line direction and Burgers vectors of the partials, the nature of the fault formed depends on the order of the dislocations, i.e. on which partial is 'on the left'. In the notation of the Thompson tetrahedron (Thompson 1953) we have the rule that for the intrinsic fault the Greek-Roman partial should be on the left when viewed from outside the tetrahedron and looking along the line. The opposite order theoretically results in the stacking sequence ABCCABC , and although it contains the forbidden CC sequence, this order of the partials is often used to represent the extrinsic fault arrangement of two intrinsic faults on two successive planes since the stacking is identical away from the fault plane itself. Therefore if the right hand side of (5.3) represents the position of the partials in an intrinsic fault, the same dislocation with the opposite order of the partials

$$\frac{a}{2}[\bar{1}10] \rightarrow \frac{a}{6}[\bar{1}2\bar{1}] + \frac{a}{6}[\bar{2}11] \tag{5.4}$$

gives the same stacking sequence away from the fault plane as the extrinsic arrangement of the two intrinsic dissociations

$$\frac{a}{2}[000] \rightarrow \frac{a}{6}[11\bar{2}] + \frac{a}{6}[\bar{1}\bar{1}2] \qquad (5.5)$$

$$\text{and} \quad \frac{a}{2}[\bar{1}10] \rightarrow \frac{a}{6}[\bar{2}11] + \frac{a}{6}[\bar{1}2\bar{1}]$$

on adjacent planes. In most practical observations the system of (5.5) would be indistinguishable from that of (5.4), so it is usual to consider only (5.3) and (5.4), calling the latter the extrinsic fault arrangement, although this is not strictly correct. This simplifies matters considerably in calculations, and is only invalid in cases where the dissociation width is not much greater than the plane spacing, or s is so high that the weak-beam image peaks come from regions of the crystal which are very close to the defect cores.

In experimental work it is usually necessary to differentiate between intrinsic and extrinsic faults, and this is possible if the line and sense of each partial Burgers vector is known. For a particular dissociation with Burgers vector $\underline{b}$, one $\pm\underline{g}$ pair of the six $\{220\}$ reflections at the (111) pole is such that $|\underline{g}.\underline{b}| = 2$, and that for each partial $|\underline{g}.\underline{b}_p| = 1$. In the other four reflections $|\underline{g}.\underline{b}| = 1$, and $|\underline{g}.\underline{b}_p| = 1$ for one partial and $|\underline{g}.\underline{b}_p| = 0$ for the other. In all these cases the central stacking fault will be out of contrast since $\underline{g}.\underline{R}$ is an integer. Assuming isotropic elasticity, in the $|\underline{g}.\underline{b}_p| = 0$ cases $\underline{g}.\underline{R}$ for this partial is also zero and therefore only one peak is expected in the $|\underline{g}.\underline{b}| = 1$ images. However, $\underline{g}.\underline{R}$ is not zero in anisotropic elasticity and some weak diffuse contrast is predicted by computation (Stobbs and Sworn 1971), but the $|\underline{g}.\underline{b}_p| = 1$ peak can easily be recognized. Two relatively strong peaks are expected in the $|\underline{g}.\underline{b}| = 2$ cases and these images are normally used when investigating partial separations. However, all three $\pm\{220\}$ images are usually needed if the fault nature is to be determined. This is done in the following manner:-

(i) Assign a positive sense to the dislocation line direction.

(ii) From the diffraction pattern and the microscope rotation calibration draw the $\underline{g}$ vector on the micrograph.

(iii) Obtain the sense of the total Burgers vector by noting the positions of the partial dislocation peaks in the $\pm\underline{g}$ micrographs and the sign of s from the diffraction patterns. This is often the most difficult step because of the uniform background of weak-beam pictures. The peak for either partial occurs on that side of the defect core for which the strain field rotates the lattice planes into the Bragg position.

(iv) From the $|\underline{g}.\underline{b}| = 1$ images determine the line of each partial Burgers vector.

(v) By noting the sense of rotation required to tilt the crystal to another pole the orientation of the Thompson tetrahedron may be deduced. This information together with the line direction and Burgers vectors of the Shockley partials enables the fault to be defined unambiguously.

5.3.2 Dissociated dislocation image symmetry

When imaging a dissociated dislocation whose Burgers vector is such that $|\underline{g}.\underline{b}| = 2$, there are eight possible arrangements of partial Burgers vectors, partial dislocation position, and sign of the $\underline{g}$ vector to consider. Fortunately, in both isotropic and anisotropic elasticity theory (see (2.21) and (2.36)) the strain field is linearly related to the Burgers vector components and so reversing the sign of $\underline{b}$ gives the same $\underline{g}.\underline{R}$ product as reversing the sign of $\underline{g}$. This means that in the general anisotropic case there are four different images to consider. These images are represented symbolically in fig. 5.5(a) where a letter is used on either side of the particular dislocation arrangement to represent a certain value of the $\underline{g}.\underline{R}$ product. The values of the letters are related by $A = -C$, $B = -D$, $E = -G$ and $F = -H$. Isotropic elasticity permits a simplification of this since the Burgers vectors are all in the same plane as $\underline{g}$. This gives the additional relations $E = -B$, $F = -A$ and the result

is shown in fig. 5.5(b). It can be seen that in the general isotropic case there are only two essentially different images, the other two being related to these by reflection about the mid-point of dissociation. In the special case of $\underline{g}.\underline{b}_1 = \underline{g}.\underline{b}_2$, $\underline{g}.\underline{b}_{1e} = \underline{g}.\underline{b}_{2e}$ ($\underline{b}_{ne}$ is the edge component of the Burgers vector of partial dislocation n) i.e. a dissociated screw or edge dislocation, the additional relations E = A and F = B also apply, giving the images of fig. 5.5(c). For the dissociated edge or screw dislocation there is only one possible value of the image peak separation when assuming isotropic elasticity. These conclusions may also be reached from the criterion of (1.81), which predicts for the observed image width Δ_{obs} at a particular partial dissociation Δ

$$\Delta_{obs} = \left[\left(\Delta + \frac{(a - b)}{ab}\right)^2 + \frac{4}{ab}\right]^{\frac{1}{2}} \qquad (5.6)$$

$$\text{where } a = -s_g \Big/ \left(\frac{\underline{g}.}{2\pi}\left(\underline{b}_1 + \frac{\underline{b}_{1e}}{2(1-\nu)}\right)\right)$$

$$\text{and } b = -s_g \Big/ \left(\frac{\underline{g}.}{2\pi}\left(\underline{b}_2 + \frac{\underline{b}_{2e}}{2(1-\nu)}\right)\right)$$

(Cockayne, Ray and Whelan 1969; Cockayne 1970; Cockayne, Jenkins and Ray 1971). Because of the (a - b) term in (5.6) , Δ_{obs} will have two different values depending on the order of the partial dislocations or the sign of $\underline{g}$ except in the special case a = b, exactly as indicated by figs. 5.5(b) and (c). A study of fig. 5.5(b) shows that, in the isotropic approximation, whatever the order of the partial dislocations and sign of the total Burgers vector may be, a dissociated dislocation of a particular character can give rise to either of the two possible image separations by using $\pm\underline{g}$. Therefore only one geometrical arrangement need be considered when computing images and the results can be compared to the experimental micrograph with the correct sign of $\underline{g}$. Clearly it is advantageous to use the images which give the wider separations, and the necessary geometry for this may be deduced from (5.6).

When images are computed using anisotropic elasticity (as is the case for all the images presented in this thesis), this simple matching

procedure is not valid. Fig. 5.5(a) shows that a dissociated dislocation of mixed character gives rise to four different images depending on the order of the partials, the sign of the total Burgers vector and the sign of $\underline{g}$. Some simplification of this state of affairs occurs in the case of the dissociated screw and edge dislocations whose $\underline{g}.\underline{R}$ products are as indicated in figs. 5.5(d) and (e) respectively. Although both these cases can give two essentially different images, there is a significant difference in the symmetries involved. In the screw case, a dislocation which gives the image AB in $+\underline{g}$ will give the image CD in $-\underline{g}$; this is therefore analagous to the mixed character dislocation in the isotropic case where only one set of computations is needed to match the micrograph taken with the correct sign of $\underline{g}$. In the edge case, fig. 5.5(e), reversing the sign of $\underline{g}$ gives essentially the same image; two sets of computations are needed to analyse correctly all possible arrangements of the dissociated edge dislocation.

The degree of importance of these differences in Δ_{obs} will depend on the anisotropy of the material concerned, but is likely to be significant in the case of copper for which (2.11) gives the anisotropy factor A as 3.21. The two values of Δ giving a Δ_{obs} of 30 Å in the case of a 30° dislocation using the isotropic criterion (5.6) are 23 and 29 Å when $s_g = 2.5.10^{-2}$ Å^{-1} . Similar differences could easily arise in the various image widths produced by anisotropic materials; when estimating the stacking-fault energy of copper from the splitting of edge dislocations, an error of 6 Å in the interpretation could change the result from γ = 40 erg cm^{-2} to γ = 48 erg cm^{-2}. Anisotropic displacement fields have been used in image computations of dissociated dislocations in copper by Stobbs and Sworn (1971) but it is not obvious from their paper that the possibility of different image widths as predicted by figs. 5.5(a), (d) and (e) was considered. For this reason it was thought desirable to check the analysis using the author's own experimental observations and the computed images allowing for the divergent beam effect and assuming anisotropic elasticity to be presented in sections

5.3.3 and 5.3.4. Calculations of this sort are very expensive in terms of computer time and so far it has only been possible to consider one arrangement of the partial dislocations and two separations for both the edge and screw orientations. Because of fig. 5.5(e) this means that some of the micrographs of near-edge orientation dislocations could not be included in the analysis. However, as a large number of dislocations of this character were observed, this was not felt to be a problem.

The properties of images of single dislocations assuming anisotropy may also be deduced from figs. 5.5(a), (d) and (e) by merging the two partials and equating $\underline{g}.\underline{R}$ products for geometries which are now equivalent. It can then be seen from fig. 5.5(d) that reversing $\underline{g}$ for the two possible screw dislocations still gives a different image, whereas fig. 5.5(e) shows that all images of undissociated edge dislocations are essentially identical. Therefore the results for the screw dislocation presented in section 5.2.1 only apply to the geometry described there with $\underline{g} = \bar{2}20$; changing $\underline{g}$ to $2\bar{2}0$ or reversing the Burgers vector would alter (5.1).

5.3.3 The screw dislocation

The calculations for dissociated screw dislocations assumed the upward foil normal to be $[111]$, the line direction $[\bar{1}10]$, the Burgers vector of partial 1 (on the left when looking from above the foil and along the line) was $\frac{a}{6}[\bar{2}11]$, that of partial 2 was $\frac{a}{6}[\bar{1}2\bar{1}]$, and the reflection used was $\bar{2}20$. The dislocations were again placed at depths d = 1.00 or 1.05 ξ_g in a foil of thickness 1.0 to 2.0 ξ_g , and computations performed for the parallel and fully-divergent beam cases. The results for a dissociation of 10.5 Å are shown in fig. 5.6 where the two peak positions are plotted against foil thickness; the dislocation positions are marked on the X_1 axis. It has been found in the vast majority of computations that the image peak which lies between the two partials is weaker than the other; an example of this can be seen in fig. 2 of Cockayne (1972). (One of the few cases where this is not so was the profile given in Cockayne, Ray and Whelan (1969)). Stobbs and Sworn (1971) found in their work that this weaker peak was

invisible for a partial separation of 10 Å . It is therefore hardly surprising that in fig. 5.6 this peak often vanishes, as can be seen from the gaps in the curves of peak position. The fully-divergent beam cases do not show any significant improvement in this. However, the peak is present in enough cases for an average peak position to be defined, and this is marked on the X_1 axis by X_c . The curves for the second peak are much better behaved and are similar in many respects to those of fig.5.2(b) for the undissociated screw dislocation. Yet again the variations are rapidly damped in the fully-divergent beam case from a thickness of $\sim 1.7\ \xi_g$ onwards as predicted by (4.11). The relation between Δ and Δ_{obs} for this case is

$$\Delta = \Delta_{obs} - 4.5 \pm 8 \text{ Å} \qquad (5.7)$$

Fig. 5.7 shows the curves for the wider dissociation of $\Delta = 21$ Å . With the fully-divergent beam the weaker peak is visible in every case considered, but with the parallel beam this peak cannot be detected for about 50% of the foil thicknesses used when the depth is $1.05\ \xi_g$. This shows that the divergent beam effect is of importance in those cases of medium to small dissociation for which parallel beam calculations suggest that resolution of both partials is often not possible. The relation between Δ and Δ_{obs} for this case is

$$\Delta = \Delta_{obs} - 3.5 \pm 8 \text{ Å} \qquad (5.8)$$

5.3.4 The edge dislocation

The line direction chosen for the dissociated edge dislocation was $[11\bar{2}]$, but in all other respects the geometry was similar to that employed in the dissociated screw computations above. Again two values of Δ were used. The results for the first, $\Delta = 34$ Å , are shown in fig. 5.8. The image correction derived from this figure is

$$\Delta = \Delta_{obs} - 9 \pm 7 \text{ Å} \qquad (5.9)$$

The other dissociation considered was $\Delta = 59$ Å , and the results of these calculations are plotted in fig. 5.9. This gives the relation

$$\Delta = \Delta_{obs} - 6 \pm 7 \text{ Å} \qquad (5.10)$$

It is interesting to note that in both these configurations and in the screw dissociation of 21 Å the weaker peak did not exist for most of the thicknesses considered at the depth $d = 1.05 \xi_g$ when assuming a parallel beam. This is an extreme example of intensity oscillation dependent on depth since the peak for $d = 1.00 \xi_g$ does not exhibit this behaviour. This depth effect is completely eliminated with the fully-divergent beam as may be seen in figs. 5.7, 5.8 and 5.9; this provides further confirmation of (4.11).

In all these graphs the peak positions as predicted by (1.81) have been indicated by the arrows X_w. The distance between these as given by (5.6) is in fact never in disagreement by more than 3 Å with the separation deduced from the arrows X_c, although this may not be the case with the other dissociation geometries. This supports the conclusion of Stobbs and Sworn (1971) that Δ_{obs} computed using anisotropy agrees with (5.6) to within 10% at $\Delta = 40$ Å, but their criticism that the positions of the individual peaks as given by (1.81) are in poor agreement with the computed profiles (e.g. 15 Å error for $\Delta = 40$ Å) is not found to be correct in the present calculations as may be seen by comparing the arrows X_c and X_w in figs. 5.6 to 5.9, where the greatest error is about 5 Å. Although their program did not assume the column approximation (see section 1.2.3), this is not thought to make significant changes in weak-beam images if the $\underline{g}(3\underline{g})$ diffraction conditions, rather than $\underline{g}(\bar{\underline{g}})$, are used (Howie and Sworn 1970), which is the case here.

5.4 The analysis of experimental images of dissociated dislocations in copper

This section applies the results of section 5.3.3 and 5.3.4 to the analysis of experimental weak-beam micrographs of dissociated dislocations in copper. The specimens were prepared in a similar manner to that outlined in section 3.4, except that an alternative final electro-

chemical polish was sometimes used; this was a 50% by volume solution of orthophosphoric acid in distilled water at room temperature and ~1V. In the analysis the definitions of screw and edge dislocations were relaxed to include dislocations of character 0° to 10° and 80° to 90° respectively. It has already been pointed out in section 5.3.2 that because of the properties of dissociated edge dislocation images as portrayed in fig. 5.5(e) some of the micrographs of near-edge dislocations could not be used. For the range of dislocations with character 10° to 80° no computations were available. It was shown in section 5.3.2 that these mixed dislocations can give rise to four different images in the manner of fig. 5.5(a). These dislocations have been included in this investigation for the sake of completeness by using the isotropic approximation and comparing them to whichever of the two possibilities given in (5.6) was appropriate. The results of this hybrid approach are shown in fig. 5.10 where Δ deduced from Δ_{obs} is plotted against dislocation character θ. All the dislocations were found to contain intrinsic faults when the procedure described in section 5.3.1 was applied. The near-screw and near-edge cases have been corrected by assuming a linear relation connecting the two cases considered in detail in sections 5.3.3 and 5.3.4. The intermediate cases are useful in that they define a shape for the curve, but many approximations have been used in their derivation. Most of the points lie in the range 45° to 90°. This is because the main interest lies with the screw and edge dissociations, and after a reasonable number of edge dislocations had been observed attention was focussed solely on finding near-screw dislocations and other orientations were ignored. This proved to be very difficult in practice, and the lack of dislocations observed with $\theta < 25^{\circ}$ has been noted previously by Cockayne, Jenkins and Ray (1971) who suggested that these dislocations may cross-slip to annihilate others of opposite sign in the bulk crystal or cross-slip out of the thin foil. These difficulties were not experienced by Stobbs and Sworn (1971) who used a copper crystal containing 0.5% by volume of silica in the form of a

dispersion of amorphous particles. Weak-beam micrographs of two dislocations near screw and edge in character are shown in fig. 5.11(a) and (b).

The points in diagrams such as fig. 5.10 may be used to estimate the intrinsic stacking-fault energy if it is assumed that the energy is constant across the width of the fault and that the dislocations have singular cores. The effect of different assumptions (e.g. extended dislocation cores) are considred in section 5.5. Because the separation is widest in the edge orientation the possible effects of finite core widths are minimized with dislocations of this character and so they should give the most reliable values of Δ for use in elasticity calculations. The force per unit length exerted by either partial on the other in the plane of dissociation according to anisotropic elasticity theory is given by (2.41), (2.32) and (2.37) as

$$F_1 = \frac{1}{2\pi\Delta} H_{ij}\, b_j(1)\, b_i(2) \qquad (5.11)$$

where H_{ij} depends on the elastic constants and the line direction, and $b_i(n)$ are the three components of the Burgers vector of partial dislocation n. For the dissociated edge dislocation in copper (5.11) takes the numerical form

$$F_1 = \frac{1541}{\Delta} \qquad (5.12)$$

where F_1 is in dynes/cm and Δ is in $\mathring{A}$. This formula is accurate to within 2% for values of θ lying in the range 80° to 90°. When the two partials are in equilibrium the force F_1 is numerically equal to the stacking-fault energy . Assuming that γ is a constant implies that there is only one equilibrium value of Δ, yet in fig. 5.10 there is a spread of approximately 12 $\mathring{A}$ in for $80^\circ \leqslant \theta \leqslant 90^\circ$. This may be compared with the predicted uncertainty in (5.9) and (5.10) of 14 $\mathring{A}$. At the end of section 5.2.1 it was pointed out that the effect of the divergent beam in eliminating variations in peak position does not permit the accuracy of interpretation of experimental micrographs to be improved unless it is

known that the defect is at least $\sim 0.7\,\xi_g$ from either surface. Exactly the same considerations apply to the accuracy of deduced partial separations in the case of dissociated dislocations. However, it is obvious from fig. 5.10 that this is only a problem when information from one particular micrograph is important; if many images of one class of defect are available, the uncertainty will be reflected in the spread of deduced separations, and the required value is simply the mean of these. In fig. 5.10 the results for $80^\circ \leqslant \theta \leqslant 90^\circ$ have an average value of 35 Å. Substituting this into (5.12) gives the stacking-fault energy for copper as

$$\gamma = 44 \text{ erg cm}^{-2} \qquad (5.13)$$

This method of taking the average separation and deriving γ from it was employed by Stobbs and Sworn (1971), who deduced a mean value of 38 Å and hence $\gamma = 41$ erg cm^{-2}. This is also the value of γ given by Cockayne, Jenkins and Ray (1971) but their approach was different. Their images were analysed by (5.6) and then two bounding curves of Δ versus θ computed by anisotropic elasticity theory were fitted to the points. These corresponded to $\gamma = 32$ and 50 erg cm^{-2}, and thus they concluded that $\gamma = 41 \pm 9$ erg cm^{-2}. This method can be applied to the results in fig. 5.10 if the edge separations are re-corrected by (5.6) rather than by (5.9) and(5.10). This corresponds to an average increase in Δ of ~ 2.5 Å. The results for $\theta > 45^\circ$ then lie roughly between the two curves corresponding to $\gamma = 34$ and 54 erg cm^{-2}, giving the result $\gamma = 44 \pm 10$ erg cm^{-2}. The agreement with (5.13) is of course coincidental. It is felt that deducing γ from the mean edge separation is the more correct approach, especially as it confines the application of elasticity theory to the widest separations for which finite core effects are minimized. The small increase in the value of γ as given in (5.13) over that deduced in the two previous studies is a result confirmed by the weak-beam observations of Carter (private communication).

It is clear from fig. 5.10 that the three points for which $\theta < 30^\circ$

do not lie on the curves given by anisotropic elasticity theory, and suggest a value of Δ in the screw orientation of ~ 23 Å . This effect has also been reported by Stobbs and Sworn (1971), although their value of 18 Å lies nearer to the theoretical curve for $\gamma = 41$ erg cm^{-2} . Such behaviour is possible evidence for the existence of finite dislocation core widths and the consequences of this are discussed in the next section.

5.5 The effect of the dislocation core on the determination of stacking-fault energy

Anisotropic elasticity theory and the assumption of singular dislocation cores enters in two stages of the determination of the stacking-fault energy of copper in section 5.4. Firstly, it is used in the computation of weak-beam images to represent the strain field of the dissociated dislocation. Secondly, it is used to calculate the force between the partial dislocations as a function of their separation. There is clearly a possibility of considerable systematic errors occurring in this procedure. Such effects were first considered by Cockayne, Jenkins and Ray (1971) who interpreted their value for the edge dislocation dissociation by the method of Seeger and Schöck (1953) which is based on a Peierls model for the core and uses anisotropy theory. The result of this was to reduce the value of γ from 41 to 32 erg cm^{-2} . However, the later investigations of Cockayne and Vitek (1974) have shown that different widths and distributions of the core for a fixed partial separation can give values of the stacking-fault energy which are higher, lower or even equal to the value deduced from singular core theory. They also pointed out that the various parameters describing the core could change with line orientation, and so no one model need explain the complete curve of Δ versus θ. (Although the analysis of Seeger and Schöck (1953) gives a different value for γ , the orientation dependence is similar to that given by anisotropy theory, and so does not explain the observed behaviour). Image computations (using isotropic elasticity and a distribution of dislocations

to represent the core) also gave the important result that the average value of Δ_{obs} for a particular Δ was almost independent of the core model used; increasing the core width merely increased the uncertainty limits. It has already been shown in the previous section that these limits do not present a problem when a reasonable number of similar observations are available. The fact that the observed spread of 12 Å in the present case is less than the theoretical maximum of 14 Å even before core effects are considered may be evidence that, at least in the edge orientation, such effects are negligible.

A different approach to this problem is that of Perrin and Savino (1973), who computed the core configuration of an extended edge dislocation and its equivalent weak-beam image by using the atomic potential for copper constructed by Englert, Tompa and Bullough (1970) and a relaxation procedure. They assumed a value of 70 erg cm^{-2} for γ and then found that on the basis of this model the predicted values of Δ and Δ_{obs} were 32 Å and 54 $\pm$ 4 Å respectively. This latter figure overlapped with the observed widths of 47 $\pm$ 6 Å reported by Stobbs and Sworn (1971). For $s_g = 2.10^{-2}$ $Å^{-1}$ (5.6) gives the image width for Δ = 32 Å as Δ_{obs} = 43 $\pm$ 7 Å and so the findings of Perrin and Savino (1973) are in conflict with those of Cockayne and Vitek (1974) who found no significant change in the average value of Δ_{obs} due to core extension. They suggested that a thorough investigation of depth and thickness dependence effects in the images based on the atomistic model may lower or remove this discrepancy. Atomistic models do however have the advantage that the orientation dependence of the dissociation may be investigated since there are no variable parameters such as the core width to be defined.

An ingenious model which combines this advantage of the atomistic approach together with that of a straightforward mathematical description is given by strain-gradient elasticity. In this theory terms containing derivatives of strain are considered as well as simple strain, and the stress field of a dislocation then includes modified Bessel functions.

Jones and Steeds (1974) analysed the results for copper given by Stobbs and Sworn (1971). Fitting the data at $\theta = 30^{\circ}$ and 90° fixed the value of γ and the amplitude of the Bessel function term. The value of Δ at screw orientation was then successfully predicted by the theory.

It is clear that the value of γ obtained from any of the various approaches which try to allow for the effect of core extension may differ significantly from the result derived assuming anisotropic elasticity and singular cores. It is also apparent from fig. 5.10 and the results of Stobbs and Sworn (1971) that some explanation is needed for the disagreement with the simple theory at screw orientations. However, it has been pointed out that the conclusions of Cockayne and Vitek (1974) concerning the effect of core extension on image width suggest that the average value of 35 Å for $80^{\circ} \leqslant \theta \leqslant 90^{\circ}$ in fig. 5.10 is accurate, and that any extension is small for these orientations because of the low spread in observed widths. In the weak-beam study of faulted dipoles in copper described in Chapter 3, which also assumed singular cores in all stages of the investigation, an upper limit on γ of 47 ± 8 erg cm^{-2} was derived. The line direction and Burgers vectors in this defect are different from those of the simple dissociated edge dislocation considered here, so any effects due to non-singular cores should cause a disagreement in the deduced values of γ. The very good agreement between this value and that given in (5.13) is strong evidence for supposing that for the faulted dipole and the dissociated edge dislocation in copper any effects due to finite core width are negligible.

5.6 Conclusions

It has been shown in this chapter that the effects of divergent beam illumination suggested in Chapter 4, and in particular (4.11), are observed in theoretical weak-beam images of undissociated and dissociated dislocations in copper. The smoothing of intensity oscillations is particularly interesting since in the case of small point-defect clusters some doubt has been expressed in the past as to their visibility and the

reliability of determining defect numbers and size-density counts from weak-beam images (Häussermann, Katerbau, Rühle and Wilkens 1973). Calculations performed in the manner described in this chapter may show that these fears are groundless.

The calculated images for dissociated dislocations have been used to analyse experimental observations in copper, and some care was taken to select the correct micrographs for comparison with theory. The results give average separations of the partials in the dissociated screw and edge orientations of ~ 23 Å and 35 Å respectively. The figure of 35 Å analysed by anisotropic theory gives the stacking-fault energy of copper as

$$\gamma = 44 \text{ erg cm}^{-2} .$$

This is slightly higher than previously reported values determined by weak-beam observations. The figure for the screw dissociation is not in agreement with anisotropic theory suggesting the existence of extended core effects, which can alter significantly the deduced value for γ. However, the results of Cockayne and Vitek (1974) when compared with the observed spread in image widths of the dissociated edge dislocations, and the value of γ_{max} obtained from the study of faulted dipoles in Chapter 3, suggest that core effects do not seriously affect the accuracy of the value $\gamma = 44 \text{ erg cm}^{-2}$.

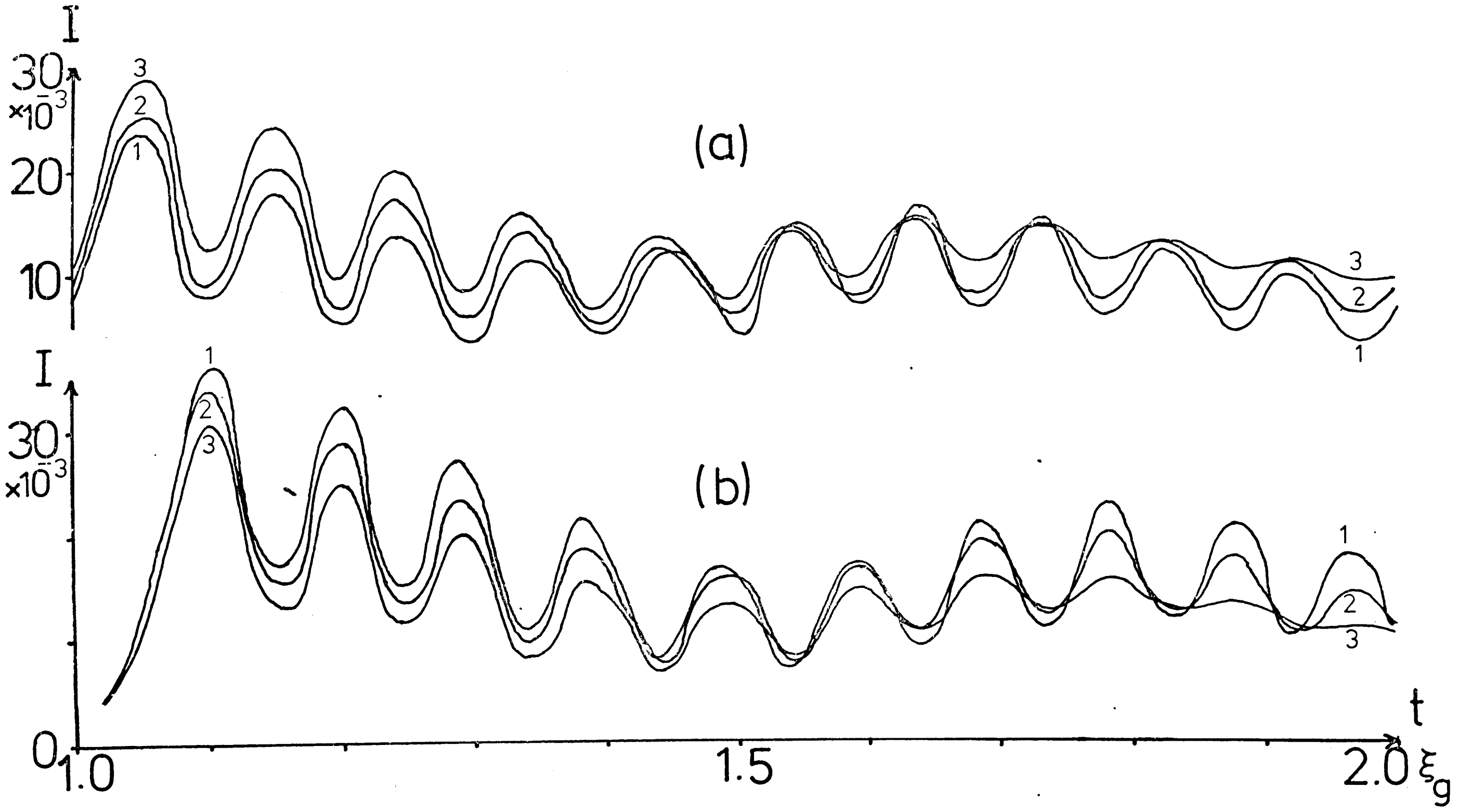
I
30
×10⁻³
20
10
0
3
2
1
(a)
I
30
×10⁻³
1
2
3
(b)
t
1.0
1.5
2.0
ξg

Figure 5.1 Intensity oscillations with thickness for an undissociated screw dislocation.

(1) parallel (2) semi-divergent (3) fully-divergent illumination.

(a) $d = 1.00\,\xi_g$

(b) $d = 1.05\,\xi_g$

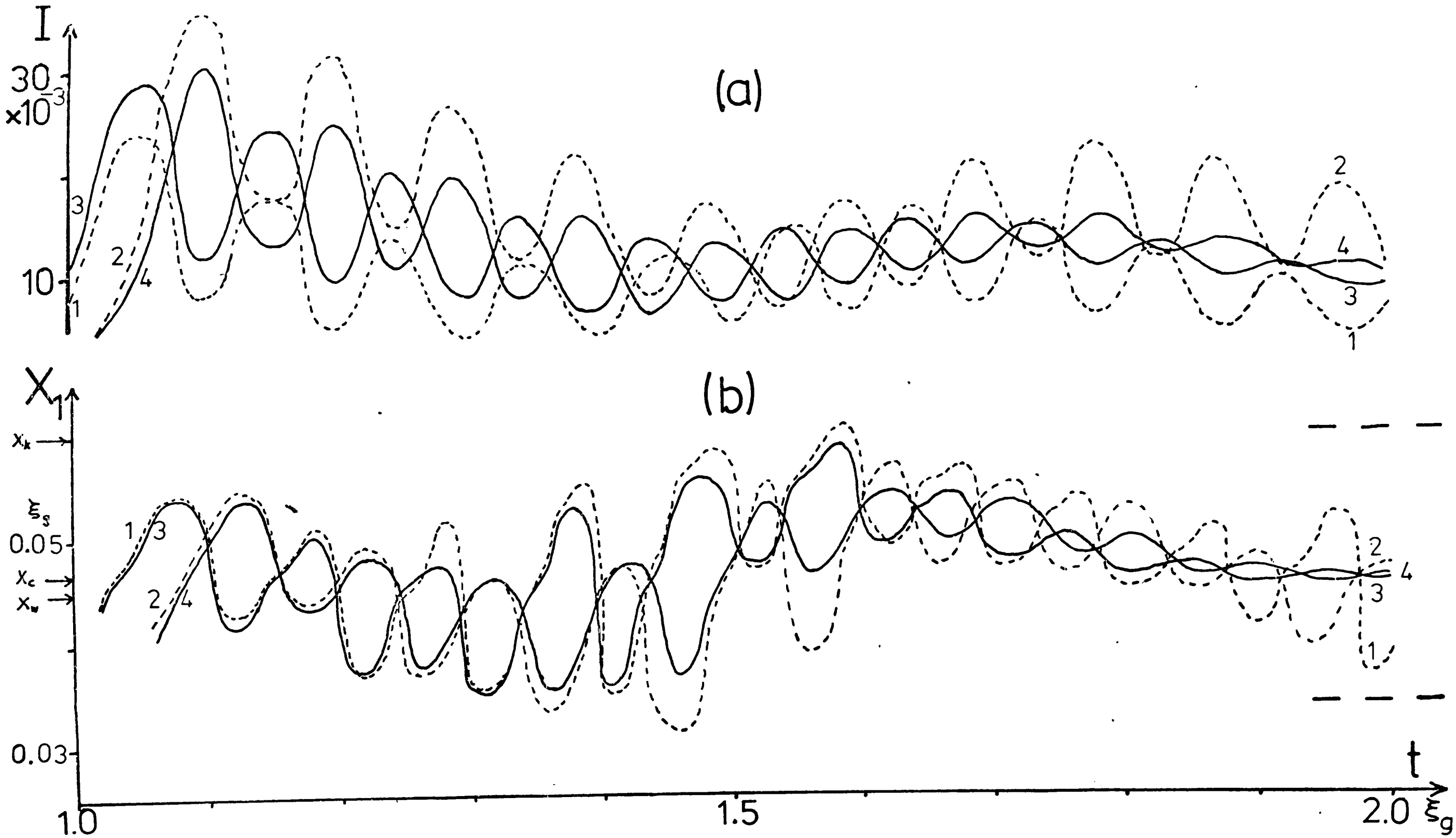
I
30
×10⁻³
10
(a)
1
2
3
4
X
X_k
ξ_s
0.05
X_c
X_w
0.03
(b)
1
2
3
4
t
1.0
1.5
2.0
ξ_g

Figure 5.2 Undissociated screw dislocation.

(1) parallel beam, d = 1.00 ξ_g

(2) parallel beam, d = 1.05 ξ_g

(3) fully-divergent beam, d = 1.00 ξ_g

(4) fully-divergent beam, d = 1.05 ξ_g

(a) peak intensity oscillations with thickness

(b) peak position oscillations with thickness

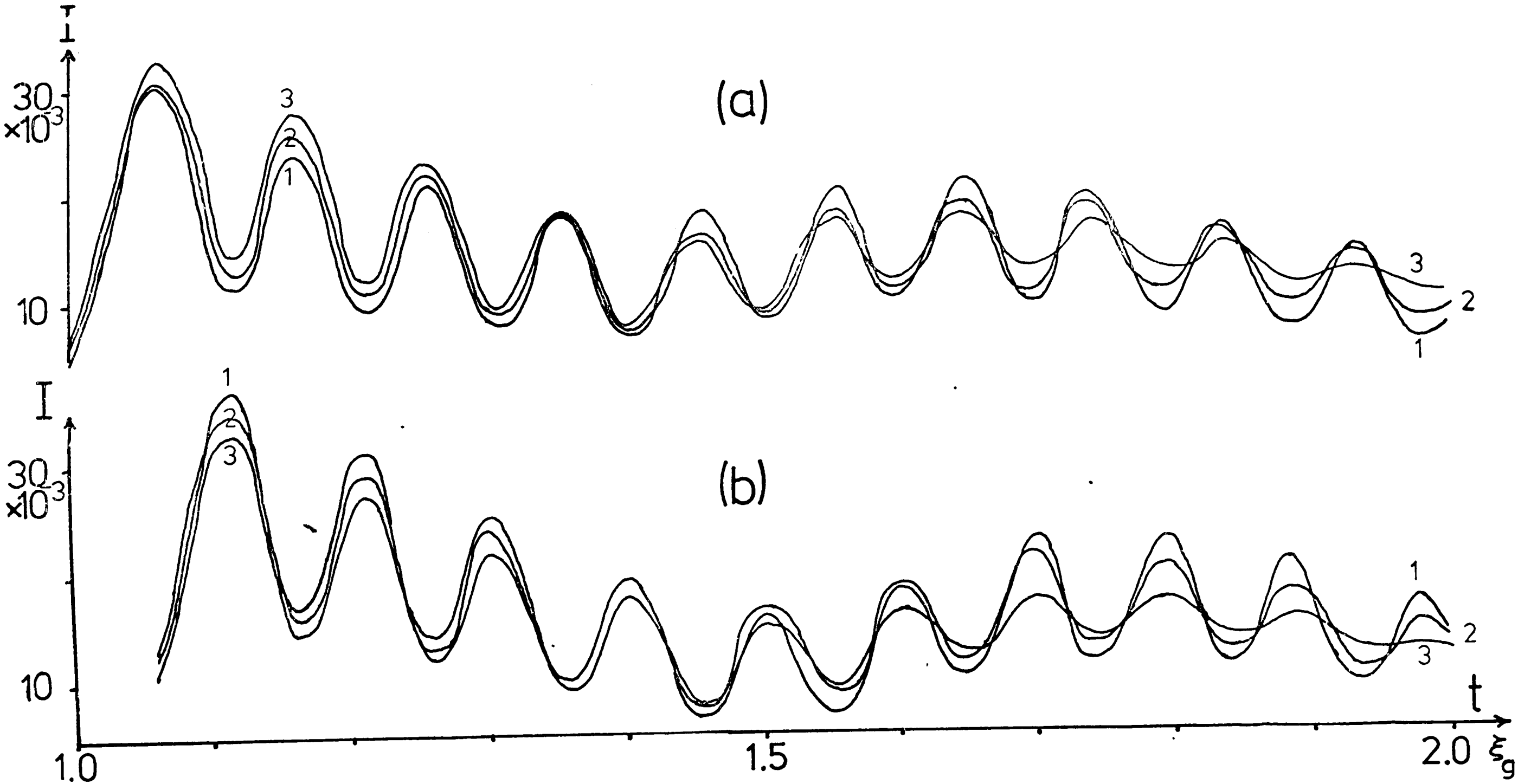
I
30
×10³
10
(a)
3
2
1
1
2
3
I
30
×10³
10
(b)
1
2
3
1
2
3
t
1.0
1.5
2.0
ξg

Figure 5.3 Intensity oscillations with thickness for an undissociated edge dislocation.

(1) parallel (2) semi-divergent (3) fully-divergent illumination.

(a) $d = 1.00\xi_g$

(b) $d = 1.05\xi_g$

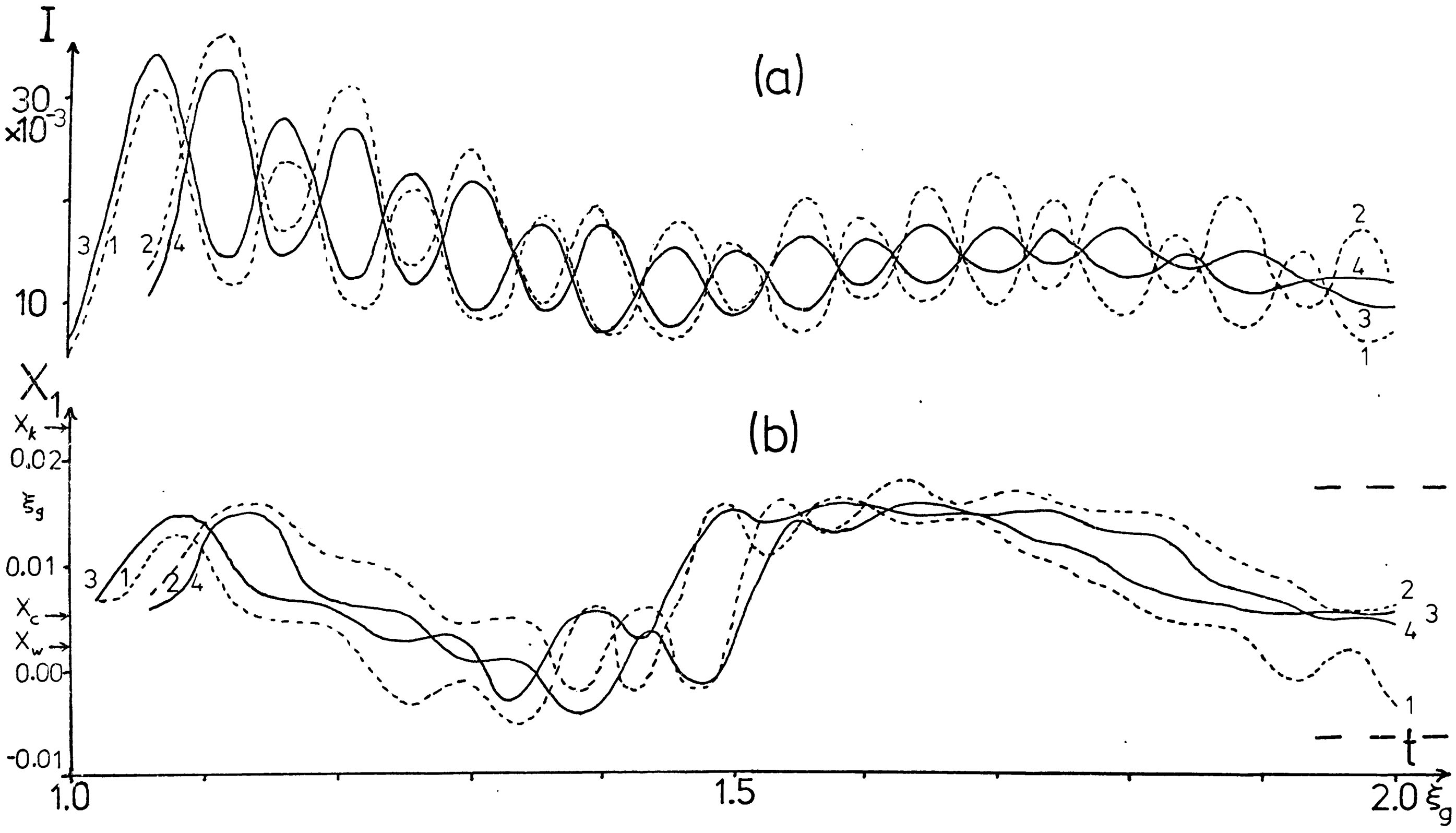
I
30
×10⁻³
10
(a)
1
2
3
4
X
X_k
0.02
ξ_g
0.01
X_c
X_w
0.00
-0.01
(b)
t
1.0
1.5
2.0
ξ_g

Figure 5.4 Undissociated edge dislocation.

(1) parallel beam, d = 1.00 ξ_g

(2) parallel beam, d = 1.05 ξ_g

(3) fully-divergent beam, d = 1.00 ξ_g

(4) fully-divergent beam, d = 1.05 ξ_g

(a) peak intensity oscillations with thickness

(b) peak position oscillations with thickness

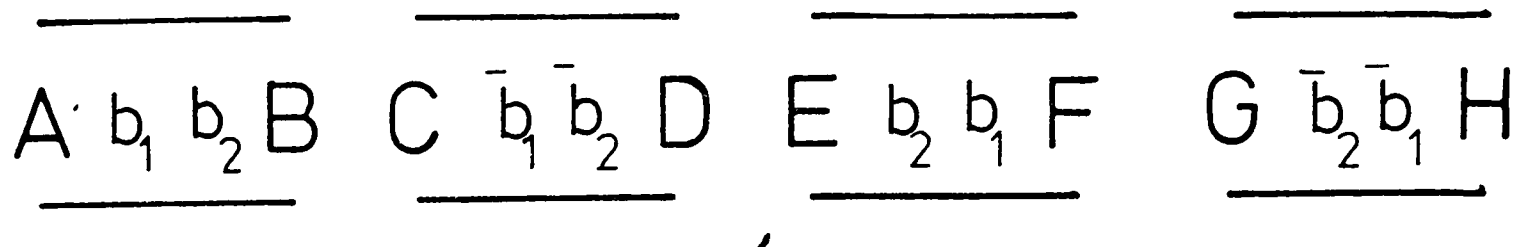
A b1 b2 B C b̄1 b̄2 D E b2 b1 F G b̄2 b̄1 H

(a')

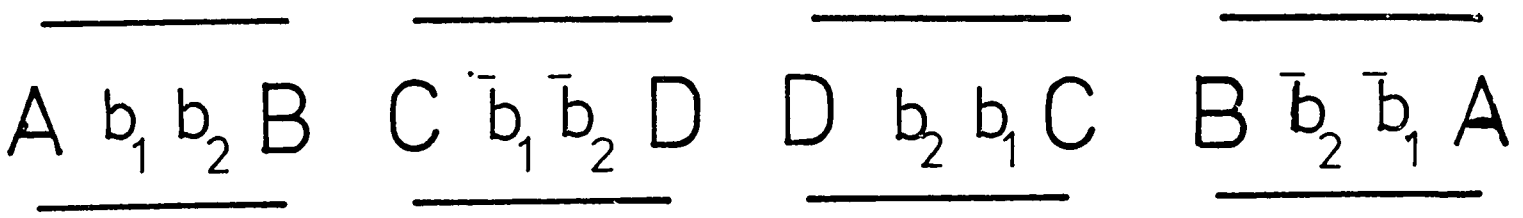
A b1 b2 B C b̄1 b̄2 D D b2 b1 C B b̄2 b̄1 A

(b)

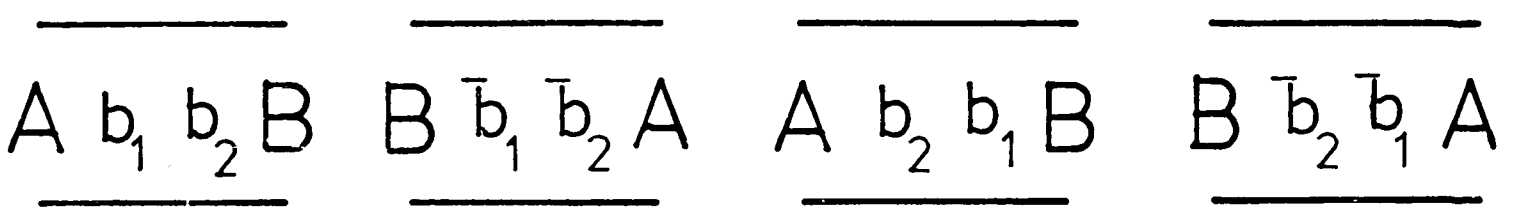
A b1 b2 B B b̄1 b̄2 A A b2 b1 B B b̄2 b̄1 A

(c)


A b1 b2 B C b̄1 b̄2 D A b2 b1 B C b̄2 b̄1 D

(d)

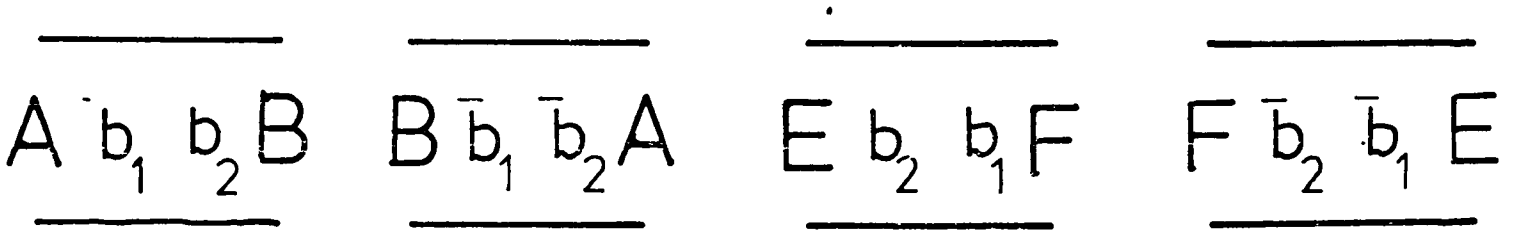
A b1 b2 B B b̄1 b̄2 A E b2 b1 F F b̄2 b̄1 E

(e)

Figure 5.5 Dissociated dislocation image symmetries.

$\bar{b}_1$, b_2 etc. represent the position and sign of the partial dislocations. The letters AB etc., represent certain values of the product $\underline{g}.\underline{R}$ on either side of the dislocation.

(a) anisotropy, general character

(b) isotropy, general character

(c) isotropy, edge or screw

(d) anisotropy, screw

(e) anisotropy, edge

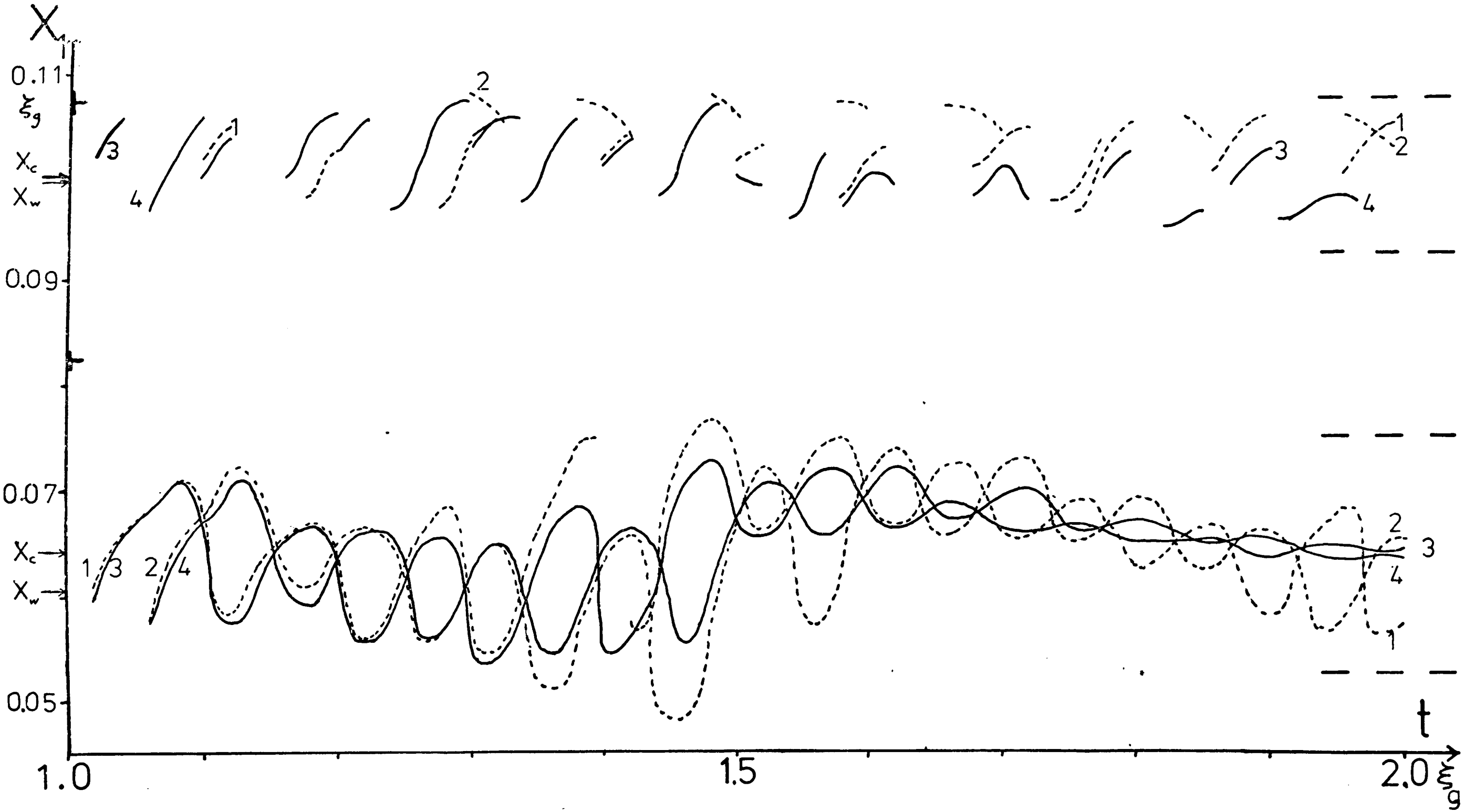
X
0.11
ξ_g
X_c
X_w
0.09
0.07
0.05
1.0
1.5
2.0
t
1
2
3
4

Figure 5.6 Dissociated screw dislocation peak positions.

$\Delta = 10.5$ Å .

(1) parallel beam, d = 1.00 ξ_g

(2) parallel beam, d = 1.05 ξ_g

(3) fully-divergent beam, d = 1.00 ξ_g

(4) fully-divergent beam, d = 1.05 ξ_g

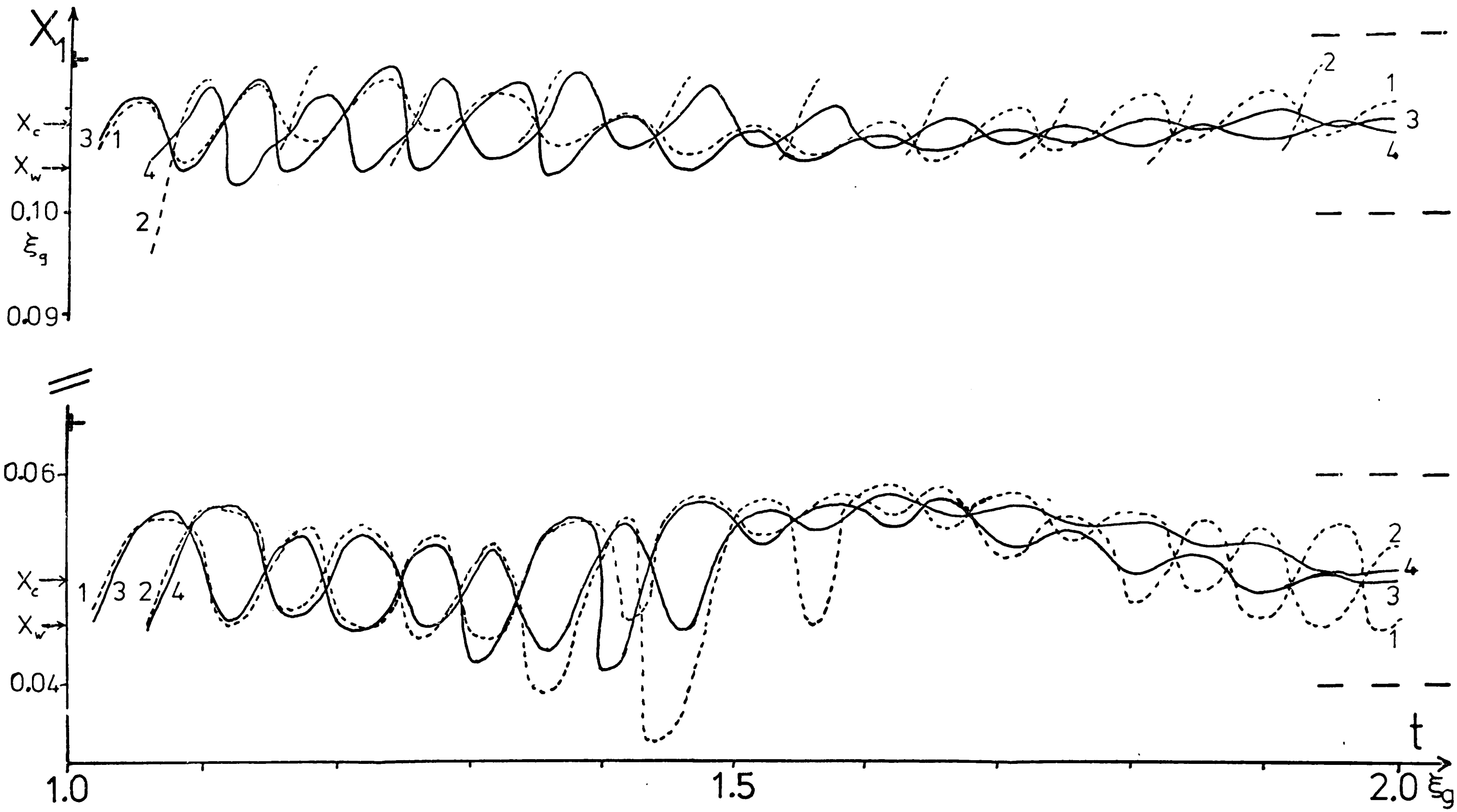
X_1
X_c
X_w
0.10
ξ_g
0.09
3
1
4
2
2
1
3
4
0.06
0.04
1 3 2 4
2
4
3
1
t
1.0
1.5
2.0 ξ_g

Figure 5.7 Dissociated screw dislocation peak positions.

Δ = 21 Å .

(1) parallel beam, d = 1.00 ξ_g

(2) parallel beam, d = 1.05 ξ_g

(3) fully-divergent beam, d = 1.00 ξ_g

(4) fully-divergent beam, d = 1.05 ξ_g

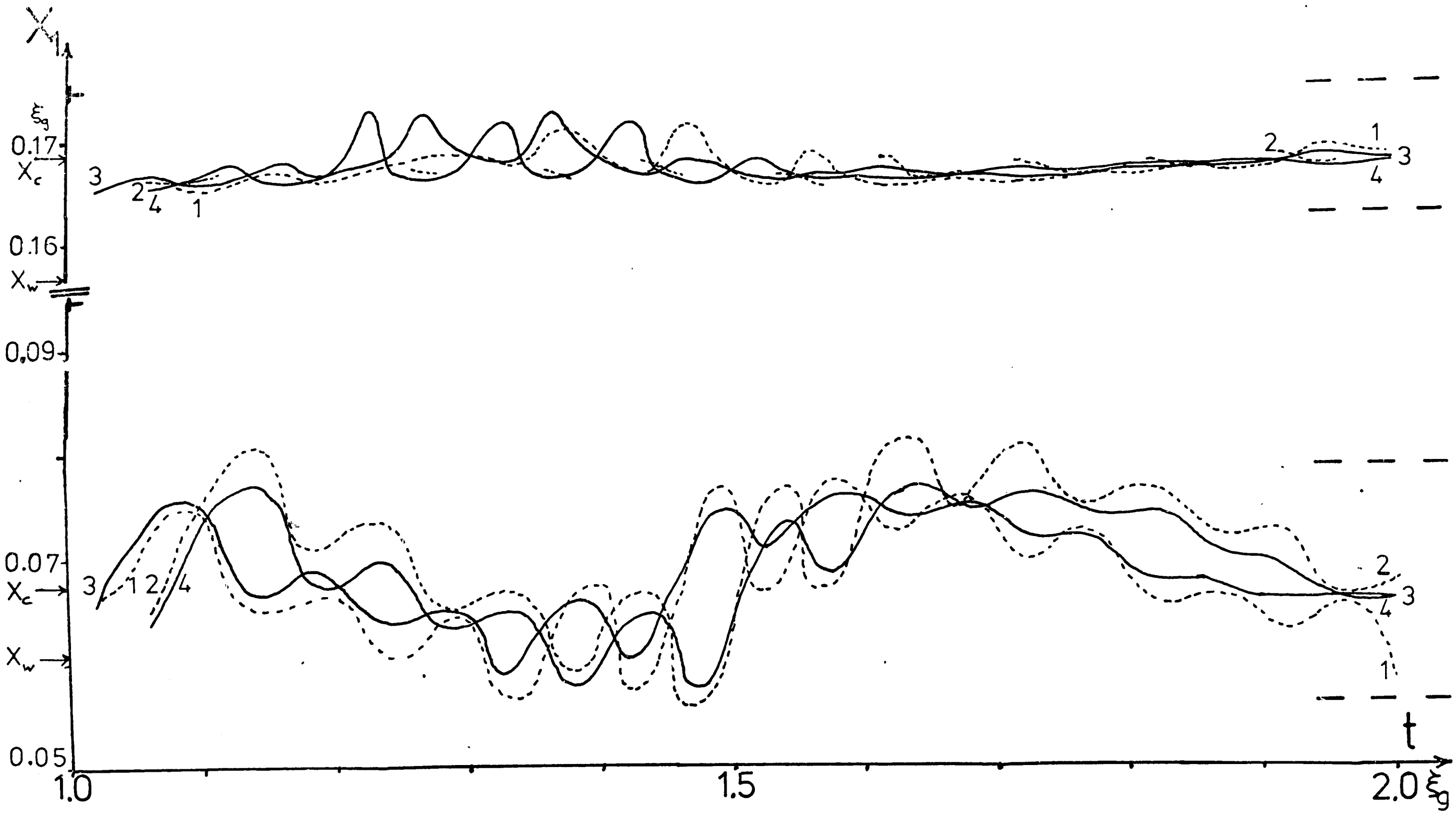
X_1
ξ_g
0.17
X_c
0.16
X_w
0.09
0.07
X_c
X_w
0.05
1.0
1.5
2.0
ξ_g
t
1
2
3
4

Figure 5.8 Dissociated edge dislocation peak positions.

Δ = 34 Å.

(1) parallel beam, d = 1.00 ξ_g

(2) parallel beam, d = 1.05 ξ_g

(3) fully-divergent beam, d = 1.00 ξ_g

(4) fully-divergent beam, d = 1.05 ξ_g

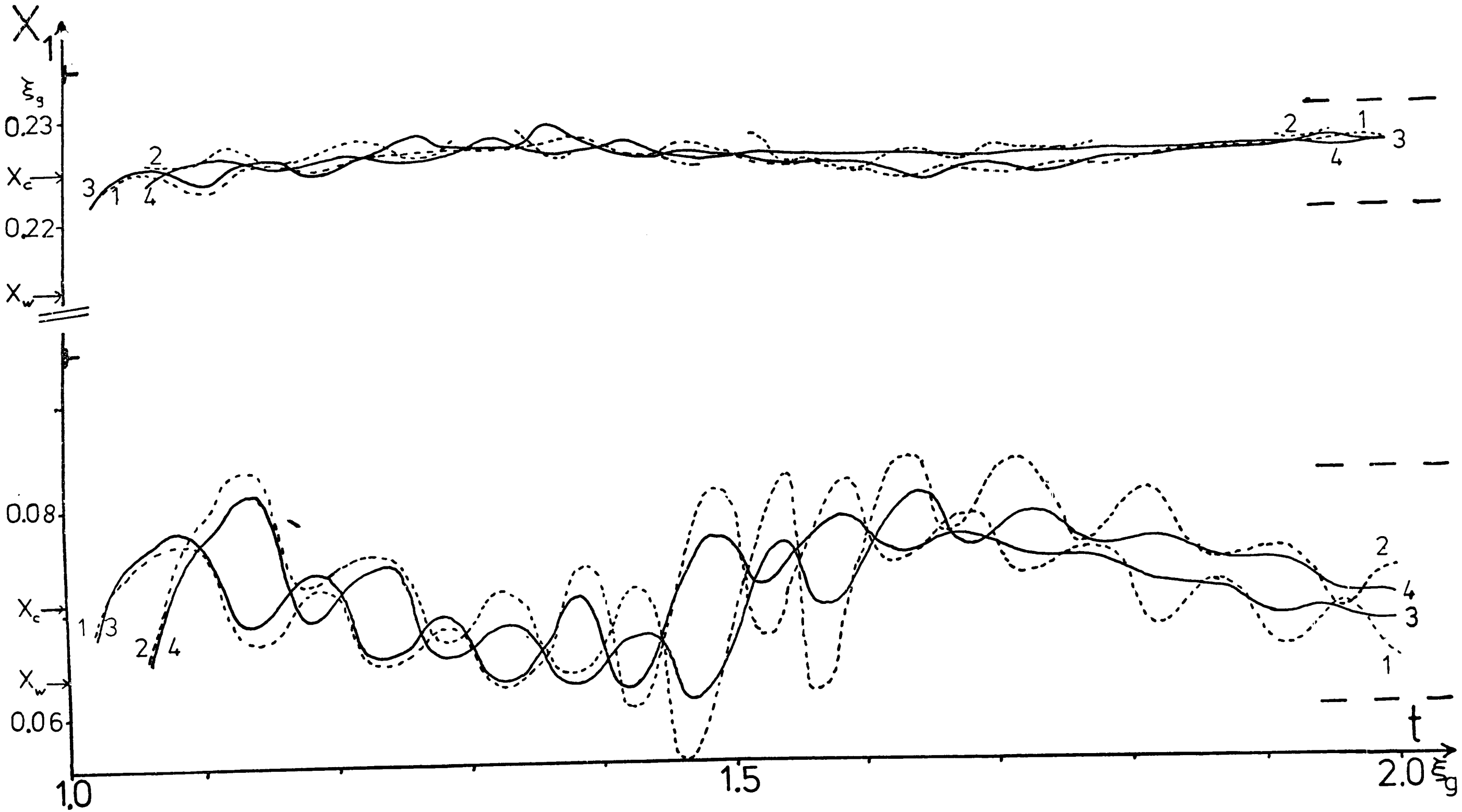
X1
ξg
0.23
Xc
0.22
Xw
0.08
0.06
1.0
1.5
2.0 ξg
t
1
2
3
4

Figure 5.9 Dissociated edge dislocation peak positions.

$\Delta = 59$ Å .

(1) parallel beam, d = 1.00 ξ_g

(2) parallel beam, d = 1.05 ξ_g

(3) fully-divergent beam, d = 1.00 ξ_g

(4) fully-divergent beam, d = 1.05 ξ_g

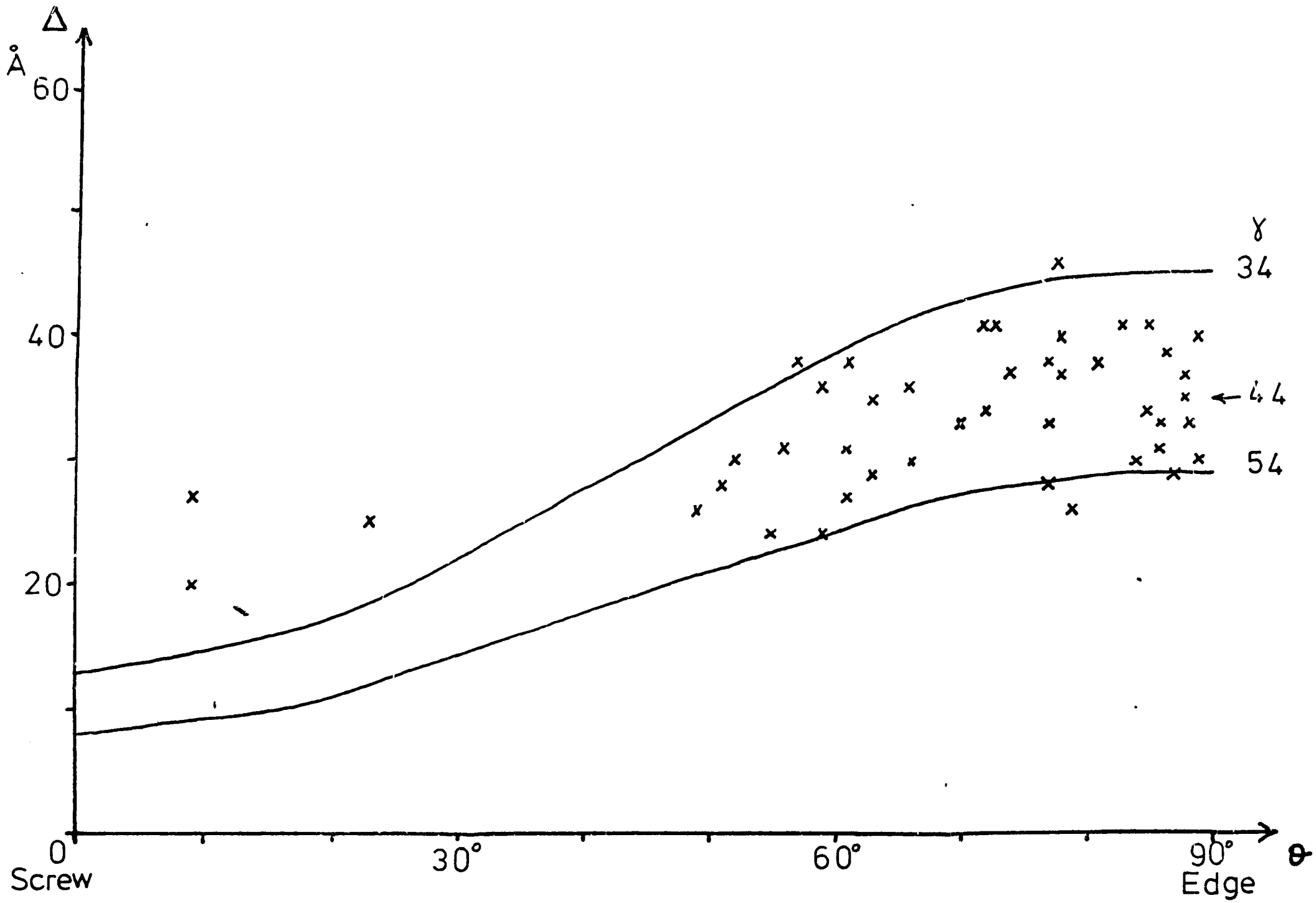
Δ
Å
60
40
20
0
Screw
30°
60°
90°
Edge
θ
γ
34
44
54

Figure 5.10 The curve of dislocation dissociation against character for pure copper.

The points have been analysed as follows:-

0^{o} to 10^{o} by computation

10^{o} to 80^{o} by the criterion (5.6)

80^{o} to 90^{o} by computation

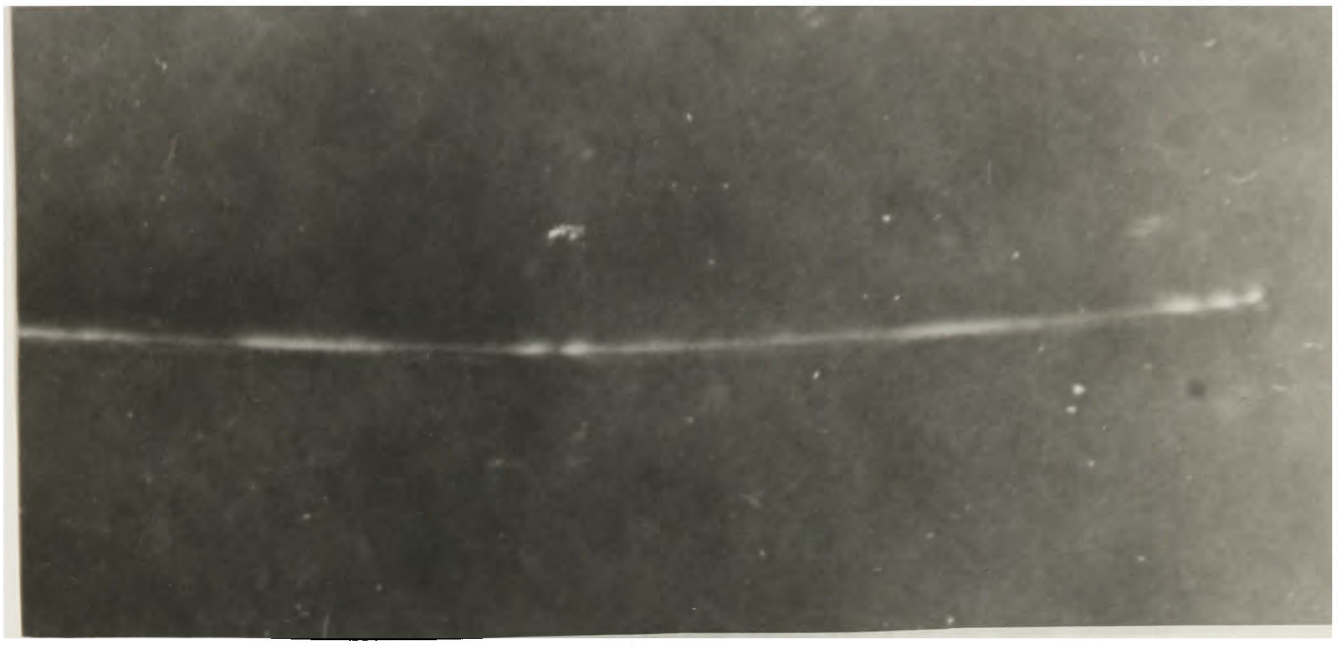

(a)

g, b

500 Å

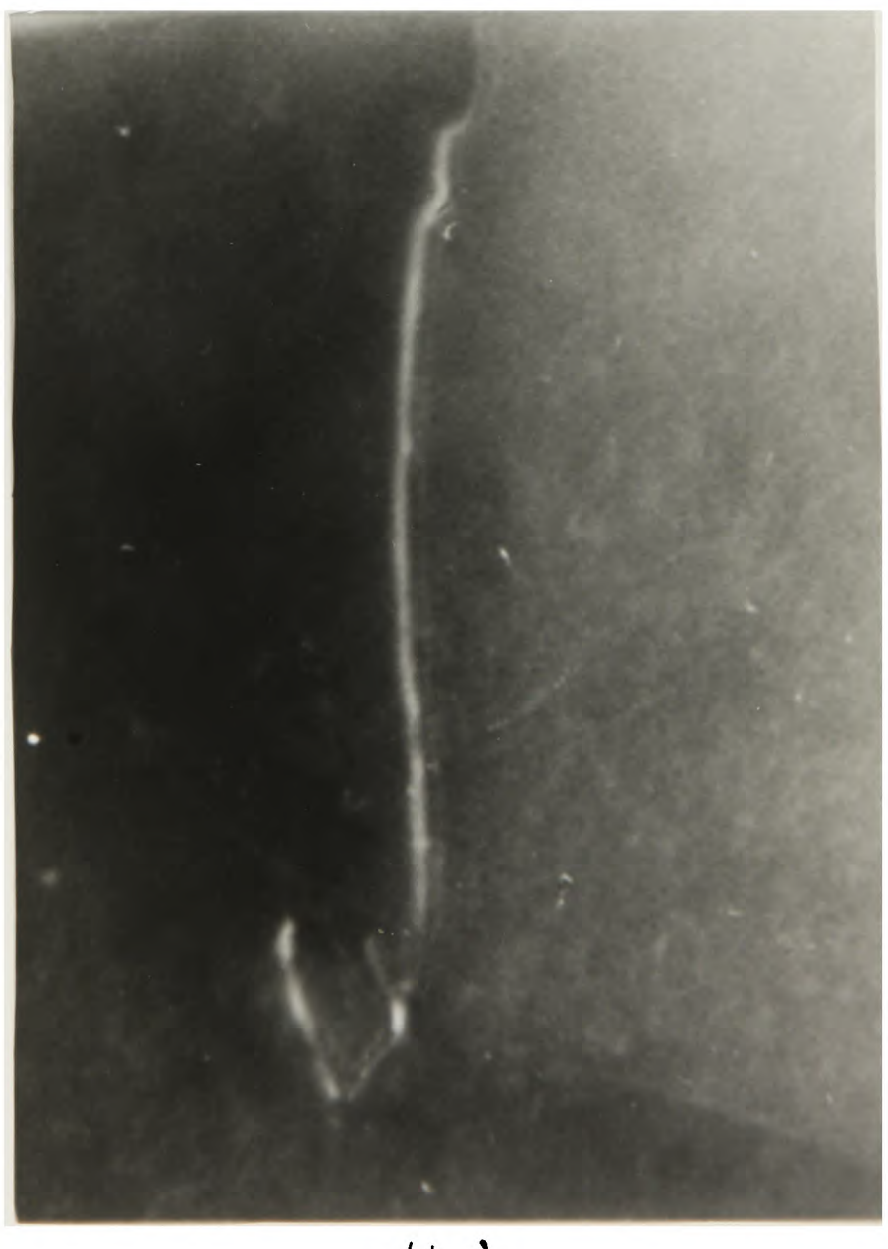

(b)

Figure 5.11(a) Dissociated near-screw dislocation in copper.

Figure 5.11(b) Dissociated near-edge dislocation in copper.

Chapter 6

Weak-beam images of dissociated Frank loops using divergent illumination

6.1 Introduction

The term radiation damage is used to describe the large variety of defects produced when a material is bombarded with energetic particles. This damage may be in the form of voids, perfect loops, faulted loops, dissociated loops or stacking-fault tetrahedra. Much work has been done on such defects under strong-beam dynamical conditions when (except in the case of voids) the images are in the form of one or more black and white lobes, and this is generally called black-white contrast. The extent of such contrast is usually much larger than that of the defect producing it, and this is one of the reasons for the success of strong-beam investigations. The contrast varies with the depth in a layer manner; changing the depth by $\xi_g/2$ reverses the black-white effect. The nature of these defects (interstitial or vacancy) can be determined if it is known in which layer they occur (e.g. by stereo measurements) by applying the rule given by Ashby and Brown (1963) and noting the sense of the black-white effect with respect to $\underline{g}$. In the case of self-ion irradiated copper Wilson (1970, 1971)and Wilson and Hirsch (1972) interpreted fine detail in the interface between the black and white lobes as evidence of the dissociation of small Frank loops in the first stage of the mechanism of formation of a stacking-fault tetrahedron given by Silcox and Hirsch (1959). Some doubt was cast on this interpretation by Eyre (1973) who said that Eyre, Maher and Perrin (unpublished) had found the interface structure in computed images of edge loops in body-centred cubic metals to be very sensitive to the exact loop depth. However, Jenkins (1973, 1974) has studied similar damage by the weak-beam technique in {220} reflections at the (111) pole and showed by simple arguments that all the observed contrast features could be explained by a dissociated Frank loop. He did not resolve the separate partial dislocations in the dissociation (a stair-rod and a Shockley) since the image peaks due to these were superimposed on the contrast of the stacking faults. Bollinger, Condat and Fayard (1974)

have observed large Frank loops edge-on in a Cu 5at.% Si alloy with the weak-beam technique at a (112) pole in {111} reflections and imaged the stacking fault between the two partials. It would clearly be advantageous when studying small defects to image just the two dislocations rather than the stacking faults. This chapter describes the investigation of suitable conditions using large Frank loops in copper and copper-aluminium alloys formed by electron radiation in a high-voltage microscope at elevated temperatures. The use of large loops enables any one side to be treated independently as two parallel infinite dislocations; this simplifies the image simulation process.

6.2 The growth of large Frank loops and the denuded zone effect

Ipohorski and Spring (1969) first reported the formation of large ($\sim 1\mu$) faulted loops on {111} planes in copper during electron irradiation and found them to be interstitial in character. The straight edges of the loops in their images lie along the projections of <110> directions suggesting the possibility of dissociation of the edges on to other {111} planes. They found that the experimental conditions required to produce such loops depended on several factors, including the electron energy and beam current density, specimen temperature and fitness, and the degree of contamination present (surface stresses due to contamination were found to encourage the loops to slip out of the foil before attaining a large size). Theories describing the growth of these defects have been discussed by several workers, including Brown (1969), Makin (1969) and Norris (1970). Vacancies are considered to be immobile while interstitials either join a loop or are annihilated at some other sink. Idealizing the problem to a circular loop of radius r, the number of interstitials in the loop N is $\frac{\pi r^2}{\Omega\xi}$ where Ω is the atomic volume; therefore the rate at which they join the loop may be written

$$\frac{dN}{dt} = \frac{2\pi r}{\Omega\xi}\left(\frac{dr}{dt}\right) \qquad (6.1)$$

If there are Z_1 sites per atom site in the loop perimeter from which spontaneous combination may occur, and n sites in the total catchment volume V acting as interstitial sinks, the probability that an interstitial will join the loop is $\frac{2\pi r Z_1}{\Omega^{\frac{1}{3}} n}$; then if G is the point defect creation rate per unit volume, the rate at which interstitials join the loop is

$$\frac{dN}{dt} = GV\left(\frac{2\pi r Z_1}{\Omega^{\frac{1}{3}} n}\right) \tag{6.2}$$

Equating (6.1) and (6.2) gives

$$\frac{dr}{dt} = \frac{\Omega^{\frac{1}{3}} GV Z_1}{n} \tag{6.3}$$

The form of the solution for r depends on the choice of n. Brown (1969) and Makin (1969) assumed that, apart from the loop itself, the only contribution to n was from the vacancies left by the interstitials. Then if each vacancy has associated with it Z_v sites with which spontaneous recombination could occur,

$$n = \frac{\pi r^2 Z_v}{\Omega^{\frac{2}{3}}} + \frac{2\pi r Z_1}{\Omega^{\frac{1}{3}}} \tag{6.4}$$

For the growth of large loops the second term is negligible and substitution in (6.3) results in

$$r = \left(\frac{3GV\Omega Z_1}{\pi Z_v}\right)^{\frac{1}{3}} t^{\frac{1}{3}} \tag{6.5}$$

An alternative choice for n was considered by Norris (1970) who assumed the surfaces to be the dominant sink. If the foil thickness is h,

$$n = \frac{2V}{h\Omega^{\frac{2}{3}}} \tag{6.6}$$

Substituting in (6.3) and solving gives

$$r = \frac{Gh\Omega Z_1 t}{2} \tag{6.7}$$

This linear behaviour with time, rather than the $\frac{1}{3}^{rd}$ power law of (6.5), was observed by Norris (1970) in the irradiation of nickel, and comparison

with the experimental figures produces a value for Z_1 which is physically plausible, 1.4, unlike the result of 0.28 obtained by Makin (1969) in the case of copper when assuming (6.5).

Denuded zones next to the foil surfaces where no loops occur are a common feature of this irradiation technique (e.g. Makin 1968; Ipohorski and Spring 1969). This can be explained by considering the original homogeneous nucleation process in which it is assumed that the di-interstitial is an immobile stable nucleus. The density of these nuclei rapidly approaches a constant value, and subsequent irradiation only causes the nuclei to grow. Makin (1969) gives this initial nucleation time as

$$\tau = \frac{1}{GV} \tag{6.8}$$

(His value for copper irradiated with 600 keV electrons at room temperature was $\sim 5.10^{-5}$ sec). If ν_i is the interstitial jump rate, and λ the jump distance, in the nucleation time the interstitials migrate a mean distance

$$x = \sqrt{\nu_i \lambda^2 \tau} \tag{6.9}$$

Within this distance of a surface no nucleation is expected. Makin (1969) has published curves of the foil thicknesses 2x in which no loops are predicted in copper for various irradiation voltages and temperatures; he found that the agreement was good at room temperature. At higher temperatures the assumption of a stable di-interstitial nucleus becomes questionable since it may migrate or dissociate, the net effect being an increase in the nucleation time τ. From (6.9) it can be seen that this should increase the denuded zone thickness. To anticipate the results of the next section, it was found experimentally when irradiating copper at $\sim 500^{\circ}K$ with 900 keV electrons that large loops formed in foils much thinner than 2x as predicted by (6.9), even before making allowance for the increase in the nucleation time. The effects of the surface have been taken into account properly by Goringe (1971) who applied Fourier techniques to the theoretical equations of Brown, Kelly and Mayer (1969). He has shown that

the growth behaviour is dependent on the dimensionless parameter P defined as

$$P = \frac{\pi^2 \alpha \lambda}{h^2} \sqrt{\frac{v}{GV}} \qquad (6.10)$$

where α is a numerical constant of order unity and v is the interstitial migration speed (dependent exponentially on temperature). For large P (thin foils at high temperature) the loop radius increases approximately linearly with time (as predicted by (6.7)) , whereas for small P (thick foils at low temperature) the $\frac{1}{3}^{rd}$ power law is obeyed (6.5), although in all cases the exact rate varies with time. This theory also predicts that the loop density is never zero, but its value in the centre of the foil and the behaviour when approaching the surface again depend on P; for large P (which is the case for the thin foils prepared for the weak-beam observations to be described in this chapter) the density at mid-foil is a factor of ~ 10 lower that that for small P (bulk specimen conditions) and the decrease in density near the surfaces is much more gradual, rather than the sharp cut-off effect when P is small (Goringe 1973). Such effects have been observed experimentally in irradiated copper (fig. 6 of Spring, Iporhorski and Goringe (1971)) where it was found that even at room temperature the denuded zone was ~ 500 Å thick.

It can therefore be seen that surface effects are very important in controlling interstitial loop-growth in irradiated specimens. The very large loops investigated here can only be produced at elevated temperatures, and the conditions for weak-beam image visibility dictated the use of thin foils. Both these requirements give a large value of P. Although theory always predicts a finite loop density, surface stresses can cause loops in very thin regions to slip out of the foil, thus enhancing the denuded zone effect. It is therefore to be expected that at the elevated temperature used no large loops should be formed in regions $\lesssim$ 1000 Å thick.

6.3 Specimen preparation

6.3.1 The formation of the loops

The materials studied were pure copper and copper-aluminium alloys containing 5 and 10 atomic per cent aluminium. $\{111\}$ slices were spark-cut from single crystals, and 3 mm discs cut from them. These were then jetted and electro-polished using the same conditions as described in section 3.4. It was found experimentally that the presence of other defects such as dislocations inhibited the formation of large loops; therefore prior to irradiation the polished specimens were annealed for about 5 minutes at 420°C. The specimens were then placed in the heating holder of an AEI high-voltage microscope and irradiated with 900 keV electrons at a rate of $1.5.10^{19}$ electrons cm^{-2} sec^{-1} for about 10 minutes at a temperature of ~ 280°C. This produced large straight-edged polygonal faulted loops in all the materials used. The determination of the ideal conditions and the preparation of the specimens was performed by Mr. D.G. Wilson. The loops were then observed in a JEOL JEM 100B operating at 100 kV with the foil titled so that the electron beam was in the $[\bar{1}\bar{1}0]$ direction.

6.3.2 The determination of the loop nature

It is usually assumed that loops formed in this manner are interstitial, and with all the loops for which the fault was determined this was found to be the case. Such determinations are most easily accomplished using the inside-outside contrast effect (e.g. see Hirsch et al. (1965) p.266). An example of this effect is shown in fig. 6.1 by two strong-beam dark-field (s positive) micrographs taken in $\pm$ $(\bar{1}13)$ of Frank loops in pure copper; fig. 6.1(a) is the outside -contrast case. The two large loops lie in the foil plane (this can be seen easily from the stacking-fault contrast in $\{111\}$ reflections; at the (110) pole two of the $\{111\}$ planes are vertical and so only two sets of loops are visible. Those in the foil plane (111) have uniform fault contrast whereas the loops on the $(11\bar{1})$ inclined to the foil display stacking-fault

fringes). The direction of tilt required to return to the (111) pole where the foil is normal to the electron beam is also drawn. This information shows that the loop faults are interstitial in nature.

6.4 The weak-beam imaging conditions

6.4.1 The geometry of the dissociated Frank partial

If the Frank partial at the edge of the loop lies along the $[1\bar{1}0]$ direction, it can dissociate into a stair-rod and a Shockley dislocation:-

$$\frac{a}{3}[\bar{1}\bar{1}\bar{1}] \rightarrow \frac{a}{6}[\bar{1}\bar{1}0] + \frac{a}{6}[\bar{1}\bar{1}2] \qquad (6.11)$$

This dissociation is shown in fig. 6.2(a) for a loop in the plane of a foil with upward normal $[11\bar{1}]$ tilted to the (110) pole. There are two possible positions for the Shockley dislocation which are marked A and B in the diagram, depending on whether an acute or an obtuse angle is formed. The nature of the fault created by the Shockley partial is opposite to that of the loop if the obtuse angle is preferred and since the loop itself is interstitial, an obtuse bend would create an intrinsic fault. The stair-rod has to lie perfectly straight along the $[1\bar{1}0]$ direction, but the Shockley is free to glide along the inclined $(11\bar{1})$ plane.

6.4.2 The $\{113\}$ images of a dissociated Frank partial

The requirements given in section 6.1 that the two partials be visible but that the stacking faults be out of contrast can be met by using $\{113\}$ reflections. Fig. 6.2(b) shows the diffraction pattern at the (110) pole and it can be seen that there are two $\pm\{113\}$ pairs. The partial dislocations have a $[1\bar{1}0]$ line direction and both are pure edge in character. This means that there is no component of the displacement $\underline{R}$ in the line direction, and so it is clear from fig. 6.2(b) that the images formed in $1\bar{1}3$ and $\bar{1}13$ must be identical. Therefore considerations of the contrast can be restricted to the $\pm(1\bar{1}3)$ cases without loss of generality. When imaged in these reflections, $|\underline{g}.\underline{b}| = 1$ for the Shockley partial; strong contrast is expected from the dislocation, but none from the fault.

For the stair-rod $\underline{g}.\underline{b} = 0$, but $|\underline{g}.\underline{b}\wedge\underline{u}| = \sim 0.7$, so some contrast may arise from this partial as well, but because $\underline{g}.\underline{b} = 0$ the main loop plane will not display stacking-fault contrast. The Shockley partial also has a $\underline{g}.\underline{b}\wedge\underline{u}$ factor of the same magnitude, so the image behaviour is likely to be more complex than that of the Shockleys in the dissociated dislocations of Chapter 5.

6.5 The weak-beam {113} image computations

6.5.1 The imaging parameters and defect geometry

To understand the model of the defect employed in the image computations it is necessary to study a typical experimental image. Fig. 6.3 is a micrograph of Frank loops in Cu 10at.% Al. It can be seen that the edges lie along <110> directions. The dissociation should only be visible for one of these directions since along the other two the dissociation is in a vertical plane. Two peaks can be seen along one edge of both loops (the smaller loop is on the $(11\bar{1})$ plane, i.e. inclined to the foil) and these may tentatively be associated with the two partials. The main point of interest is that the inner peak is straight, whereas the outer peak can bend in and out from various constrictions. Assuming that these two peaks do in fact represent the partials (which will be confirmed in section 6.5.3) the stair-rod is clearly the inner dislocation. Fig. 6.2(a) then shows that the dissociation has an obtuse bend, and so although the loop fault is extrinsic, the small dissociation contains an intrinsic fault. This geometry was noticed in all the loops observed, and suggests that in these materials the ratio of intrinsic to extrinsic stacking-fault energy is less than unity. Because of this effect the obtuse bend was assumed in the image computations. The Burgers vectors of (6.11) and fig. 6.2(a) were used in a foil of upward normal $[111]$ with the electron beam in the $[\bar{1}\bar{1}0]$ direction. Five-beam images were calculated in $\pm(1\bar{1}3)$ assuming anisotropic elasticity and the elastic constants of Cu 10at.% Al given by Hearmon (1956). These are slightly more anisotropic than those

for pure copper (A = 3.66 as opposed to 3.21) but the results should be a reasonable approximation to the images in copper (and Cu 5at.% Al) as well.

6.5.2 The parallel beam computations

The deviation parameter s used in these computations was $2.14.10^{-2}$ Å^{-1} , corresponding to the diffraction conditions $\underline{g}(2.4\underline{g})$. Images of a Frank partial dissociated by 79 Å placed at two depths such that the value of d for the stair-rod was 1.0 or $1.04\xi_g$ were computed for foils of thickness t' = $2.0 \rightarrow 2.2\ \xi_g$ where t' is measured in the direction of the beam (ξ_g = 536 Å). Even over this small range the images vary a great deal. Because both partials have large values of $\underline{g}.\underline{b}_{\wedge}\underline{u}$, they can each give rise to two separate peaks. The relative intensities of these peaks are a sensitive function of defect depth and foil thickness and one or more of the peaks can vanish. Fig. 6.4(a) shows the computed images in $1\bar{1}3$ of the defect at the two depths in a foil for which t' = $2.08\ \xi_g$. It is clear that both the sensitive nature of the image and the number of peaks do not agree with experimental images such as fig. 6.3.

These effects may more clearly be seen by plotting the positions of the peaks referred to the X_1 axis against the foil thickness t' , and this is done in fig. 6.5 for a depth d = $1.0\ \xi_g$. That greatly differing images exist at slightly different values of t' is obvious from this figure; equally obvious is the impossibility of obtaining any form of correction equation to derive the horizontal separation Δ of the partials. It was therefore decided to incorporate the effects of beam divergence into the image computations in the hope of removing these undesirable effects. In section 6.2 it was argued that no loops should occur in foils of thickness $\lesssim$ 1000 Å , and clearly the loops which do exist in foils a little thicker than this will be in the centre of the specimen. Therefore the divergent beam effect for an angular spread in the incident beam of α_{max} ,(4.4) , should be significant since the defect

is greater than the critical distance given by (4.11) from either surface.

6.5.3 The divergent beam computations

Computations over a range in s corresponding to the fully-divergent illumination condition as defined in Chapter 5 were performed, initially for the same geometries as described above. Fig. 6.4(b) shows the $1\bar{1}3$ fully-divergent images for the defect deometries corresponding to the parallel beam profiles in fig. 6.4(a). The virtual absence of depth dependent effects can clearly be seen. The form of the profile is now more amenable to description. The stair-rod dislocation gives rise to two peaks symmetrically displaced about the partial position; the closeness of these peaks gives the resultant effect of one rather broad peak situated very close to the core. The Shockley partial now only gives one peak, more intense than the stair-rod contrast, and in the present case lying outside the connecting stacking-fault region. This peak exhibits inside-outside contrast behaviour; changing $\underline{g}$ to $\bar{1}1\bar{3}$ causes this peak to lie between the partials. The fact that the image contrast is now well-behaved enables a relation between Δ and Δ_{obs} to be derived from the curves of peak position in a similar manner to that employed in Chapters 3 and 5.

In fig. 6.6 curves of the Shockley peak position variation with foil thickness are plotted for images in both $1\bar{1}3$ and $\bar{1}1\bar{3}$. The partial is placed at the origin and the X_1 axis is positive in the direction away from the stair-rod. The four geometries used are $\Delta = 64$ Å at d = 1.0 and $1.04\xi_g$; d = 1.0 ξ_g for $\Delta = 20$ and 80 Å . In fig. 6.7 two curves for each of the peaks due to the stair-rod are plotted in a similar fashion and they are for the geometries $\Delta = 64$ Å at d = 1.0 and 1.4 ξ_g . The profiles of fig. 6.4(b) show that in practice these peaks merge to form one wider peak whose position is the mean of that of the original two. The positions of the resultant peak deduced in this way are also plotted,

and it can be seen that the average position of this peak is that of the stair-rod itself. Similar conclusions apply to the other reflection, $\bar{1}1\bar{3}$, except that the original two peaks are further apart (by about 30%) than in the $1\bar{1}3$ case. From the image profiles it can be seen that this does not affect the conclusions conerning the form of the resultant peak.

Dotted boundary lines have been drawn on figs. 6.6 and 6.7 to define the mean position of the peaks. Two results are obtained for the cases considered. They are

$1\bar{1}3$ (outside contrast) $\Delta = \Delta_{obs} - 7.5 \pm 7.5$ Å (6.12)

$\bar{1}3\bar{1}$ (inside contrast) $\Delta = \Delta_{obs} + 7.0 \pm 7.5$ Å (6.13)

6.5.4 Other geometrical arrangements of the Frank partial dissociation

The image calculations have exclusively used the geometry of fig. 6.2(a), but at this pole there are three other arrangements of the dissociation of the Frank partial to be considered; one at the other side of the loop in fig. 6.2(a), and the other two bounding the loop on the inclined $(11\bar{1})$ plane. It is not the intention of this chapter to make a detailed investigation of the dissociation widths in the specimen; if this were the case images would have to be computed for these other geometries. However, (6.12) and (6.13) can be used to obtain a very rough estimate of the dissociation. From the Burgers vector of the Shockley partial it can be seen that the opposite edges of a loop will have the same image behaviour i.e. both give inside or outside contrast; and that the contrast for the inclined plane loops is opposite in nature to that of the foil plane loops in any one micrograph.

6.6 Experimental observations of large dissociated loops

Because of the denuded zone effect discussed in section 6.2 there were large loop-free areas around the hole in all the specimens studied. By using the thickness fringes the foil thickness in which some loops were present could be determined and was generally found to be at

least 1000 Å . It has already been pointed out in section 6.5.2 that these first loops will certainly be at the centre of the foil, and so divergent-beam computed images may be used with confidence in the analysis. The (110) pole is a large angle of tilt away from the (111) foil plane and could only just be reached in the JEM 100B . Fortunately the {113} reflections for which weak-beam conditions could most easily be set up were of the $(1\bar{1}3)$-type which give outside contrast for the loops in the foil plane. Because of the large thicknesses involved the weak-beam intensity was generally low and exposure times of at least one minute were required.

It has already been shown that the two-peak form of the divergent-beam images agrees well with experimental observations, unlike the parallel-beam calculations for which several peaks with large positional variations are predicted (e.g. fig. 6.5). No such effects were observed in any of the specimens. The splitting of the Frank partial dislocation has been resolved in the three materials studied, Cu 10at.% Al, Cu 5at.% Al and pure copper. A micrograph of Frank loops in copper is shown in fig. 6.8(a). The two small loops are on the inclined $(11\bar{1})$ plane and display inside-contrast, whereas the larger loop in the foil plane appears to have a wider separation as predicted in section 6.5.4. The theoretical dissociation of the two partials may be calculated assuming anisotropic elasticity and the Peach-Koehler formula, (2.41). Unfortunately, there is very little agreement between these values and those determined from the micrographs. For example, assuming that for copper $\gamma = 44$ erg cm^{-2} (as obtained in Chapter 5), the theoretical separation is 21.5 Å ; from fig. 6.8(a) the experimental measurement is $\sim$ 40 Å . In the case of Cu 10at.% Al the spread in observed values is 91 $\longrightarrow$ 157 Å . This suggests that in many cases the dissociation does not assume the equilibrium value predicted by theory. Evidence for this view is shown in fig. 6.8(b) which is a micrograph of a Frank loop in Cu 10at.% Al .

It can be seen that the observed separation varies greatly along the side of the triangular loop. One possible explanation for this is that the defect was trapped in a non-equilibrium growth state when the radiating beam and the heating were removed, although the reason for this behaviour is not clear.

6.7 Conclusions

The appearance of small point-defect clusters under both strong and weak-beam conditions has suggested that many of these defects are partially dissociated Frank loops, although the separate partials could not be resolved. Irradiation of thin foils at elevated temperatures in a high-voltage electron microscope produces large loops whose dissociated edges are very useful for determining suitable diffraction conditions for studying smaller defects. The use of {113} reflections at the (110) pole enables the two partials to be resolved, but does not image the stacking faults. Parallel-beam image computations do not agree with the experimental observations, but the calculations of divergent-beam images satisfactorily explain the contrast effects. The separation of the two partials in these specimens can vary greatly along a dissociated edge, and so the successful comparison of images with elasticity calculations was not possible. However, the object of finding a diffraction geometry which can clearly resolve the splitting of a Frank partial has been achieved. These weak-beam observations have the advantage that non-equilibrium spacings such as occur in fig. 6.8(b) may easily be recognised; this would not be possible using conventional strong-beam matching techniques.

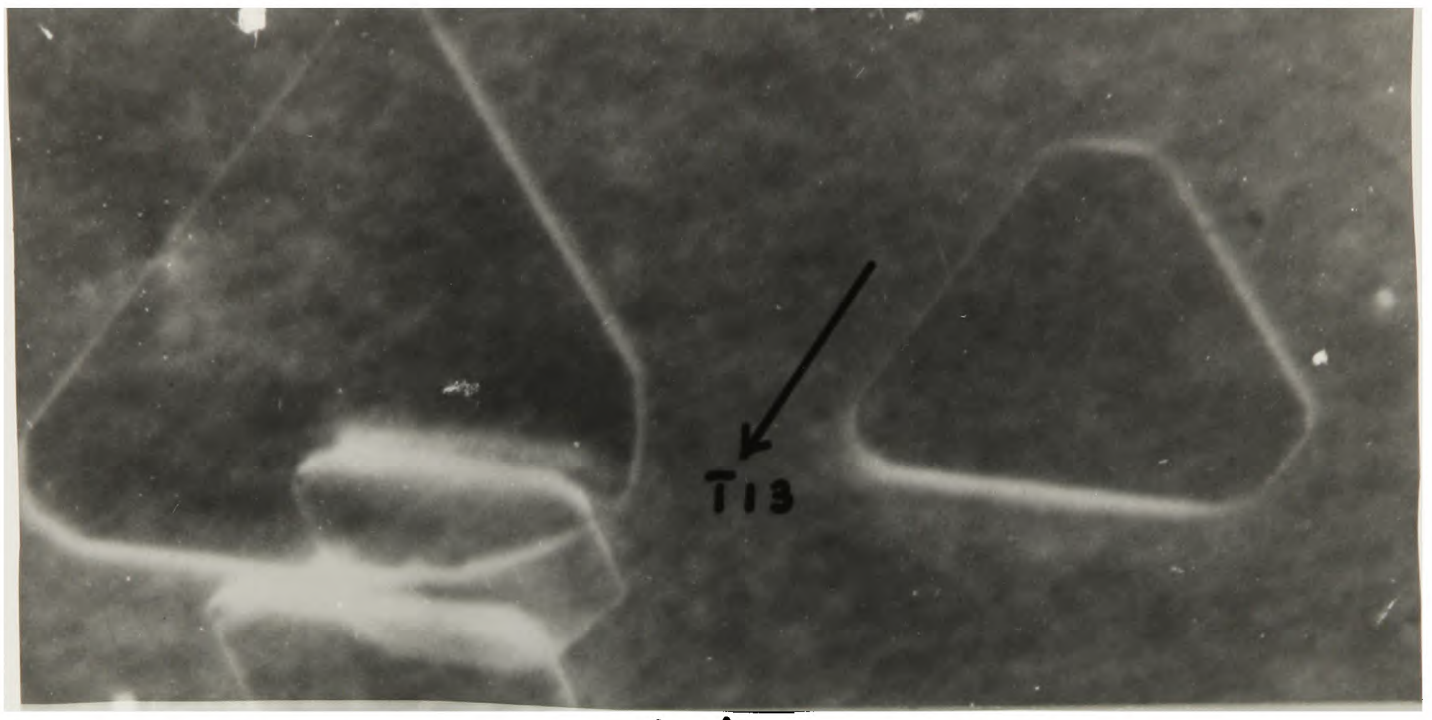

(a)

Foil, upward normal [111] at (110) pole. Return to (111) pole by tilting

1000 Å

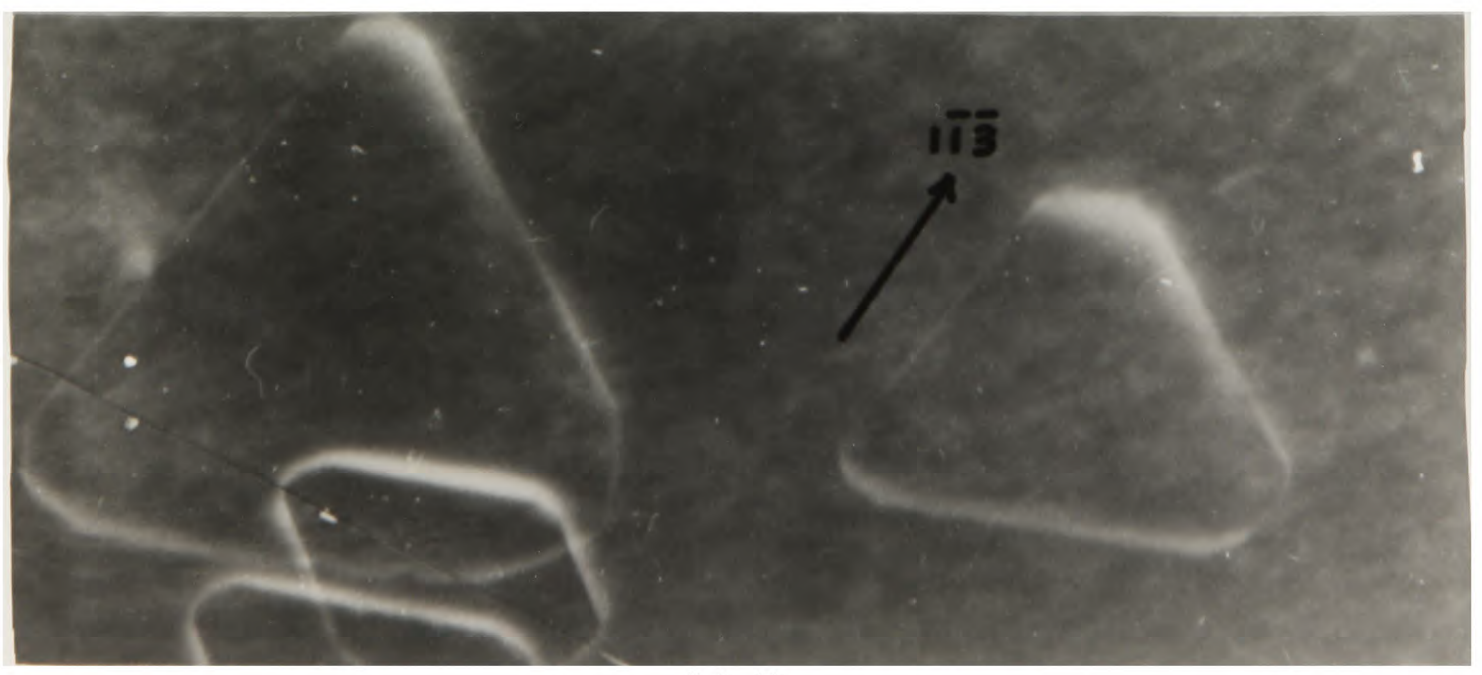

(b)

Figure 6.1 Inside-outside contrast determination of loop fault nature.

(a) outside contrast

(b) inside contrast

The direction of tilt required to return to the (111) pole is shown.

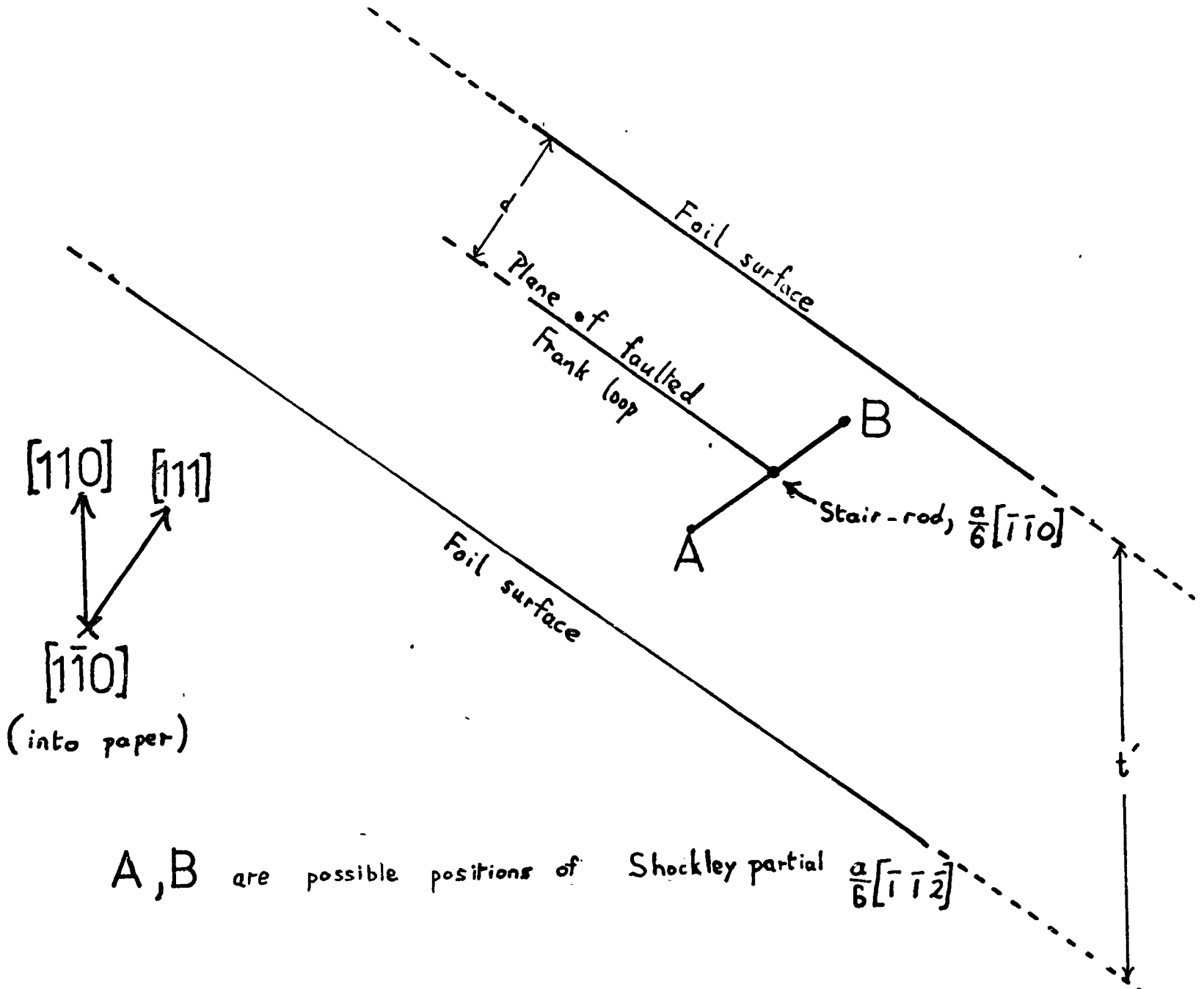

A, B are possible positions of Shockley partial $\frac{a}{6}[\bar{1}\,\bar{1}\,2]$

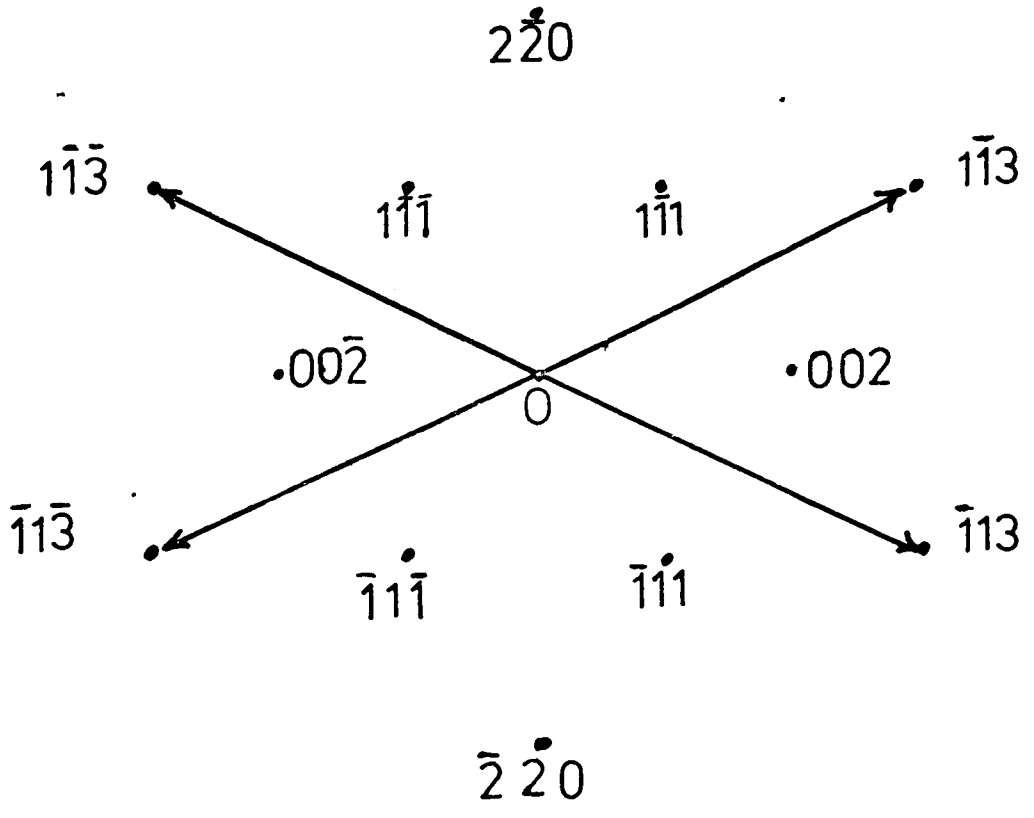

Figure 6.2(a) The dissociation of a Frank partial into a stair-rod and a Shockley partial. A and B represent possible positions for the Shockley. The obtuse angle dissociation given by B results in an intrinsic fault ribbon.

Figure 6.2(b) Diffraction pattern at the (110) pole.

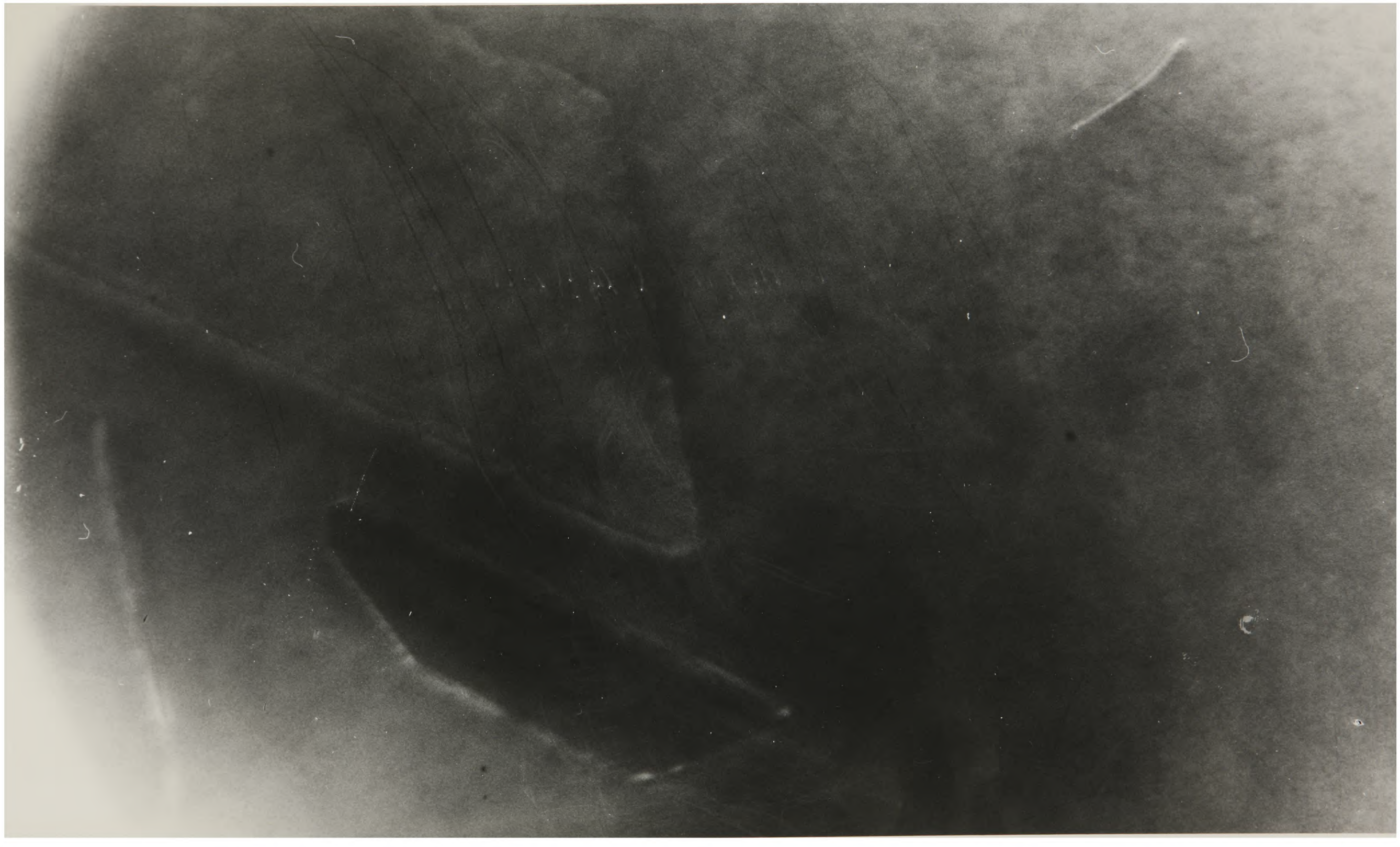

Figure 6.3 Frank loops in Cu 10at.% Al.

The outer peak which bends in and out from various constrictions arises from the Shockley partial.

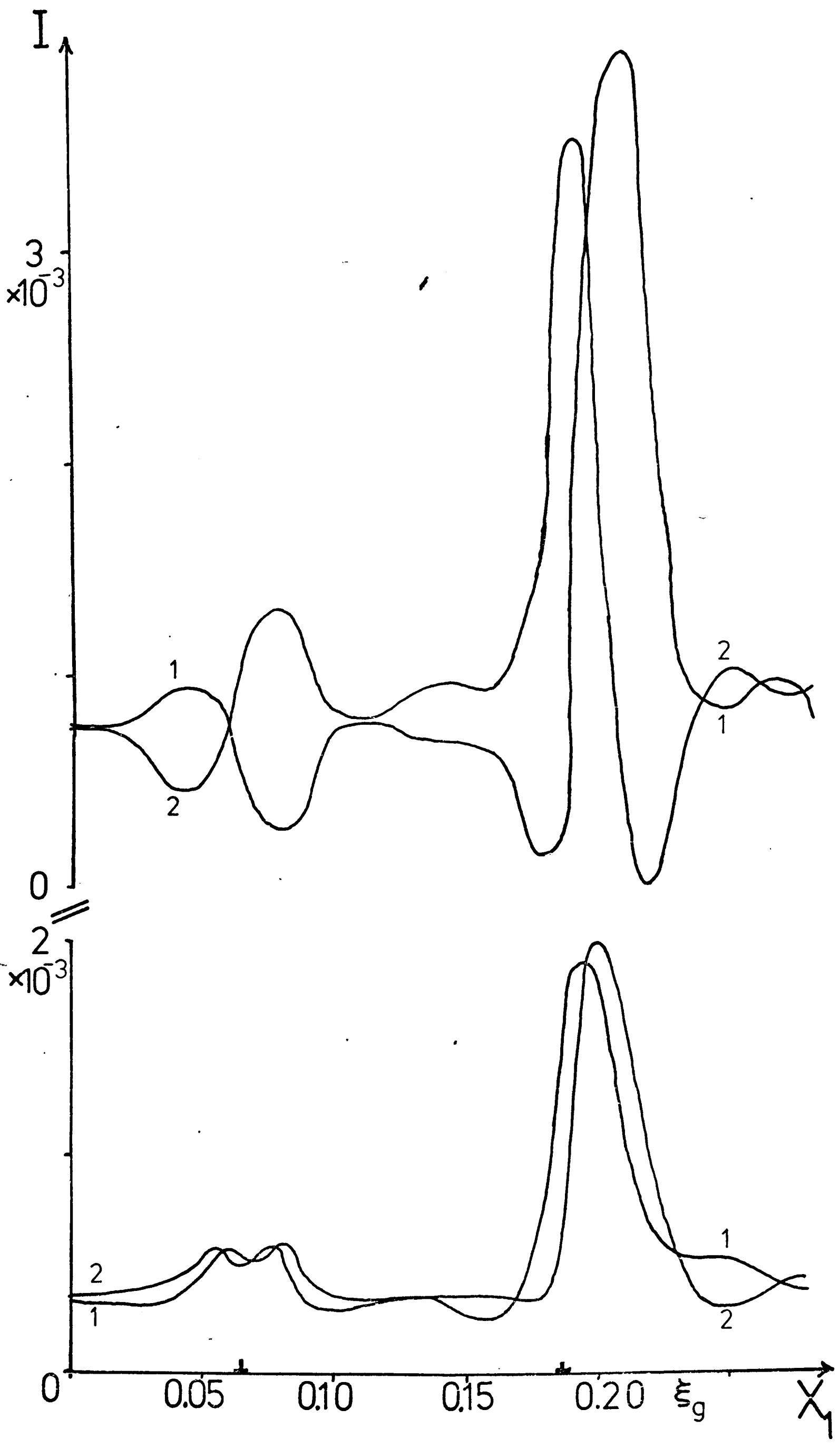
I
3
×10⁻³
0
2
×10⁻³
0
1
2
2
1
1
2
2
1
1
2
0.05
0.10
0.15
0.20
ξg
X1

Figure 6.4(a) Parallel beam image profiles of a dissociated Frank partial. Width of splitting equals 79 Å .

$\underline{g} = 1\bar{1}3$, $t' = 2.08\,\xi_g$.

(1) $d = 1.00\,\xi_g$

(2) $d = 1.04\,\xi_g$.

Figure 6.4(b) Fully-divergent beam image profiles of a dissociated Frank partial. Other details as above.

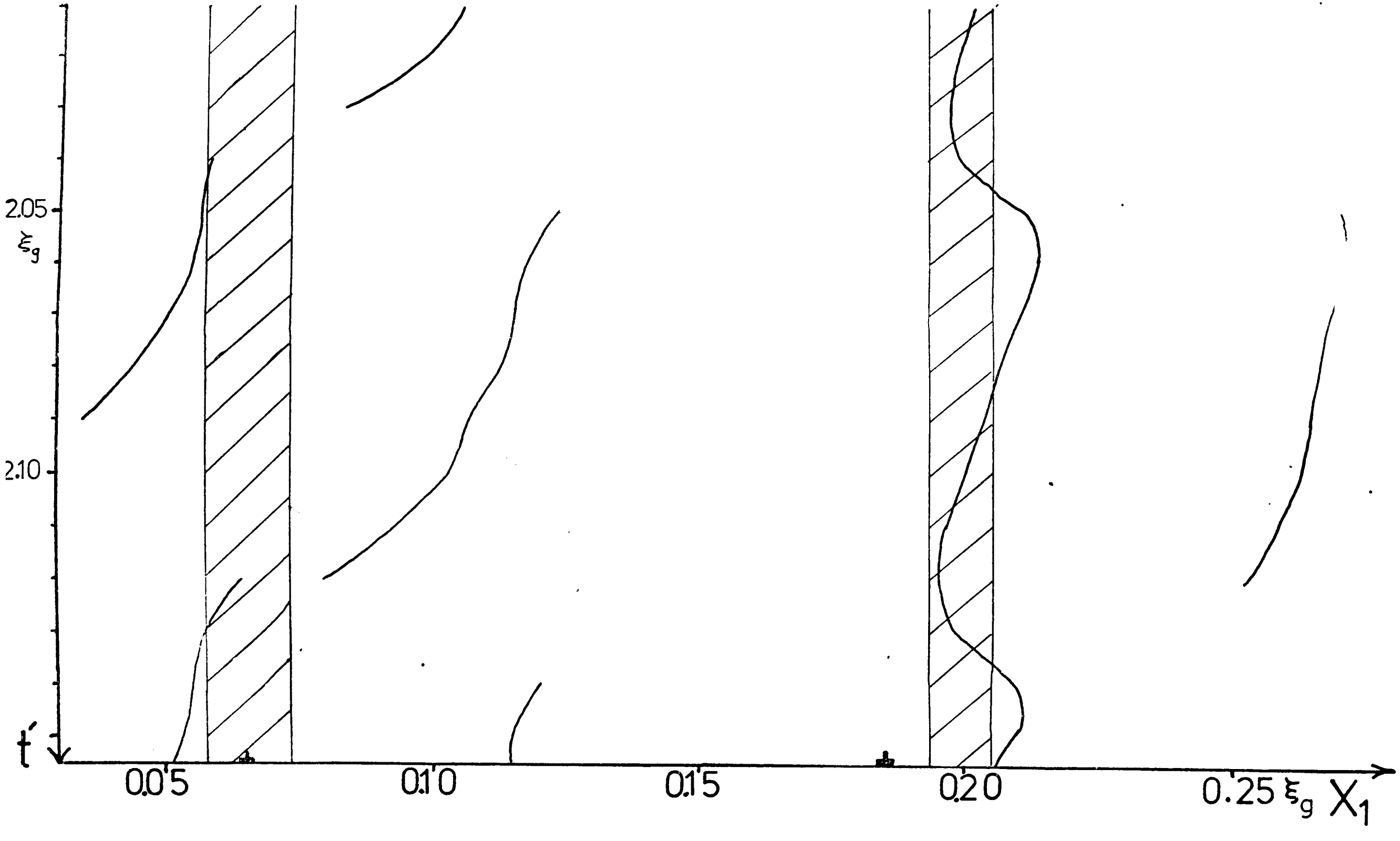
2.05
ξ_g
2.10
t'
0.05
0.10
0.15
0.20
0.25 ξ_g X_1

Figure 6.5 The variations in the peak positions for a dissociated Frank partial computed assuming a parallel beam. The width of dissociation is 79 Å . Depth d = 1.0 ξ_g . The shaded regions represent the positions of the two peaks calculated assuming a fully-divergent beam.

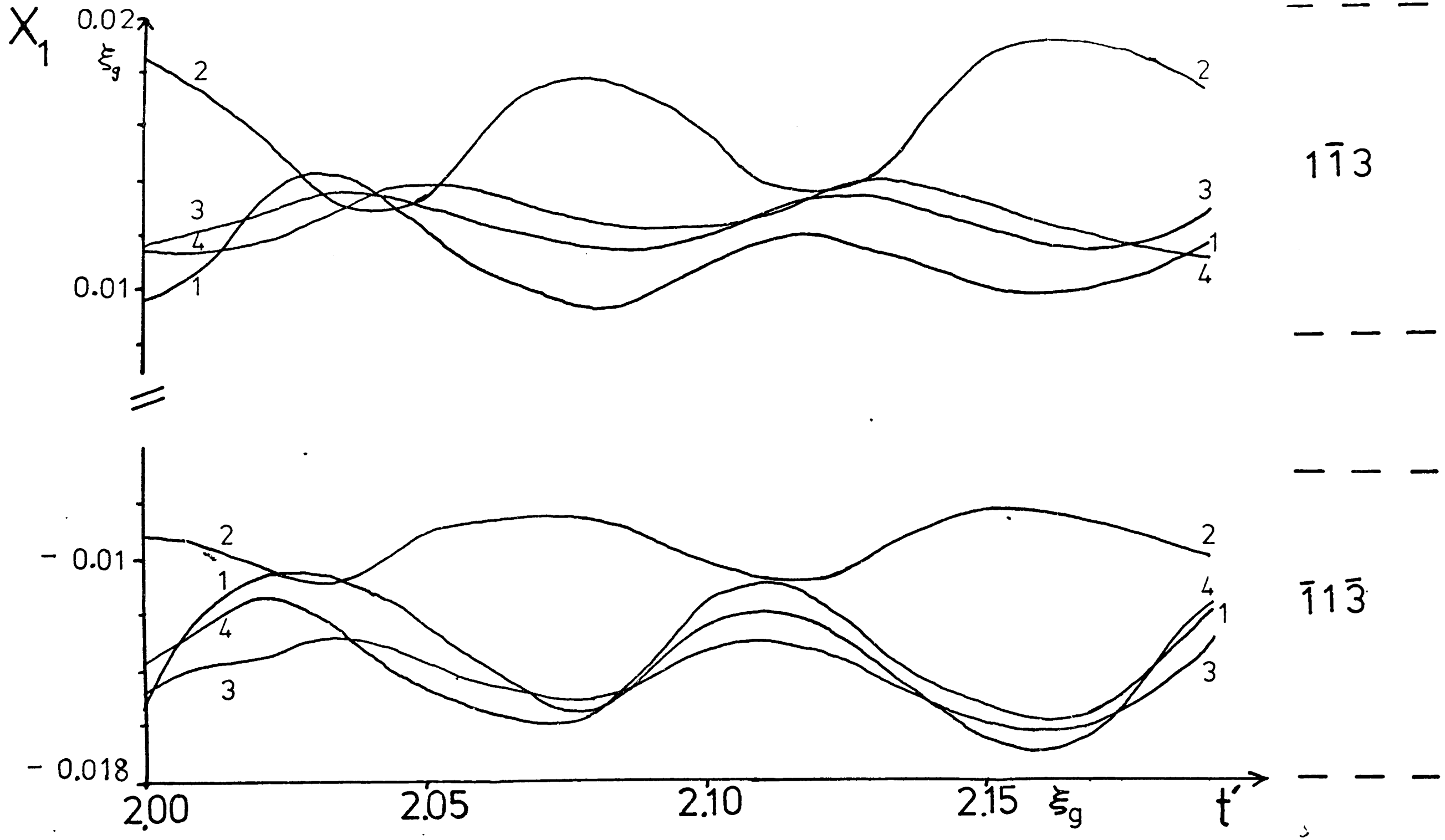
X1
0.02
ξg
0.01
- 0.01
- 0.018
2.00
2.05
2.10
2.15
ξg
t'
1
2
3
4
1 1̄ 3
1̄ 1 3̄

Figure 6.6 The variations in the position of the peak due to the Shockley partial assuming fully divergent illumination for $\underline{g} = \pm (1\bar{1}3)$.

(1) $\Delta = 64$ Å , $d = 1.0\,\xi_g$

(2) $\Delta = 64$ Å , $d = 1.04\,\xi_g$

(3) $\Delta = 20$ Å , $d = 1.0\,\xi_g$

(4) $\Delta = 80$ Å , $d = 1.0\,\xi_g$

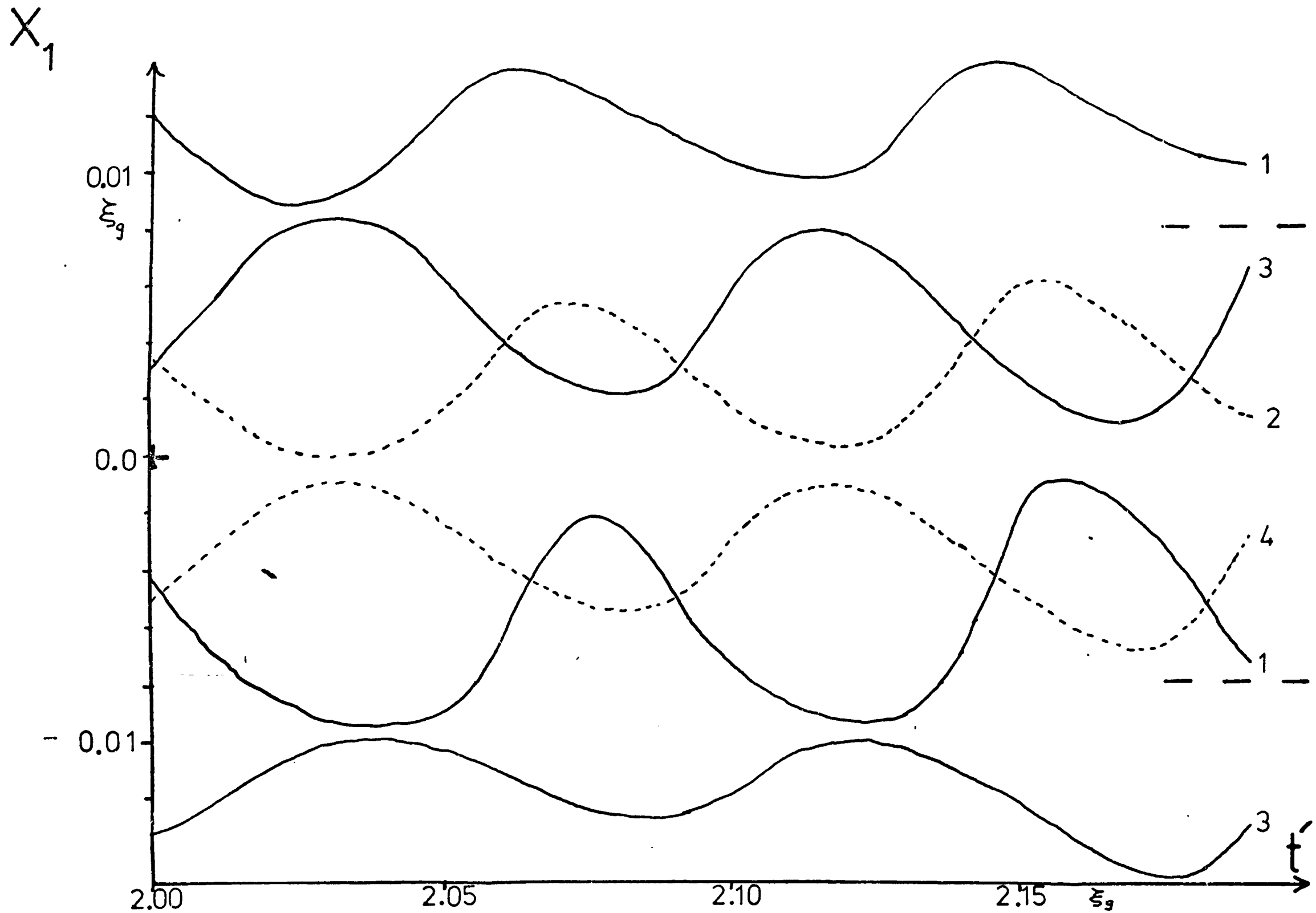
X_1
0.01
ξ_g
0.0
- 0.01
1
2
3
4
1
3
t'
2.00
2.05
2.10
2.15
ξ_g

Figure 6.7 The variations in the positions of the peaks due to the stair-rod assuming fully divergent illumination for $\underline{g} = 1\bar{1}3$.

The mean of the two curves is also plotted.

(1) $\Delta = 64$ Å , $d = 1.0\xi_g$

(2) $\Delta = 64$ Å , $d = 1.0\xi_g$, mean position of the two peaks.

(3) $\Delta = 64$ Å , $d = 1.04\xi_g$

(4) $\Delta = 64$ Å , $d = 1.04\xi_g$, mean position of the two peaks.

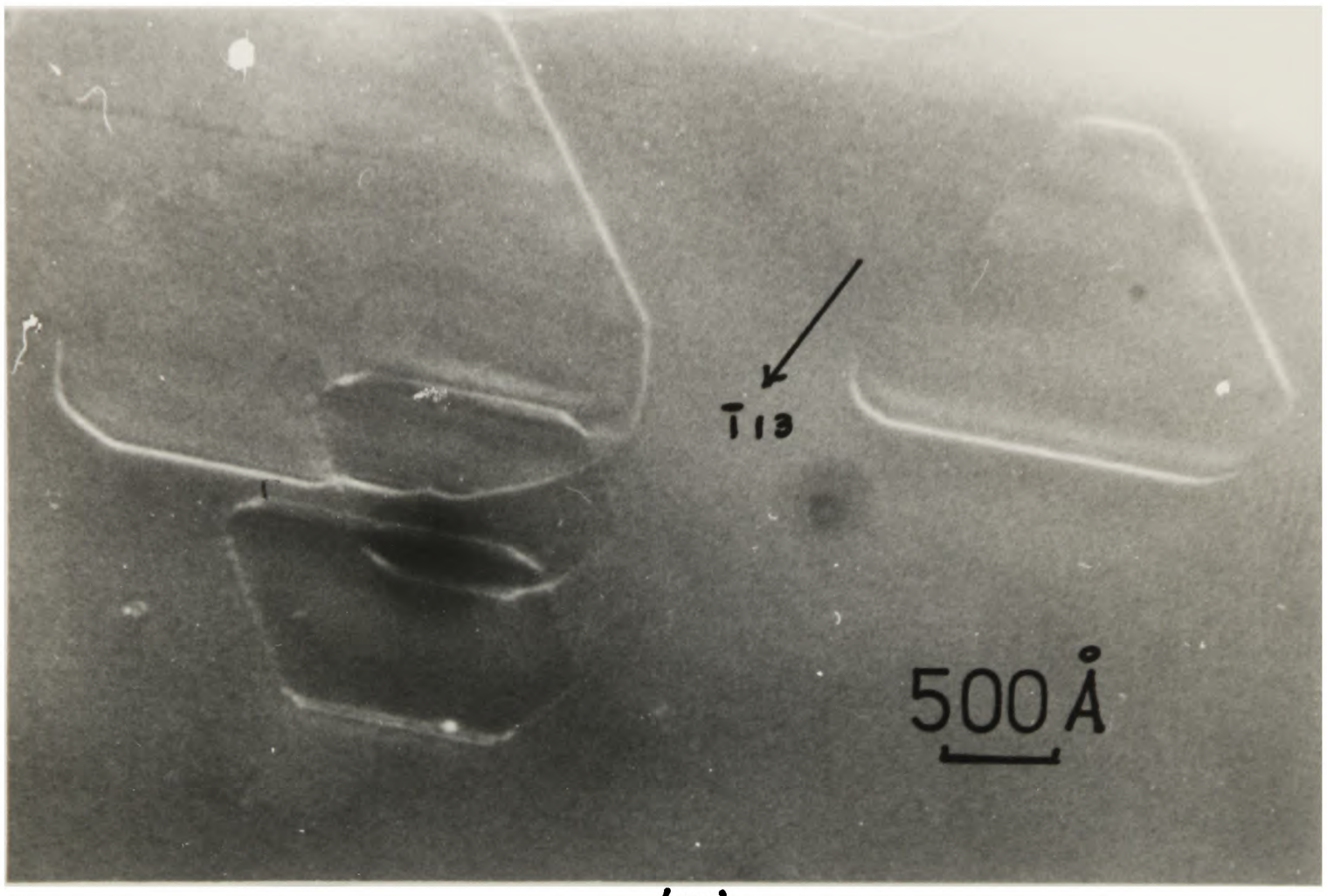

(a)

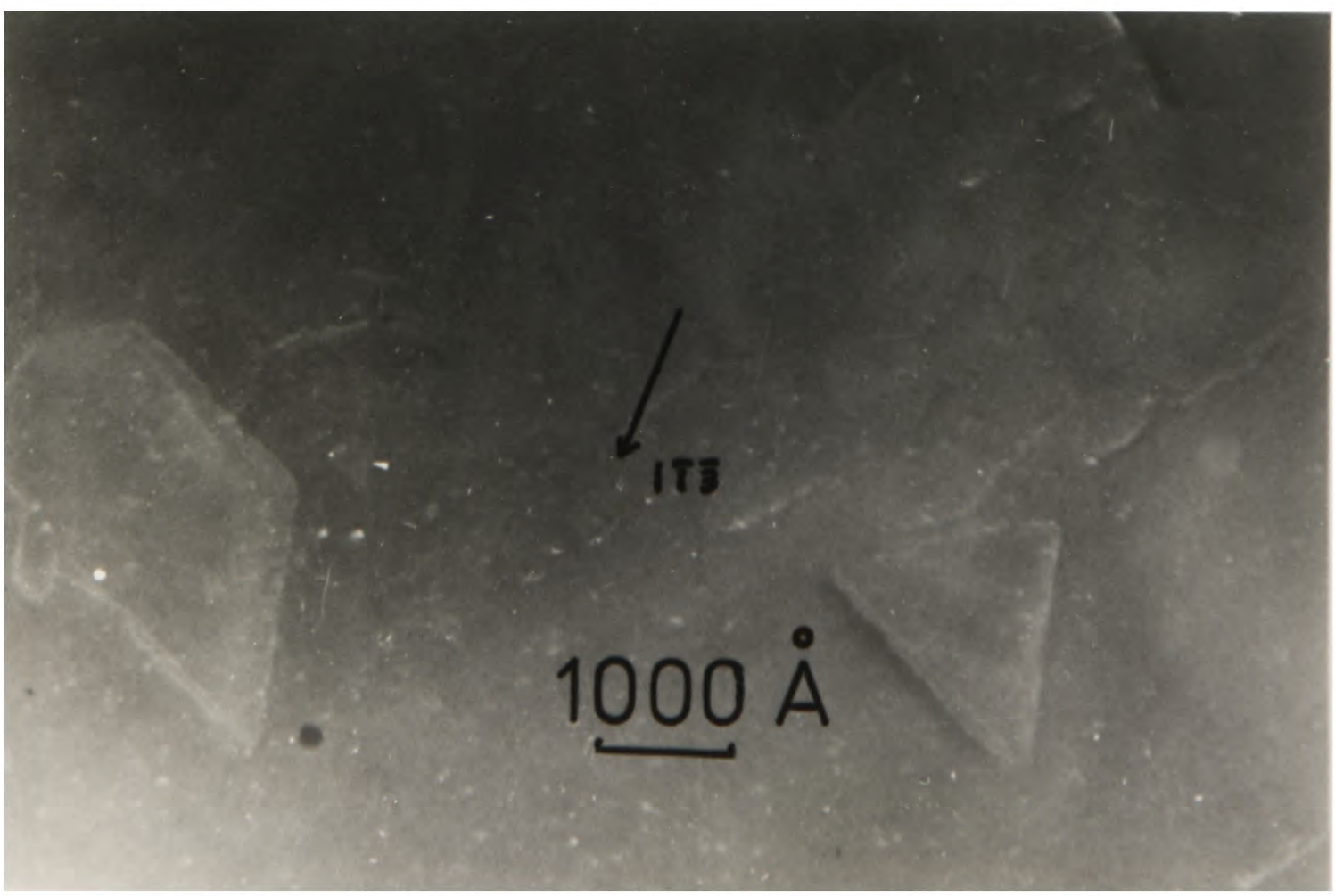

(b)

Figure 6.8(a) Dissociated Frank loops in pure copper.

Figure 6.8(b) Dissociated Frank loops in Cu 10at.% Al . Note the wide variation in the value of Δ_{obs} for the triangular loop dissociation.

Chapter 7

General summary and conclusions

7.1 Introduction

This thesis has considered three dislocation geometries and described the theoretical and experimental aspects of studying these with the high-resolution weak-beam technique of electron microscopy. For two of these geometries the effect of the divergent incident beam of electrons was also included. In this chapter the main points that have arisen are discussed and suggestions of suitable areas for further work are made.

7.2 The study of faulted dipoles

In Chapter 3 it was shown that the observed peak separation Δ_{obs} in $(20\bar{2})$-type images of faulted dipoles with a $[1\bar{1}0]$ line direction could be used to obtain the actual horizontal separation of the Shockley partials Δ. This information enabled a value of γ_{max} to be determined from the equilibrium curves assuming that the defect was a Z dipole or from the transition curves if it was assumed to be an S dipole. This uncertainty as to the type of dipole is inconvenient. It was possible using a $11\bar{1}$ image to obtain a very imprecise idea of the dipole height H, but this was sufficient to make the value of γ_{max} for the S dipole dependent on equilibrium curves rather than on transition curves.

It would clearly be advantageous to obtain an accurate value for H as well as Δ. This could be done by tilting through a larger angle, possibly to a $\{110\}$ pole. Image computations to investigate this method are planned. Even with both Δ and H of the same dipole, it may not be possible to determine if it is S or Z, but every observation would yield two possible values of γ (unlike the present case, where only the widest observed image is used to give two values of γ_{max}). With several observations the correct value of γ would soon be apparent, and this information could then be used to deduce the type of any observed dipole.

The obvious application of these observations (apart from simply studying the properties of faulted dipoles in general) is to obtain values of γ of materials for which the dissociation of an edge dislocation is too small to be clearly resolved even by the weak-beam technique. One such material is nickel, and preliminary measurements on faulted dipoles suggest an upper limit of

$$\gamma_{max} = 150 \pm 40 \text{ erg cm}^{-2}$$

7.3 Divergent-beam illumination

In Chapter 5 it was shown that the effect of a divergent incident beam is to remove thickness and depth dependence effects in images of dislocations greater than a certain critical distance from either surface. The damping of intensity oscillations is particularly interesting when one considers small defects since in parallel-beam calculations these can disappear completely for certain combinations of depth and foil thickness. It would be interesting to calculate divergent-beam images for a small loop and see if a removal of intensity oscillations similar to that noted in straight dislocation images does in fact occur.

In Chapter 6 it was found that the parallel-beam images of the two partials at the edge of a dissociated Frank loop were very sensitive to depth and thickness changes and the number of peaks could vary between two and four. This behaviour is due to the large $\underline{g}.\underline{b}_{\wedge}\underline{u}$ components for both partials. The divergent beam effect changes this to two stable well-behaved peaks, and this agrees with the experimental images. It may be possible to apply this diffraction geometry which was developed with the large loops to resolving the dissociation (if any) of small Frank loops in heavy-ion irradiated materials.

Therefore the divergent beam, besides damping intensity oscillations, can also change the fundamental character of weak-beam

images and the possibility of such effects should be borne in mind.

7.4 Extended core effects

Much interest has been expressed recently in the literature as to the possibility of gross systematic errors in deducing values of from experimental observations by assuming that the dislocation cores are singular (see section 5.5). If extended core effects are of importance in affecting dislocation separations and weak-beam images, one might expect this to be noticeable when deriving values of γ from two different types of defect in the same material. The very good agreement between that determined from dissociated edge dislocations and that derived from faulted dipoles in the case of copper, although it could be coincidental, strongly suggests that such effects are negligible in these defects.

References

Ashby, M.F. and Brown, L.M., 1963,

Phil. Mag., 8, 1083, 1649.

Bollinger, E., Condat, M. and Fayard, M., 1974,

phys. stat. sol. (a), 24, K.95.

Brown, L.M., 1969,

Phil. Mag., 19, 869.

Brown, L.M., Kelly, A. and Mayer, R.M., 1969,

Phil. Mag., 19, 721.

Burgers, J.M., 1939,

Proc. Kon. Ned. Akad. Wetenschap, 42, 293, 378.

Carter, C.B. and Ray, I.L.F., 1974,

Phil. Mag., 29, 1231.

Clarebrough, L.M. and Morton, A.J., 1969,

Austr. J. Phys., 22, 351, 371.

Cockayne, D.J.H., 1970,

D. Phil. Thesis, Oxford.

Cockayne, D.J.H., 1972,

Z. Naturforsch., 27a, 452.

Cockayne, D.J.H., 1973,

J. Microsc., 98, 116.

Cockayne, D.J.H., Jenkins, M.L. and Ray, I.L.F., 1971,

Phil. Mag., 24, 1383.

Cockayne, D.J.H., Parsons, J.R. and Hoelke, C.W., 1971,

Phil. Mag., 24, 139.

Cockayne, D.J.H., Ray, I.L.F. and Whelan, M.J., 1969,

Phil. Mag., 20, 1265.

Cockayne, D.J.H. and Vitek, V., 1974,

phys. stat. sol. (b), 65, 751.

Cockayne, D.J.H. and Whelan, M.J., 1970,

Proc. 7th Int. Cong. Electron Microscopy, Grenoble, 1, 29.

Englert, A., Tompa, H. and Bullough, R., 1970,

Nat. Bureau Standards, Special Publication 317, Washington, D.C.

Eshelby, J.D., Read, W.T. and Shockley, W., 1953,

Acta Met., 1, 251.

Eyre, B.L., 1973,

J. Phys. F., 3, 422.

Frank, F.C., 1951,

Phil. Mag., 42, 809.

Fujimoto, F., 1959,

J. Phys. Soc. Japan, 14, 1588.

Goringe, M.J., 1971,

Rad. Eff., 10, 169.

Goringe, M.J., 1973,

J. Microscopie, 16, 169.

Grivet, P., 1965,

Electron Optics, Oxford.

Häussermann, F., Katerbau, K.H., Rühle, M. and Wilkens, M., 1973,

J. Microsc., 98, 135.

Häussermann, F. and Wilkens, M., 1966,

phys. stat. sol., 18, 609.

Head, A.K., 1967,

Austr. J. Phys., 20, 557.

Head, A.K., Humble, P., Clarebrough, L.M., Morton, A.J. and Forwood, C.T. 1973,
Computed Electron Micrographs and Defect Identification (Defects in Crystalline Solids Vol.7), North Holland Publishing Co., Amsterdam.

Hearmon, R.F.S., 1956,
Adv. Phys., 5, 323.

Hirsch, P.B., 1963,
The Relation between Structure and Mechanical Properties of Metals, p.48, H.M.S.O. London.

Hirsch, P.B., Howie, A., Nicholson, R.B., Pashley, D.W. and Whelan, M.J., 1965,
Electron Microscopy of Thin Crystals, Butterworth, London.

Hirsch, P.B., Howie, A. and Whelan, M.J., 1960,
Phil. Trans. Roy. Soc., A252, 499.

Hirth, J.P. and Lothe, J., 1968,
Theory of Dislocations, McGraw-Hill, New York.

Holmes, S.M., Cockayne, D.J.H. and Ray, I.L.F., 1974,
Proc. 8th Int. Cong. Electron Microscopy, Canberra, 1, 290.

Howie, A., 1963,
Proc. Roy. Soc., A271, 268.

Howie, A. and Basinski, Z.S., 1968,
Phil. Mag., 17, 1039.

Howie, A., Krivanek, O.L. and Rudee, M.L., 1973,
Phil. Mag., 27, 235.

Howie, A. and Sworn, C.H., 1970,
Phil. Mag., 22, 861.

Howie, A. and Whelan, M.J., 1960,
Proc. Eur. Reg. Conf. Electron Microscopy, Delft, 1, 181.

Howie, A. and Whelan, M.J., 1961,
Proc. Roy. Soc., A263, 217.

Humphreys, C.J. and Hirsch, P.B., 1968,

Phil. Mag., 18, 115.

Huntington, H.B., 1958,

Solid St. Phys., 7, 214.

Ipohorski, M and Spring, M.S., 1969,

Phil. Mag., 20, 937.

Jenkins, M.L., 1973,

D.Phil. Thesis, Oxford.

Jenkins, M.L., 1974,

Phil. Mag., 29, 813.

Jones, P.M. and Steeds, J.W., 1974,

Proc. 8th Int. Cong. Electron Microscopy, Canberra, 1, 294.

Kamiya, Y and Uyeda R., 1961,

J. Phys. Soc. Japan, 16, 1361.

Lenz, F., 1965,

Laboratory Investigation, 14, 808.

Longhurst, R.S., 1973,

Geometrical and Physical Optics (3rd Edition), Longmans, London.

Lynch, D.F. and O'Keefe, M.A., 1972,

Acta Crystallogr., A28, 536.

Mader, S., 1963,

Electron Microscopy and Strength of Crystals, p.183,

Interscience, New York.

Makin, M.J., 1968,

Phil. Mag., 18, 637.

Makin, M.J., 1969,

Phil. Mag., 20, 1133.

Melander, A. and Sandström, R., 1974,

phys. stat. sol. (a), 22, 587.

Menter, J.W., 1956,

Proc. Roy. Soc., A236, 119.

Menter, J.W., 1958,

Adv. Phys., 7, 299.

Morton, A.J. and Forwood, C.T., 1973,

Crystal Lattice Defects, 4, 165.

Mott, N.F. and Massey, H.S.W., 1949,

The Theory of Atomic Collisions, Clarendon Press, Oxford.

Norris, D.I.R., 1970,

Phil. Mag., 22, 1273.

Orowan, E., 1934,

Z. Phys., 89, 605, 634.

Parsons, J.R. and Hoelke, C.W., 1969,

J. Appl. Phys., 40, 866.

Parsons, J.R., Hoelke, C.W. and Rainville M., 1968,

Proc. 4th Eur. Conf. Electron Microscopy, Rome, 1, 133.

Peach, M. and Koehler, J.S., 1950,

Phys. Rev., 80, 436.

Perrin, R.C. and Savino, E.J., 1973,

J. Microsc, 98, 214.

Phillips, V.A. and Hugo, J.A., 1970,

Acta Metall., 18, 123.

Polanyi, M., 1934,

Z Phys., 89, 660.

Seeger, A., 1964,

Discuss. Faraday Soc., 38, 82.

Seeger, A. and Schöck, G., 1953,

Acta Metall., 1, 519.

Seeger, A. and Wobser, G., 1966,

phys. stat. sol., 18, 189.

Silcox, J. and Hirsch, P.B., 1959,

Phil. Mag., 4, 72.

Smith, G.H. and Burge, R.E., 1962,

Acta crystallogr., 15, 182.

Steeds, J.W., 1967a,

Phil. Mag., 16, 771.

Steeds, J.W., 1967b,

Phil. Mag., 16, 785.

Stobbs, W.M. and Sworn, C.H., 1971,

Phil. Mag., 24, 1365.

Stroh, A.N., 1958,

Phil. Mag., 3, 625.

Sturkey, L., 1957,

Acta crystallogr., 10, 858.

Takagi, S., 1962,

Acta crystallogr., 15, 1311.

Taylor, G.I., 1934,

Proc. Roy. Soc., A145, 362.

Thompson, N. 1953,

Proc. Phys. Soc., 66B, 481.

Valentine, R.C., 1966,

Advances in Optical and Electron Microscopy, 1, 180,

Academic Press, London.

Volterra, V., 1907,

Ann. Ecole Norm. Super., 24, 400.

Whelan, M.J., 1971,

Proc. Chalk River Conf., Atomic Energy of Canada report

CRNL-622-1, p. 307.

Whelan, M.J. and Hirsch, P.B., 1957a,

Phil. Mag., 2, 1121.

Whelan, M.J. and Hirsch, P.B., 1957b,

Phil. Mag., 2, 1303.

Wilson, M.M., 1970,

D. Phil. Thesis, Oxford.

Wilson, M.M., 1971,

Phil. Mag., 24, 1023.

Wilson, M.M. and Hirsch, P.B., 1972,

Phil. Mag., 25, 983.